

ISSN • 2708-6437 (Online)
• 2708-6429 (Print)

Journal of Engineering Advancements

Editor-in-Chief:

Prof. Dr. Mohammad Mashud

Volume 02 Issue 02



**Published by:
SciEn Publishing Group**

Journal of Engineering Advancements

Apt. # 6 C-D, House # 191
Road # 9/A, Dhanmondi R/A
Dhaka-1209, Bangladesh

Email: jea@scienpg.com

Website: www.scienpg.com/jea/

Editor-in-Chief

Prof. Dr. Mohammad Mashud
Khulna University of Engineering & Technology
Khulna-9203, Bangladesh.
Tel: +880-41-769468 Ext. 405
Email: mdmashud@me.kuet.ac.bd

Executive Editors

Dr. Md. Arifuzzaman
Khulna University of Engineering & Technology
Khulna-9203, Bangladesh.
Email: arif48@me.kuet.ac.bd

Dr. Md. Shariful Islam
Khulna University of Engineering & Technology
Khulna-9203, Bangladesh.
Email: msislam@me.kuet.ac.bd

Editors

Dr. Abul Mukid Mohammad Mukaddes
Shahjalal University of Science and Technology
Email: mukaddes1975@gmail.com
Bangladesh

Dr. Md. Rashedul H. Sarker
University of Indianapolis
Email: sarkerm@indy.edu
USA

Dr. Chu Chi Ming
University Malaysia Sabah
Email: chrischu@ums.edu.my
Malaysia

Dr. Seock Sam Kim
University Malaysia Sabah
Email: sskim@ums.edu.my
Malaysia

Dr. Mohammad H. Rahman
University of Wisconsin-Milwaukee
Email: rahmanmh@uwm.edu
USA

Dr. Sabuj Mallik
University of Derby
Email: s.mallik@derby.ac.uk
UK

Dr. Sivakumar Kumaresan
University Malaysia Sabah
Email: shiva@ums.edu.my
Malaysia

Dr. Mohd Suffian Bin Misaran
University Malaysia Sabah
Email: suffian@ums.edu.my
Malaysia

Dr. Md. Mizanur Rahman
World University of Bangladesh
Email: mizanur.rahman@mte.wub.edu.bd
Bangladesh

Dr. Zahir Uddin Ahmed
Khulna University of Engineering & Technology
Email: zuahmed@me.kuet.ac.bd
Bangladesh

Dr. Riaz U. Ahmed
University of Wisconsin-Green Bay
Email: ahmedm@uwgb.edu
USA

Dr. Mohammad Ilias Inam
Khulna University of Engineering & Technology
Email: iliasinam@me.kuet.ac.bd
Bangladesh

Dr. Kazi Mostafijur Rahman
Khulna University of Engineering & Technology
Email: mostafij@me.kuet.ac.bd
Bangladesh

Dr. Md. Mahfuz Sarwar
AECOM
Email: mahfuzsarwar@yahoo.com
Australia



Published in: June 2021

Published by: SciEn Publishing Group

Dr. Md. Abdullah Al Bari
Khulna University of Engineering & Technology
Email: abdullahalbari@me.kuet.ac.bd
Bangladesh

Journal of Engineering Advancements

Volume 02, Issue 02

June 2021

CONTENTS

Original Articles

01. Numerical Investigation of Aerodynamic Characteristics of NACA 4312 Airfoil with Gurney Flap
Subah Mubassira, Farhana Islam Muna, Mohammad Ilias Inam 63
02. Quartic Non-polynomial Spline Method for Singularly Perturbed Differential-difference Equation with Two Parameters
Gemadi Roba Kusi, Tesfaye Aga Bullo, Gemechis File Duressa 71
03. Morphogenesis of Silicovanadate Glasses: Investigation of Physical Properties
Md. Moinul Islam, Md. Abdur Rashid, Md. Parvez Ahamed, Md. Emran Hossain, M. Rafiqul Ahsan, M. Golam Mortuza, Mirza Humaun Kabir Rubel 78
04. Numerical Investigation of Liquid–Liquid Mixing in Modified T Mixer with 3D Obstacles
Md. Readul Mahmud 87
05. Fabrication and Characterization of α -Fe₂O₃ Nanoparticles Dispersed Epoxy Nanocomposites
Muhammad Abdullah Al Mamun, Md. Abdus Sabur, Md. Abdul Gafur, Hrithita Aftab, G.M. Shafiur Rahman 95
06. Production and Characterization of Biodiesel from Avocado Peel Oils using Experimental Analysis (ANOVA)
Tafere Aga Bullo, Feyissa Bekele Fana 104
07. Design and Analysis of A Vortex Induced Vibration Based Oscillating Free Stream Energy Converter
Ratan Kumar Das, Muhammad Taharat Galib 112

This page is intentionally left blank.

Journal of Engineering Advancements

Editor-in-Chief

Prof. Dr. Mohammad Mashud
Department of Mechanical Engineering,
Khulna University of Engineering & Technology, Khulna, Bangladesh

Executive Editors

Dr. Md. Shariful Islam
Department of Mechanical Engineering,
Khulna University of Engineering & Technology, Khulna, Bangladesh

&

Dr. Md. Arifuzzaman
Department of Mechanical Engineering,
Khulna University of Engineering & Technology, Khulna, Bangladesh



Published by: SciEn Publishing Group

Apt. # 6 C-D, House # 191, Road # 9/A
Dhanmondi, Dhaka-1209, Bangladesh
Email Address: jea@scienpg.com

www.scienpg.com/jea/

This page is left intentionally blank

Numerical Investigation of Aerodynamic Characteristics of NACA 4312 Airfoil with Gurney Flap

Subah Mubassira^{1*}, Farhana Isalm Muna², Mohammad Ilias Inam²

¹Department of Mechanical Engineering, Bangladesh University of Engineering & Technology, Dhaka-1000, BANGLADESH

²Department of Mechanical Engineering, Khulna University of Engineering & Technology, Khulna-9203, BANGLADESH

Received: February 08, 2021, Revised: April 04, 2021, Accepted: April 05, 2021, Available Online: April 10, 2021

ABSTRACT

This paper presents a two-dimensional Computational Fluid Dynamics (CFD) analysis on the effect of gurney flap on a NACA 4312 airfoil in a subsonic flow. These numerical simulations were conducted for flap heights 1.5%, 1.75%, 2% and 3% of chord length at fixed Reynold Number, Re (5×10^5) for different angle of attack ($0^\circ \sim 16^\circ$). ANSYS Fluent commercial software was used to conduct these simulations. The flow was considered as incompressible and K-omega Shear Stress Transport (SST) model was selected. The numerical results demonstrate that lift coefficient increase up to around 120° AoA (angle of attack) for NACA 4312 with and without gurney flap. For every AoA lift coefficient and drag coefficient presented proportionate behavior with flap height. However, lift coefficient was decreased after around 12° angle of attack due to flow separation. Maximum lift to drag ratio was found at around 4° AoA for every flap length and airfoil with flap of 1.5% C (chord length) had shown the most optimized aerodynamic performance through the analysis. This study concluded that airfoil with gurney flap displayed enhanced aerodynamic performance than the airfoil without gurney flap due to the delay in flow separation.

Keywords: CFD, Airfoil, Gurney flap, Lift-Coefficient, Drag-Coefficient, Pressure-Coefficient.



This work is licensed under a [Creative Commons Attribution-Non Commercial 4.0 International License](https://creativecommons.org/licenses/by-nc/4.0/).

1 Introduction

Airfoil design is important for the wing and control surface performance in aerospace engineering. CFD investigation is faster and cheaper than experimental testing. An airfoil is the cross-sectional shape of a wing [1]. Gurney flap or wicker bill is a lift enhancing device which is vastly used in aerodynamics. Gurney flap is a micro tab attached at trailing edge on airfoil's lower surface side perpendicularly. Attaching a gurney flap with an airfoil is easy method to increment the lift co-efficient of the airfoil mechanically. For increased lift generation takeoff can be steeper, resulting reduced noise. Also for better lift to drag ratio, the aircraft can achieve cruise altitude quicker. It also increases fuel-efficiency [2]. By attaching the boundary layer up to trailing edge gurney flap increases the lift co-efficient [3]. Common applications of gurney flap are in auto racing, helicopter horizontal stabilizers and high lift aircraft like banner-towing airplanes. Liebeck [4] first experimented on gurney flap to investigate the aerodynamic characteristics in wind tunnel. He observed that there was a lift enhancement at every angle of attack with respect to clean airfoil. Neuhart and Pendergraft [5] examined NACA 0012 wing with various gurney flap in a water tunnel study and justified Liebeck's statement. Jeffrey mentioned that gurney flaps were initially used for improving downforce and stability in racing cars by the race car driver Daniel Gurney [6]. Jang [2] investigated the lift enhancement of gurney flap in his experiment. Yoo [7] observed the increase of lift co-efficient through his experiment. Li [8] verified this fact by his observation too. A formation of a small recirculation region at upstream of the flap were observed by all of them. Fernandez-Gamiz [9] analyzed the outcome of Vortex Generators and Gurney Flaps on a wind turbine. Armendenia [10] observed the improvement of a modification method for the

gurney flap height for different wind and rotor blade airfoil geometry setups and concluded the non-linear dependency of lift to drag ratio on AoA and GF height. Graham [11] experimented the consequence of width and height of GF by using open circuit subsonic wind tunnel. A proportional relation between lift and flap height and an inversely proportional relation between lift and flap thickness were established in his study. A CFD analysis was done by Jain [12] to examine the impact of gurney flap on NACA 0012 airfoil for various heights at varying locations from trailing edge. It was observed that 0.015 height to chord ratio (H/C) of gurney flap resulted maximum lift coefficient (C_l). Storms [13] experimentally measured aerodynamic properties for NACA 4412 airfoil with GF and vortex generator and suggested that by using both GF and Vortex generator simultaneously, airfoil displayed better performance than using these individually. Ankit kumar [1] analyzed numerically the ground effect on NACA 4412 airfoil with varying AoA and gurney flap ranging from 0.5% C to 2.5% C. Airfoil with 1.5% C flap had shown the maximum lift to drag ratio in the study. A significant enhancement in performance was observed by Myose [14] during the investigation of the gurney flap effect on NACA0011 and GS(W)-2 airfoils. Cole [15] inspected the aerodynamic impact of gurney flap at varying height in subsonic, low-turbulence wind tunnel and chord-wise locations of various airfoils. He proposed that GF at trailing edge showed better result and witnessed lift enhancement for each airfoils. Ahmed [16] experimented the flow behavior of NACA 4412 airfoil with little turbulence and moving ground simulation at Reynolds no. 3×10^5 with varying AoA and obtained that the airfoil geometry also had a great impact on aerodynamic performance aside from AoA and ground clearance. Webb [17] did a wind tunnel test for both wing and airfoil section with varying lengths of GF and perceived a greater lift to drag ratio. Camocardi [18] experimented in wind

tunnel on an airfoil with flexible GF. The performance of fixed gurney flap joint with airfoil showed higher lift coefficient than the movable gurney flap. 30% enhancement in lift coefficient was seen by Maughmer [19] during the inspection of the aerodynamics properties of gurney flaps in subsonic wind tunnels at Reynolds number 10^6 . Chand [20] compared the aerodynamics properties of a multi element airfoil and a standard NACA airfoil where the performance was found superior for multi element airfoil.

Analyzing the aforementioned literature, it is quite apparent that enough light hasn't been shed on enhancing the performance of NACA 4312 airfoil. The aim of this present study is to investigate the effect of GF height on aerodynamic performance and evaluating the optimum height for the airfoil. The flow characteristics were compared between airfoil with and without flap computationally for Reynolds number 5×10^5 with varying AoA ($0^\circ - 16^\circ$). Since the geometry of airfoil has a great impact on aerodynamic characteristics, it is essential to determine the height of the GF. Finite volume method (FVM) was used to carry out to solve the cases on ANSYS Fluent and $k - \omega$ SST was chosen as a turbulence model for this study.

2 Computational Method

2.1 Geometry Modeling

NACA 4312 airfoil was chosen as geometrical model for gurney flap study. The NACA-4312 airfoil indicates maximum camber of 4%C which is situated at 30%C from the leading edge. Maximum thickness of the airfoil is 12% length of chord. For present analysis, chord length was taken 1000 mm. Airfoil geometry was generated in SolidWorks by importing coordinates file and is shown in Fig. 1(a) and in Fig. 1(b) airfoil with flap is shown. Reviewing previous literatures, four different lengths of GF were chosen for this study which were of 1.5%C, 1.75%C, 2%C and 3%C with varying AoA ($0^\circ - 16^\circ$).

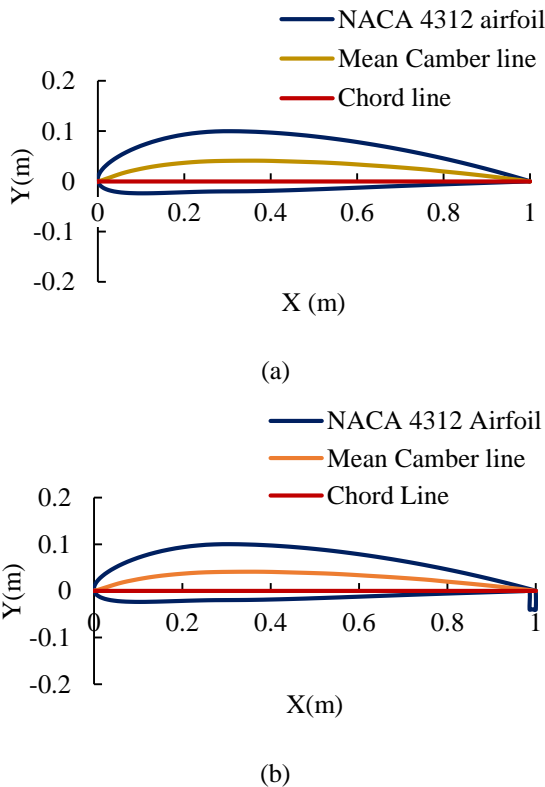


Fig. 1 (a) NACA 4312 airfoil; (b) NACA 4312 with flap.

2.2 Governing Equations

Several types of turbulence models are generally used to solve according to the type of flow like $k - \omega$ SST and $k - \epsilon$ etc. $k - \epsilon$ is more suitable for flow away from the wall, while $k - \omega$ SST model is best suited for near the wall flow region, where adverse pressure gradient is developed. $k - \omega$ SST model shows better numerical analysis and results than $k - \epsilon$ model [21].

$k - \omega$ SST model is a two equation eddy viscosity model which is constructed upon conservation of mass, momentum and energy accompanied by two additional transport equations to characterize the turbulent properties model. It is a hybrid model combining the Wilcox $k - \omega$ and the $k - \epsilon$ models.

The continuity model:

$$\frac{\partial}{\partial x_i}(\rho u_i) = 0 \tag{1}$$

The momentum model:

$$\begin{aligned} \frac{\partial}{\partial x_j}(\rho u_i u_j) = \frac{\partial p}{\partial x_i} \\ + \frac{\partial}{\partial x_j} \left[\mu \left(\frac{\partial u_i}{\partial x_j} + \frac{\partial u_j}{\partial x_i} - \frac{2}{3} \delta_{ij} \frac{\partial u_l}{\partial x_l} \right) \right] \\ + \frac{\partial}{\partial x_j}(-\rho \overline{u_i' u_j'}) \end{aligned} \tag{2}$$

Here in Equations (1) and (2), ρ denotes density, μ denotes dynamic viscosity and u denotes inlet velocity of the fluid.

The turbulent kinetic energy and dissipation rate of eddy viscosity are represented by k and ω respectively. These are gained from Equations (3) and (4):

$$\begin{aligned} \frac{\partial}{\partial t}(\rho k) + \frac{\partial}{\partial x_i}(\rho k u_i) \\ = \frac{\partial}{\partial x_j} \left(\Gamma_k \frac{\partial k}{\partial x_j} \right) + \tilde{G}_k - Y_k + S_k \end{aligned} \tag{3}$$

and

$$\begin{aligned} \frac{\partial}{\partial t}(\rho \omega) + \frac{\partial}{\partial x_i}(\rho \omega u_i) \\ = \frac{\partial}{\partial x_j} \left(\Gamma_\omega \frac{\partial \omega}{\partial x_j} \right) + G_\omega - Y_\omega + D_\omega \\ + S_\omega \end{aligned} \tag{4}$$

In these equations, \tilde{G}_k represents the generation of turbulence kinetic energy due to mean velocity gradients. G_ω represents the generation of ω . Γ_k and Γ_ω represent the effective diffusivity of k and ω . Y_ω and Y_k represent the dissipation of k and ω due to turbulence. D_ω represents the cross-diffusion term, calculated as described below S_ω and S_k are user-defined source terms. As the flow was considered to be incompressible, the energy equation was not required for the present study.

2.3 Boundary Condition with Domain

The domain was designed with a semicircle and rectangle. The upstream, upper and lower domain were 12.5C away and the downstream was 20C away (C is referred as chord length) to reduce the boundary effect.

Fig. 2 shows the domain taken for the airfoil. Based on geometry ABCDE, BCD was set as constant velocity inlet and

AE as a pressure outlet. The airfoil wall as well as flap were assumed with no slip boundary condition. The Reynolds No was fixed at 5×10^5 , the inlet velocity is assumed 7.5 m/s which directed to a Mach number less than 0.3. For this low Mach number, the flow was deliberated to be incompressible. With different angle of attack, the components of velocity was measured using $u \sin \alpha$ and $u \cos \alpha$ (where u is the free stream velocity of the flow and α is the corresponding AoA). Air was assumed as an ideal fluid with a constant density of 1.225 kg/m^3 and dynamic viscosity of $1.7894 \times 10^{-5} \text{ kg/m-s}$.

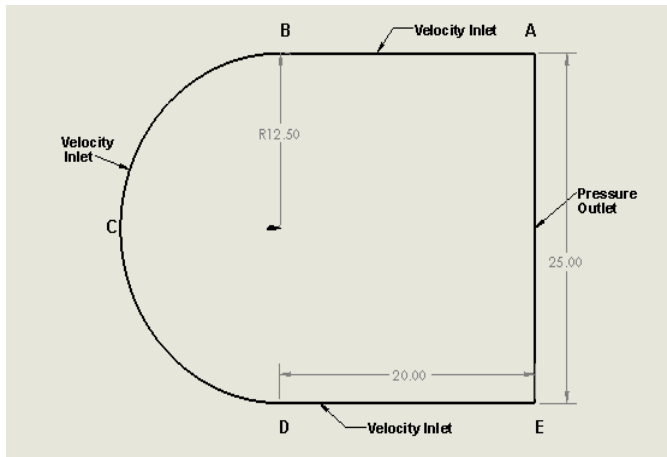


Fig. 2 Computational Domain with Boundary condition

2.4 Numerical Setup

In FLUENT, the governing equations were discretized using a second-order upwind scheme and the solver of these equations was run on pressure based Coupled algorithm. This method obtained a greater performance compared to segregated solution schemes [22]. Instead of rotating the airfoil, the flow direction of air was inclined along the increasing angle of attack. The convergence criterion was set as $1e-07$ and double precision was fixed for accuracy. The steady-state Reynolds Average Navier-Stokes (RANS) equation was deciphered using the Least squares cell based gradient option and pressure-based solver was chosen.

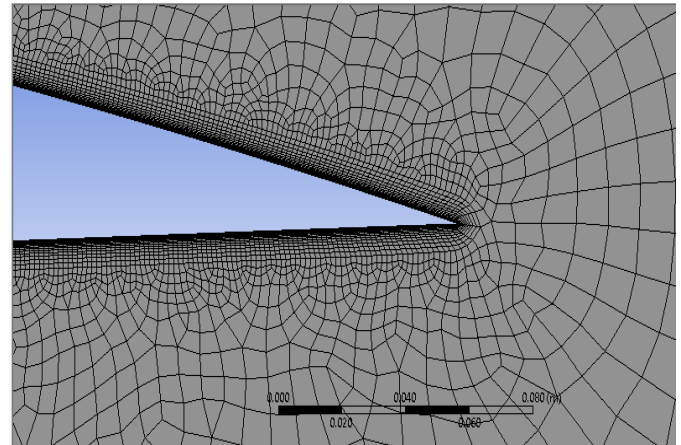
2.5 Mesh Generation

Mesh generation is very important aspect for CFD simulation. Mesh or grid is used for better convergence properties. The element and nodal data achieved from this discretization is beneficial for the numerical results of Finite Element Method (FEM) and for the aerodynamic investigation. As the geometry was complicated unstructured mesh was selected for grid generation which had been done in ANSYS Meshing. Fig. 3 presents an augmented view of the mesh structure of without flap and 3% flap. In Fig. 3(a) finer mesh is apparent close to the surface of the airfoil and trailing edge, and in Fig. 3(b) around the flap by introducing inflation layer to achieve suitable resolution of the boundary layer and the area around the Gurney flap. For inflation, 16 layers were considered for a good mesh and maximum thickness of Inflation had been used 0.007m. Higher mesh resolution had been used near leading edge and trailing edge. By changing the edge sizing and body sizing, element numbers and node numbers had been varied to find proper mesh for accurate result.

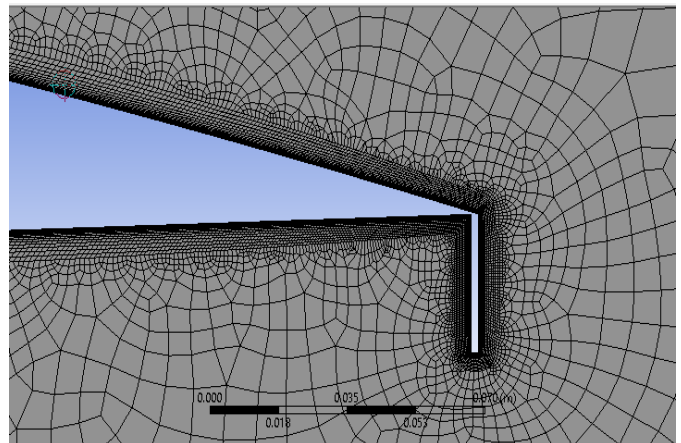
The non-dimensional wall parameter is defined as:

$$Y^+ = y \times \frac{\sqrt{(\tau_w)/\rho}}{\mu} \quad (5)$$

where, y is the distance from the wall to the centroid of the wall adjacent first cell and τ_w is the wall shear stress. From reference [22] to acquire accurate simulation result, $Y^+ \sim 1$ was recommended which denotes finer mesh in the near wall region. For each simulation of airfoil with and without flap the anticipated Y^+ value was detected.



(a)

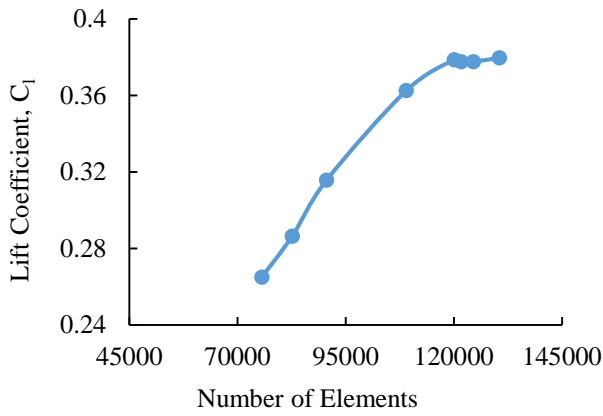


(b)

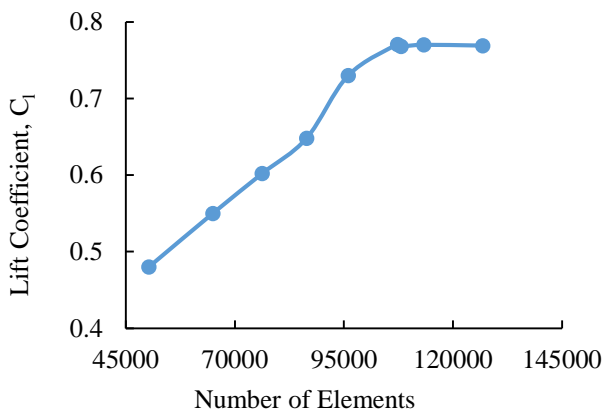
Fig. 3 Mesh Generated around (a) without flap (b) with 3% flap

2.6 Mesh Independence Test

Mesh independence test were performed to evaluate the most optimized mesh to obtain a precise numerical result. For this study a set of simulations were conducted to get the optimized mesh. The refinement had been achieved by altering the body sizing and edge sizing for each mesh. Fig. 4(a) shows the effect of mesh elements on the lift coefficient of NACA-4312 airfoil without flap at angle of attack 0° . Results demonstrate that mesh with elements number higher than 120055 could produce a mesh independent result. Fig. 4(b) demonstrates the effect of mesh element number on the lift coefficient of NACA-4312 with 1.5% C flap and AoA is 0° . It is evident from the graph that mesh with elements number higher than 108000 the lift coefficient becomes constant. So, the mesh with 108000 elements was considered for the numerical simulation of NACA-4312 airfoil with flap.



(a)



(b)

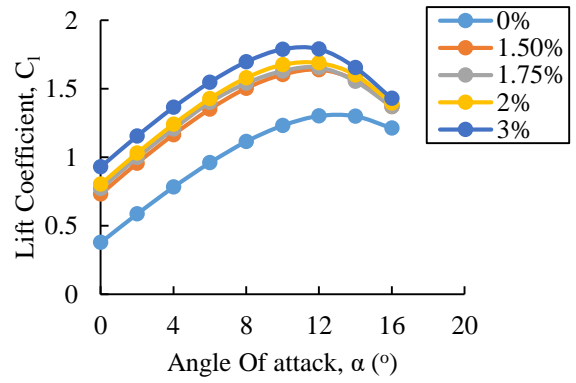
Fig. 4 Variation of Lift coefficient with Number of elements (a) without flap at 0° AoA (b) with 1.5% flap, 0° AoA

3 Results and Discussion

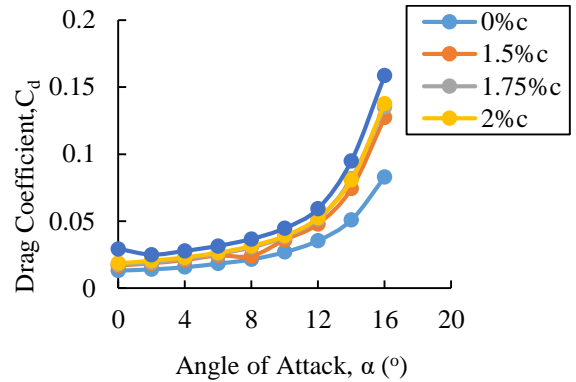
Fig. 5(a) depicts the relation between lift coefficient and AoA for different flap height. It had been observed from the figure that the lift coefficient, C_l , increases up to 10°-12° and then starts to fall due to flow separation which is caused by adverse pressure gradient at the trailing edge. This phenomenon is known as stall. It was also observed that airfoil with gurney flap showed a significant jump on lift coefficient at all corresponding angle of attack. Higher flap height have higher lift coefficient. In this graph it is perceived that 3%C flap produced the highest lift coefficient and the lowest lift coefficient is produced by the airfoil without flap.

Fig. 5(b) shows the relation between drag coefficient and angle of attack. It was perceived from the graph that drag increased very slowly at lower angle of attack however behind the stall angle due to the flow separation drag increased suddenly. Results also demonstrated that drag coefficient increases with increasing lengths of gurney flap. The airfoil with 3%C flap showed the sharpest increase of drag around stall.

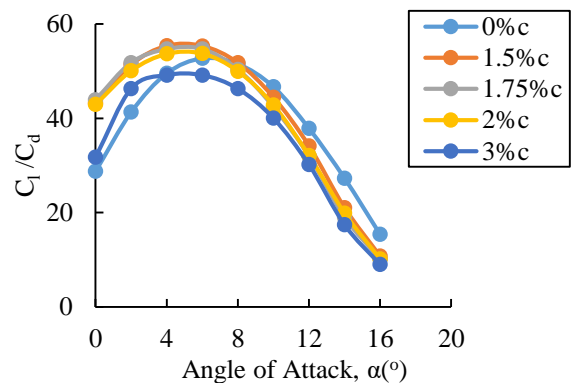
As the lift and drag both increase along with the increasing AoA, it is more efficient to calculate the C_l/C_d value and it was depicted in Fig. 5(c). Initially the graph showed a positive slope but after reaching a maximum value it dropped which signified that the rate of increasing lift is slower than the rate of increasing drag causing a major drawback in airfoil efficiency. The airfoil with 1.5%C flap showed the most efficient result while flap with 3%C showed drastic case of drag increment.



(a)



(b)



(c)

Fig. 5 Relation between (a) Lift Coefficient vs Angle of Attack; (b) Drag Coefficient vs Angle of Attack; and (c) C_l/C_d vs Angle of Attack for various length of flap

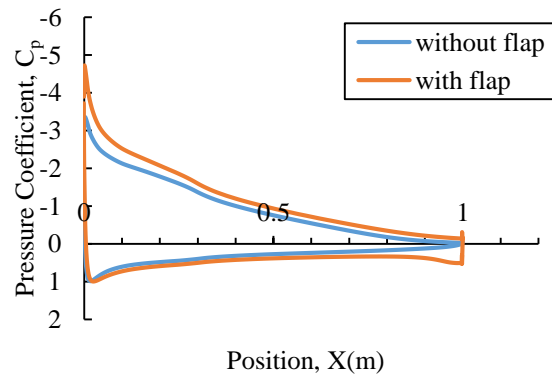
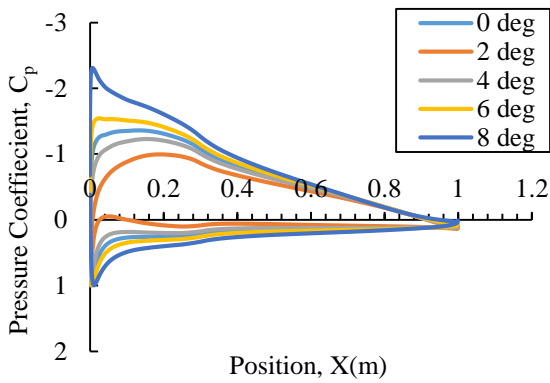
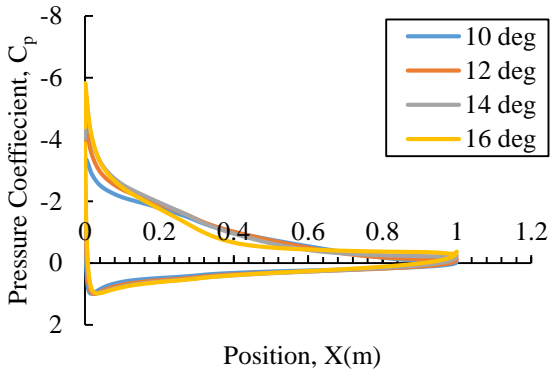


Fig. 6 Variation of Pressure Coefficient with position on airfoil surface for without flap and with flap at 10° AoA

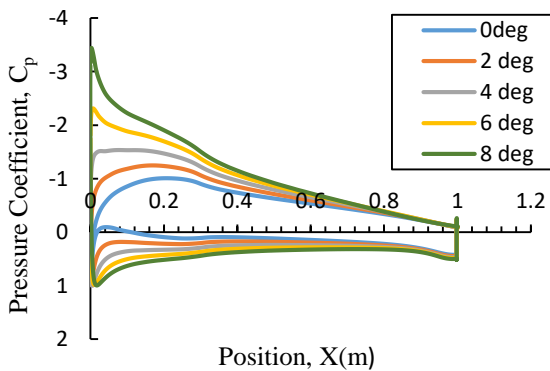


(a)

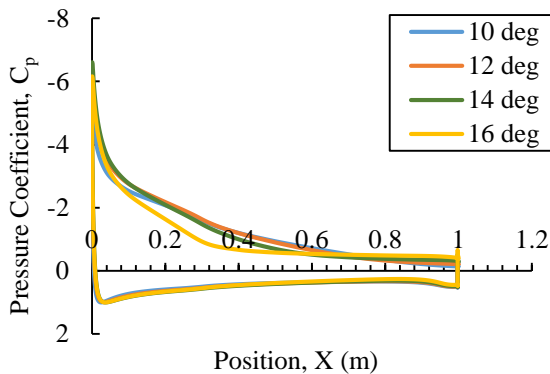


(b)

Fig. 7 Variation of Pressure Coefficient with position on airfoil surface for without flap at different AoA



(a)



(b)

Fig. 8 Variation of Pressure Coefficient with position on airfoil surface for with 1.5%C flap at different AoA

Fig. 6 displays the relation between pressure coefficient and the position along the chords for airfoil without flap and with 1.5%c flap at 10° AoA. The high pressure coefficient had been observed for the lower surface of the airfoil and the lower pressure coefficient surface denoting the upper surface of the airfoil. Because of this pressure difference the airfoil can generate lift. The pressure alteration between upper and lower surface rose largely in the trailing edge section of the airfoil due to the flap. From Fig. 6 it has been seen that for airfoil without flap at $\alpha = 10^\circ$ the flow separation occurs in 86%C. For same angle of attack, flow separation took place at 92%C when the gurney flap is attached with the airfoil. From Fig. 6 it can be seen that the difference of pressure co-efficient between upper and lower surface is greater for the airfoil with gurney flap than the clean airfoil. As the flow separation occurred late in the gurney flap case, the lift increment occurred in airfoil with gurney flap.

As is depicted in Fig. 7(a), at $\alpha=0^\circ$, 13.2%C of the upper surface from leading edge has undergone favorable pressure gradient. After that, the air moves fluently over the upper surface without being separated. With increasing AoA, the leading edge suction is enhanced, but the favorable pressure gradient is decreased for $\alpha = 4^\circ$. In Fig. 7(a), the leading edge suction was enhanced again, and the suction side of the airfoil had undergone adverse pressure gradient after 0.7%C of the upper surface at $\alpha=8^\circ$. As a result, flow started to separate at 91%C. In the separation zone, the pressure remained constant. From Fig. 8(b), the separation point for $\alpha = 12^\circ$ occurred in 75%C in clean airfoil. But from Fig. 8(b), for same angle of attack the separation delayed to 78%C in airfoil with gurney flap. $\alpha = 12^\circ$ is the stall angles for the airfoil with 1.5%C gurney flap and clean airfoil respectively. As after stall angles, lift decreased and the drag increased, the separation point for airfoil with gurney flap had been seen at 53%C for $\alpha = 14^\circ$ from Fig. 8(b) where the separation point for clean airfoil had been seen at 60%C for same angle of attack from Fig. 7(b). Flow separation is occurred in the pressure side of the airfoil close to the trailing edge and before the GF creating a huge recirculation region, causing an increment in pressure. Pressure co-efficient is observed maximum for all simulations at leading edge stagnation point as the local velocity becomes zero there. When AoA increased, the stagnation point shifted behind along the lower surface causing a nose-up pitching moment. Highest pressure co-efficient had been perceived in lower surface graph. Fig. 9 depicts the flow separation point is delayed for airfoil with flap up to stall angle.

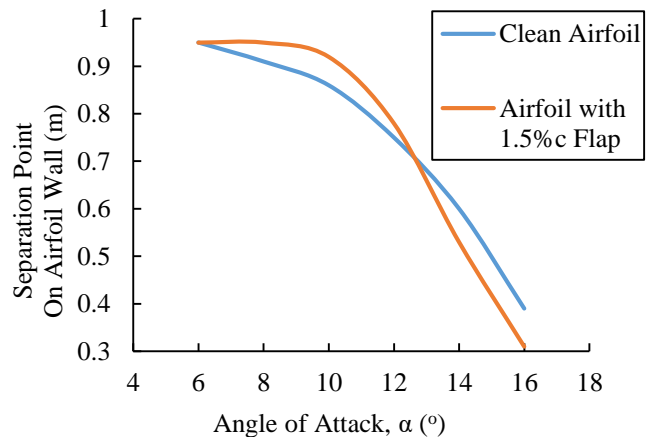


Fig. 9 Separation Point on airfoil wall for different AoA for clean and with 1.5%C flap airfoil

Fig. 10 presents the pressure distribution on the airfoil with various height of gurney flap at 10° AoA. The Kutta condition at the trailing edge is changed by deploying a GF which leads to a pressure increment for both the upper and lower airfoil surface. As there is a pressure difference between upper and lower surface, the load capacity of the airfoil rises resulting increment in lift. With increasing height of gurney flap the lift coefficient also increases.

From Fig. 11 it is quite evident that the upper surface of the airfoil had lesser pressure than the lower surface. At moderate AoA, the pressure on both surfaces were increased and thus the lift as well as drag also increased, which then bring about the decreasing nature of lift to drag ratio. Also, from the pressure contour it is observed that the front side of the GF had positive pressure and the rear side had negative pressure, resulting the increment of drag of the airfoil.

3.1 Trailing Edge Flow Structure

In Fig. 12(a) flow behavior of airfoil without flap with AoA of 4° is shown and Fig. 12(b) depicts the flow behavior of airfoil with flap 1.5% with angle of attack 4° . At this angle of attack, the flow created two vortices, one is at the downstream of the flap and the other one is at the upstream creating the separation bubble. At lower angle of attack, one very strong anti-clockwise vortex is created down the stream of the GF and no contra rotating distinct vortices was seen. This vortex induces the wake region to proceed downstream which results in delaying the flow separation and the reduction of pressure due to the vortices results in increasing the suction. At the lower surface upstream of the flap velocity is decreased which causes in pressure increase and this adds to the rise of the suction in the downstream resulting the increment of lift.

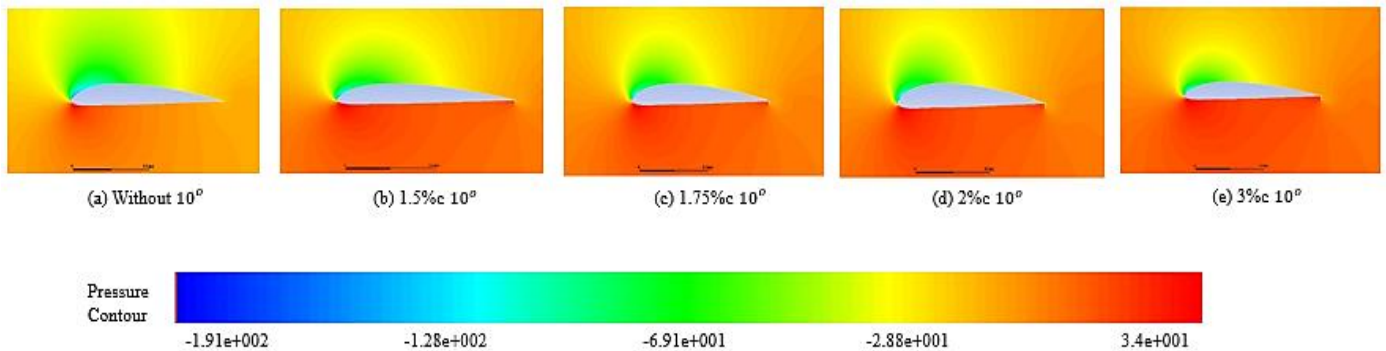


Fig. 10 Pressure contour of airfoil with different height of flap at 10° angle of attack

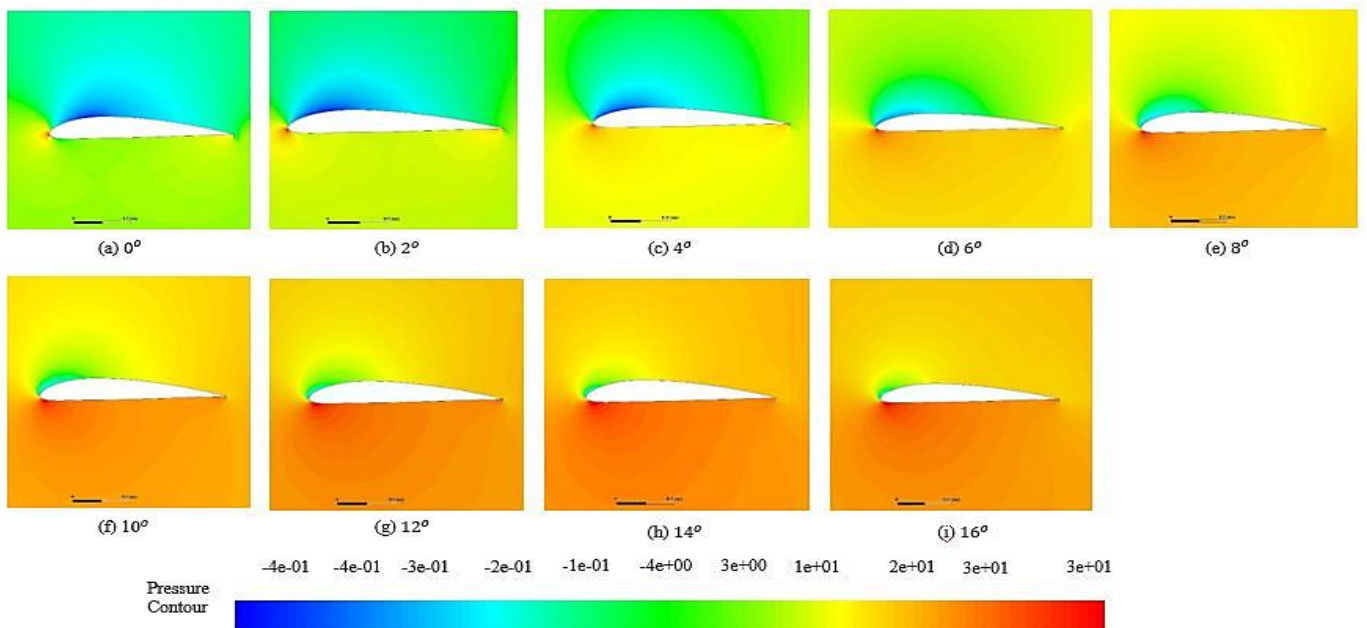


Fig. 11 Pressure contour of airfoil with 1.5%C flap at different angle of attack

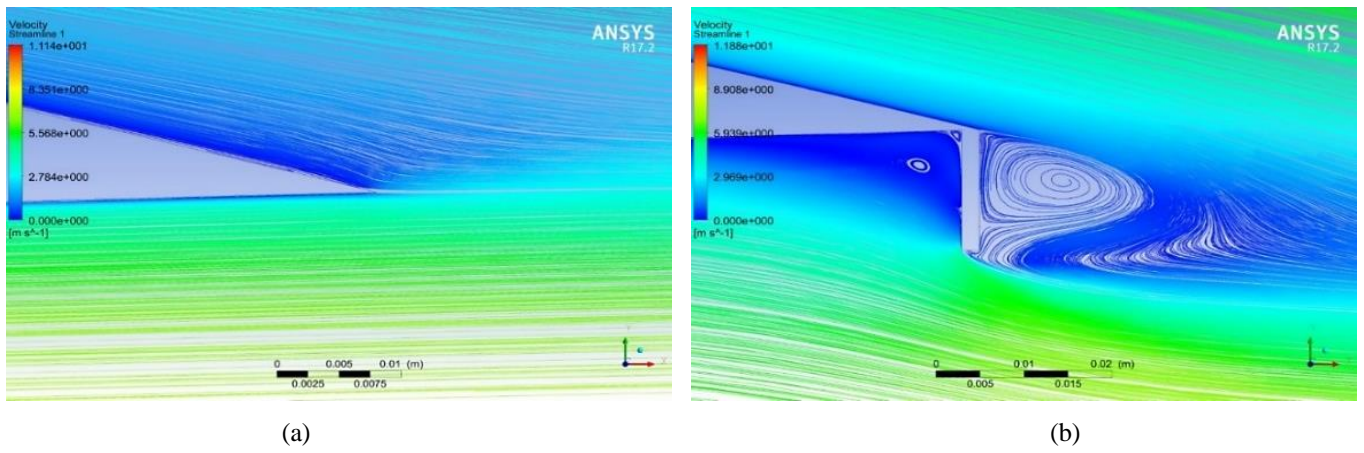


Fig. 12 Flow behavior of (a) without flap and (b) with flap at AoA 4° at the trailing edge

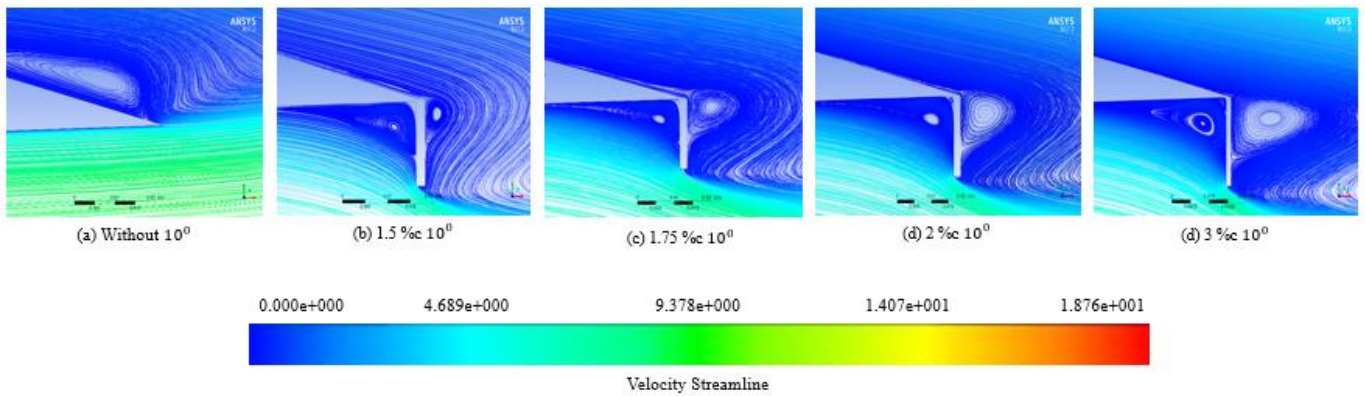


Fig. 13 Velocity Streamlines of airfoils with 1.5%C flap (left column) and without flap (right column)

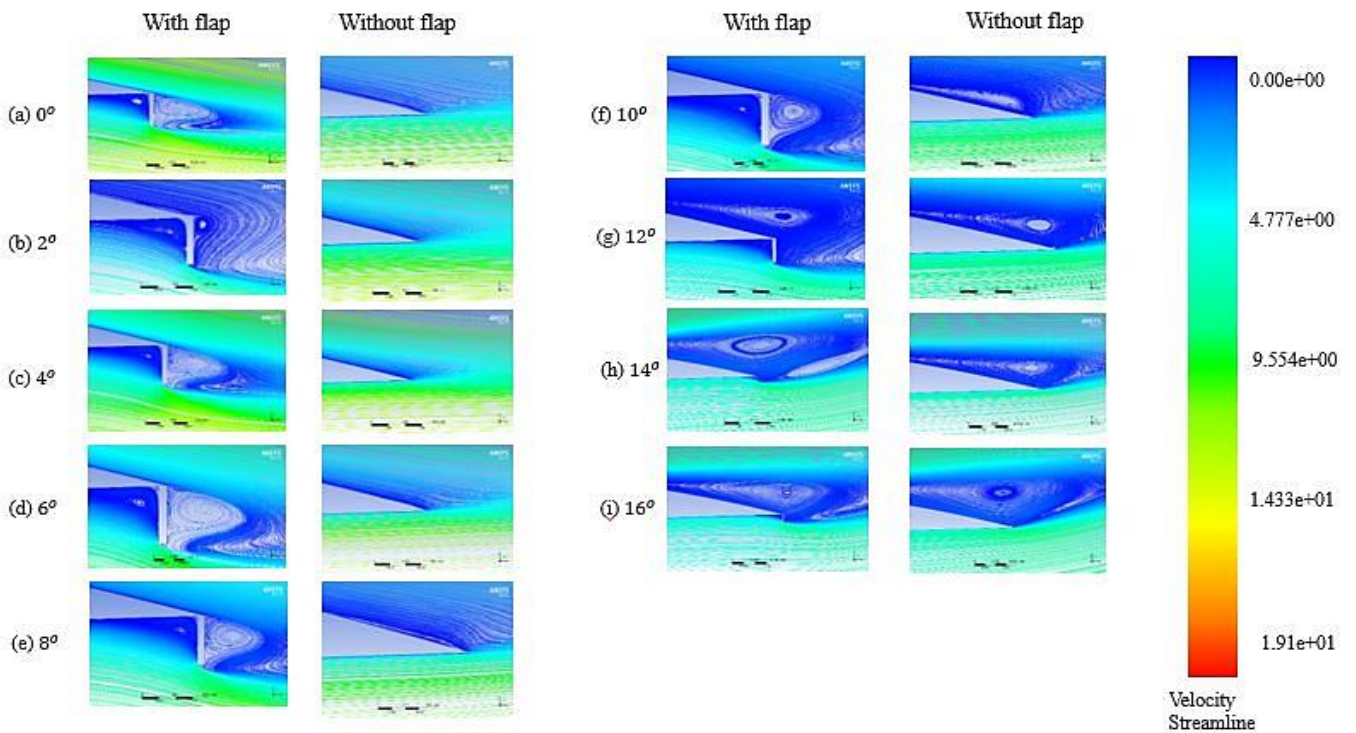


Fig. 14 Velocity Streamlines of airfoils with flap of different heights and without flap

In Fig. 13 it had been depicted the differences of flow behavior between an airfoil with flap and without flap with increasing angle of attack. Fig. 13 shows that the air moves fluently without separation for clean airfoil at $\alpha = 4^\circ$. In

downstream of the leeward of the GF, there is a wake region with two vortices. Since GF has effects as a point vortex, it enlarges the circulation of the airfoil. However, when a GF had been installed, the flow separation on the upper surface is reduced so

that the suction is greater and vortex creation behind the flap which results the delay of flow separation. At higher AoA (for airfoil with flap) these vortices move to the upper surface of the airfoil enhancing the lift to drag ratio which is quite equal as the airfoil without flaps. From Fig. 14 flow structure had been showed for different height of the gurney flap at angle of attack 10° . It clearly shows that the flow separation is occurring lately. With the increasing height the vortex after the gurney flap is getting bigger and clear.

4 Conclusion

A CFD analysis of a NACA 4312 airfoil with a Gurney flap has been done precisely. The two-dimensional flow was measured using ANSYS Fluent with the two-equation turbulence model of K-omega SST. The main intention of using the gurney flap is lift increment. Gurney flap can produce the same lift with lesser AoA. In comparison with a clean airfoil, lift coefficient and lift to drag ratio were enhanced by the Gurney flaps. By deploying gurney flap at trailing edge, flow can be optimized for anticipated flow behavior. So gurney flap can be used as lift-enhancement device. Along with the increment of the height of the flap, lift as well as drag increases but the aerodynamics performance is not always up to the mark. It was inspected that the relation between Lift/drag ratio and gurney flap length is non-linear and it relied on the angle of attack. The maximum value of Lift/drag ratio is attained with Gurney flap of 1.5%C which is considered as the best performance for this study. The contours of static pressure, velocity and the coefficient of lift, coefficient of drag distribution and coefficient of pressure is calculated. Outcomes from this research can be utilized as a path for achieving higher lift on aircraft by using GF.

References

- [1] Kumar, A., Chaubdar, P., Sinha, G.S. and Harichandan, A.B., 2021. Performance Analysis of NACA4412 Airfoil with Gurney Flap. In *Proceedings of International Conference on Thermofluids* (pp. 167-176). Springer, Singapore.
- [2] Jang, C.S., Ross, J.C. and Cummings, R.M., 1998. Numerical investigation of an airfoil with a Gurney flap. *Aircraft Design*, 1(2), pp.75-88.
- [3] Fatahian, H., Salarian, H., Nimvari, M.E. and Khaleghinia, J., 2020. Effect of Gurney flap on flow separation and aerodynamic performance of an airfoil under rain and icing conditions. *Acta Mechanica Sinica*, pp.1-19.
- [4] Liebeck, R.H., 1978. Design of subsonic airfoils for high lift. *Journal of Aircraft*, 15(9), pp.547-561.
- [5] Neuhart, D.H., 1988. A water tunnel study of Gurney flaps (Vol. 4071). *National Aeronautics and Space Administration, Scientific and Technical Information Division*.
- [6] Zerihan, J. and Zhang, X., 2001. Aerodynamics of Gurney flaps on a wing in ground effect. *AIAA Journal*, 39(5), pp.772-780.
- [7] Yoo, N.S., 2000. Effect of the Gurney flap on a NACA 23012 airfoil. *KSME International Journal*, 14(9), pp.1013-1019.
- [8] Li, Y., Wang, J. and Zhang, P., 2002. Effects of Gurney flaps on a NACA0012 airfoil. *Flow, Turbulence and Combustion*, 68(1), pp.27-39.
- [9] Fernandez-Gamiz, U., Zulueta, E., Boyano, A., Ansoategui, I. and Uriarte, I., 2017. Five megawatt wind turbine power output improvements by passive flow control devices. *Energies*, 10(6), p.742.
- [10] Aramendia, I., Saenz-Aguirre, A., Fernandez-Gamiz, U., Zulueta, E., Lopez-Guede, J.M., Boyano, A. and Sancho, J., 2018. Gurney Flap Implementation on a DU91W250 Airfoil. In *Multidisciplinary Digital Publishing Institute Proceedings* (Vol. 2, No. 23, p. 1448).
- [11] Graham, M., Muradian, A. and Traub, L.W., 2018. Experimental study on the effect of Gurney flap thickness on airfoil performance. *Journal of Aircraft*, 55(2), pp.897-904.
- [12] Jain, S., Sitaram, N. and Krishnaswamy, S., 2015. Computational investigations on the effects of Gurney flap on airfoil aerodynamics. *International Scholarly Research Notices*, 2015.
- [13] Storms, B.L. and Jang, C.S., 1994. Lift enhancement of an airfoil using a Gurney flap and vortex generators. *Journal of Aircraft*, 31(3), pp.542-547.
- [14] Myose, R., Papadakis, M. and Heron, I., 1998. Gurney flap experiments on airfoils, wings, and reflection plane model. *Journal of Aircraft*, 35(2), pp.206-211.
- [15] Cole, J.A., Vieira, B.A., Coder, J.G., Premi, A. and Maughmer, M.D., 2013. Experimental investigation into the effect of Gurney flaps on various airfoils. *Journal of Aircraft*, 50(4), pp.1287-1294.
- [16] Ahmed, M.R., Takasaki, T. and Kohama, Y., 2007. Aerodynamics of a NACA4412 airfoil in ground effect. *AIAA Journal*, 45(1), pp.37-47.
- [17] Webb, J., Higgenbotham, H., Liebshutz, D., Potts, D., Tondreau, E. and Ashworth, J., 2001. Analysis of Gurney Flap effects on a NACA 0012 airfoil/wing section. In *19th AIAA Applied Aerodynamics Conference* (p. 2483).
- [18] M. E. Camocardi, J. Maranon, D. Leo, J. S. Delnero, and J. L. C. Lerner, "Gurney Flap," vol. 47, no. January, pp. 1-15, 2011.
- [19] Maughmer, M.D. and Bramesfeld, G., 2008. Experimental investigation of Gurney flaps. *Journal of Aircraft*, 45(6), pp.2062-2067.
- [20] Chand, D.V., Sriram, R. and Kumar, D.U., 2016. Aerodynamic analysis of multi element airfoil. *Int J Sci Res Publ*, 6(7), pp. 305-310.
- [21] Pranto, M.R.I. and Inam, M.I., 2020. Numerical Analysis of the Aerodynamic Characteristics of NACA4312 Airfoil. *Journal of Engineering Advancements*, 1(02), pp.29-36.
- [22] Fluent, A.N.S.Y.S., 2013. ANSYS fluent theory guide 15.0. ANSYS, Canonsburg, PA, 33.

Quartic Non-polynomial Spline Method for Singularly Perturbed Differential-difference Equation with Two Parameters

Gemadi Roba Kusi, Tesfaye Aga Bullo*, and Gemechis File Duressa

Department of Mathematics, Jimma University, Jimma, P.O. Box 378, Ethiopia

Received: March 15, 2021, Revised: April 27, 2021, Accepted: April 29, 2021, Available Online: May 03, 2021

ABSTRACT

Quartic non-polynomial spline method is presented to solve the singularly perturbed differential-difference equation containing two parameters. The considered equation is transformed into an asymptotical equivalent differential equation, and the derivatives are replaced finite difference approximation using the quartic non-polynomial spline method. The convergence analysis of the method has been established. Numerical experimentation is carried out on model examples, and the results are presented both in tables and graphs. Furthermore, the present method gives a more accurate solution than some existing methods reported in the literature.

Keywords: Quartic non-polynomial, differential-difference, two-parameters, accurate solution.



This work is licensed under a [Creative Commons Attribution-Non Commercial 4.0 International License](https://creativecommons.org/licenses/by-nc/4.0/).

1 Introduction

Numerical analysis is both a science and an art. As a science, it is concerned with the processes by which mathematical problems can be solved by appropriate methods. While, as an art numerical analysis is concerned with choosing that procedure that is suitable for the solution of a particular problem. Numerical answers to a problem generally cover errors that arise in inherent in the mathematical formulation of the problem or approximate to the physical situation and suffered in finding the solution numerically. If the small positive constant number multiplies with the highest-order derivative of a given differential equation, then the obtained equation is known as a singularly perturbed differential equation. The small positive parameter is known as the perturbation parameter. In singular perturbation theory, the study of differential equations which are modified by the addition of small coefficients multiplying the higher-order derivative is of importance in many fields, [1]-[5].

Singular perturbation problems are the differential or difference equations that arise as a result of the modeling of real-life phenomena and whose solutions exhibit the boundary layer. Based on the parameters, the perturbation and/or delay parameters they involved, singularly perturbed problems can be categorized into the singularly perturbed differential equations or singularly perturbed differential-difference equations. Many researchers, like in, [7]-[16] have been providing different numerical methods for solving singularly perturbed differential-difference equations. But, most of those author's considered the stated problem when it involves one perturbation parameter. Few scholars like in [9],[14],[17] have been developed numerical schemes to solve singularly perturbed problems with two parameters. For the problems that contain two perturbation parameters and involve delay term in the convection term proposed by Sahu and Mohapatra, [9] who tried to develop a parameter uniform numerical method.

However, this developed method and most of the classical methods produce good results only when the perturbation parameter in the convection term μ is much less than the

perturbation parameter in the diffusion coefficient ϵ , (i.e., $\mu \ll \epsilon$). This difficulty is caused due to μ in convection term which implies the existence of the two boundary layers in the solution. Moreover, classical numerical methods give good accurate solutions only when the step length the solution domain $h < \epsilon$. This leads to huge systems of equations which is costly to solve. Thus, in this paper, we present a quartic non-polynomial spline method that produces a more accurate solution for singularly perturbed differential-difference equations involving two parameters when $\epsilon \leq \mu \leq h$.

2 Description of the Numerical Method

We consider the singularly perturbed differential-difference equation with two parameters of the form:

$$\epsilon y''(x) + \mu a(x)y'(x - \delta) - b(x)y(x) = g(x), \quad (1)$$

$$x \in \Omega = (0, 1)$$

with the interval and boundary condition:

$$y(x) = \phi(x), \quad -\delta \leq x \leq 0, \quad y(1) = \beta. \quad (2)$$

where $0 < \epsilon, \mu \ll 1$ are the perturbation parameters. The delay parameter is δ , and satisfies $\delta < \epsilon$. Functions $a(x), b(x), g(x)$ and $\phi(x)$ are continuous on Ω , and the constant number β is given. Furthermore, assume that $a(x) \geq a > 0$ and $b(x) \geq b > 0, \forall x \in \bar{\Omega}$.

By Taylor's series expansion as:

$$y'(x - \delta) = y'(x) - \delta y''(x) + O(\delta^2) \quad (3)$$

Substituting Eq. (3) into Eq. (1), gives the asymptotical equivalent boundary value problem:

$$\epsilon y''(x) + \mu p(x)y'(x) - q(x)y(x) = f(x) \quad (4)$$

with the boundary conditions,

$$y(0) = \phi_0 = \phi(x_0), \quad y(1) = A \tag{5}$$

where: $p(x) = \frac{\epsilon a(x)}{\epsilon - \delta \mu a(x)}$, $q(x) = \frac{\epsilon b(x)}{\epsilon - \delta \mu a(x)}$, and

$$f(x) = \frac{\epsilon g(x)}{\epsilon - \delta \mu a(x)}.$$

Consider for $0 < p_0 \leq p(x) \leq p_1$ and $q(x) \geq q \geq 0$, the homogenous part of Eq. (4) is written as;

$$\epsilon y''(x) + \mu p_1 y'(x) - qy(x) = 0 \tag{6}$$

The characteristic equation of Eq. (6) is $\epsilon m^2 + \mu p_1 m - q = 0$, and assume it has two real solution

$$m_{1,2} = \frac{-\mu p_1 \pm \sqrt{(\mu p_1)^2 + 4\epsilon q}}{2\epsilon}.$$

The situation of the layer is characterized by the case, for $\epsilon \ll \mu$, as $\mu \rightarrow 0$, and $q \geq 0$ which suggests that

$$m_1 \approx \frac{-\mu p_1}{\epsilon} \text{ and } m_2 \approx 0.$$

Hence, in this case for $\epsilon \ll \mu$, the complementary solution to Eq. (6) is

$$y(x) = C_1 + C_2 e^{\frac{-\mu p_1 x}{\epsilon}}, \tag{7}$$

where C_1 and C_2 are arbitrary constants.

Let N be a positive integer and a uniform mesh Δ with nodal point x_i on $[0,1]$ such that:

$$\Delta : 0 = x_0 < x_1 < x_2 < \dots < x_{N-1} < x_N = 1,$$

$$x_i = ih, i = 0, 1, 2, \dots, N; \text{ where } h = \frac{1}{N}, \text{ and } N \text{ is the}$$

number of intervals. For each segment $[x_i, x_{i+1}]$, $i = 1, 2, \dots, N-1$, let us the non-polynomial

quartic spline $S_\Delta(x)$ defined by:

$$S_\Delta(x) = a_i \sin k(x - x_i) + b_i \cos k(x - x_i) + c_i(x - x_i)^2 + d_i(x - x_i) + e_i, \tag{8}$$

where a_i, b_i, c_i, d_i and e_i are real finite constants to be determined and k is an arbitrary parameter that will be used to increase the accuracy of the method. Denoting y_i be an approximation to $y(x_i)$ obtained by the segments $S_\Delta(x)$ of the spline function passing through the points (x_i, S_Δ) and $(x_{i+1}, S_{\Delta+1})$. To determine the coefficients of Eq. (8), we do not only require that $S_\Delta(x)$ satisfies interpolator conditions at x_i and x_{i+1} but also continuity condition of the first, and the third derivatives at the nodes (x_i, S_Δ) and $(x_{i+1}, S_{\Delta+1})$. Symbolizing:

$$\begin{aligned} S_\Delta(x_i) &= y_i, & S_\Delta(x_{i+1}) &= y_{i+1} \\ S''_\Delta(x_i) &= M_i, & S''_\Delta(x_{i+1}) &= M_{i+1} \\ S^{(4)}_\Delta(x_i) &= \frac{1}{2}(F_i + F_{i+1}) \end{aligned} \tag{9}$$

We get through a long straightforward calculation,

$$\begin{aligned} a_i &= \frac{1}{k^2 \sin \theta} (M_i - M_{i+1}) + \frac{1 - \cos \theta}{2k^4 \sin \theta} (F_i + F_{i+1}), \\ b_i &= \frac{F_i + F_{i+1}}{2k^4}, \\ c_i &= \frac{M_i}{2} + \frac{F_i + F_{i+1}}{4k^2}, \\ d_i &= \frac{1}{h} (y_{i+1} - y_i) - \left(\frac{1}{hk^2} + \frac{h}{2} \right) M_i + \frac{1}{hk^2} M_{i+1} - \frac{h}{4k^2} (F_i + F_{i+1}), \\ e_i &= y_i - \frac{1}{2k^4} (F_i + F_{i+1}). \end{aligned}$$

Expanding the continuity condition of the first derivatives at knots, $S'_{\Delta-1}(x_i) = S'_\Delta(x_i)$, leads to:

$$\begin{aligned} \frac{4hk^3 \sin \theta}{2(1 - \cos \theta) - hk \sin \theta} \left[\frac{y_{i-1} - 2y_i + y_{i+1}}{h^2} \right] + \\ (F_{i-1} + F_{i+1}) + 2F_i = \frac{2k(2hk \cos \theta + h^2 k^2 \sin \theta - 2 \sin \theta)}{h[2(1 - \cos \theta) - hk \sin \theta]} M_{i-1} + \\ \frac{2k(4 \sin \theta + h^2 k^2 \sin \theta - 2hk(\cos \theta + 1))}{h[2(1 - \cos \theta) - hk \sin \theta]} M_i + \\ \frac{4k(hk - \sin \theta)}{h[2(1 - \cos \theta) - hk \sin \theta]} M_{i+1}. \end{aligned} \tag{10}$$

Likewise, using the continuity of the third derivatives at knots, $S'''_{\Delta-1}(x_i) = S'''_\Delta(x_i)$, we get:

$$(F_{i-1} + F_{i+1}) + 2F_i = \frac{2k^2 \cos \theta}{1 - \cos \theta} M_{i-1} - \frac{2k^2(\cos \theta + 1)}{1 - \cos \theta} M_i + \frac{2k^2}{1 - \cos \theta} M_{i+1} \tag{11}$$

By substituting Eq. (11) into (10), we get the system:

$$\frac{y_{i-1} - 2y_i + y_{i+1}}{h^2} = \alpha(M_{i-1} + M_{i+1}) + 2\beta M_i, \tag{12}$$

where, $i = 1, 2, \dots, N-1$,

$$\alpha = \frac{\theta^2 - 2(1 - \cos \theta)}{2\theta^2(1 - \cos \theta)} \text{ and } \beta = \frac{4(1 - \cos \theta) + \theta^2(1 - 3\cos \theta)}{4\theta^2(1 - \cos \theta)}.$$

If $h \rightarrow 0$, then $\theta = hk \rightarrow 0$. Thus using L'Hospital's rule we have $\lim_{\theta \rightarrow 0} \alpha = \frac{1}{12}$ and $\lim_{\theta \rightarrow 0} \beta = \frac{5}{12}$.

Using the splines second derivatives in Eqs. (9) with (4), we have

$$\begin{aligned} M_i &= \frac{1}{\epsilon} (f_i - \mu p_i y'_i + q_i y_i), \\ M_{i-1} &= \frac{1}{\epsilon} (f_{i-1} - \mu p_{i-1} y'_{i-1} + q_{i-1} y_{i-1}), \\ M_{i+1} &= \frac{1}{\epsilon} (f_{i+1} - \mu p_{i+1} y'_{i+1} + q_{i+1} y_{i+1}). \end{aligned} \tag{13}$$

For the first-order derivatives in Eq. (13), we consider the central finite difference approximation of the form:

$$y'_i = \frac{y_{i+1} - y_{i-1}}{2h}, \quad y'_{i-1} = \frac{-3y_{i-1} + 4y_i - y_{i+1}}{2h},$$

$$y'_{i+1} = \frac{y_{i-1} - 4y_i + 3y_{i+1}}{2h}.$$

Using this approximation and substituting Eq. (13) into (12) yields:

$$\left(\frac{\varepsilon}{h^2} + \frac{\mu}{2h}(\alpha p_{i+1} - 2\beta p_i - 3\alpha p_{i-1}) - \alpha q_{i-1}\right)y_{i-1}$$

$$- \left(\frac{2\varepsilon}{h^2} + \frac{2\mu}{h}(\alpha p_{i+1} - \alpha p_{i-1}) + 2\beta q_i\right)y_i \quad (14)$$

$$+ \left(\frac{\varepsilon}{h^2} + \frac{\mu}{2h}(3\alpha p_{i+1} + 2\beta p_i - \alpha p_{i-1}) - \alpha q_{i+1}\right)y_{i+1} = \alpha(f_{i+1} + f_{i-1}) + 2\beta f_i.$$

To control the disturbance perturbation parameter in the solution, we introduce the fitting parameter σ on Eq. (14). In order to get the value of σ , multiply Eq. (14) by $\frac{h}{\mu}$, denote

$\rho = \frac{\mu h}{\varepsilon}$, and then evaluate limits as $h \rightarrow 0$ gives:

$$\sigma = \frac{(\alpha + \beta)\rho p_1 \lim_{h \rightarrow 0}(y_{i-1} - y_{i+1})}{\lim_{h \rightarrow 0}(y_{i-1} - 2y_i + y_{i+1})} \quad (15)$$

From the discrete form of Eq. (7) we have

$$y_i = C_1 + C_2 e^{\frac{-\mu p_1}{\varepsilon} x_i} = C_1 + C_2 e^{-p_1 i \rho}$$

$$y_{i+1} = C_1 + C_2 e^{-p_1(i+1)\rho} = C_1 + C_2 e^{-p_1 i \rho} \cdot e^{-p_1 \rho} \quad (16)$$

$$y_{i-1} = C_1 + C_2 e^{-p_1(i-1)\rho} = C_1 + C_2 e^{-p_1 i \rho} \cdot e^{p_1 \rho}$$

Considering Eq. (16) into Eq. (15), we get:

$$\sigma = \frac{\rho p_1}{2} \coth\left(\frac{\rho p_1}{2}\right).$$

Hence, the fitted form of Eq. (14) is

$$E_i y_{i-1} - F_i y_i + G_i y_{i+1} = H_i, \quad (17)$$

where

$$E_i = \frac{\varepsilon \sigma}{h^2} + \frac{\mu}{2h}(\alpha p_{i+1} - 2\beta p_i - 3\alpha p_{i-1}) - \alpha q_{i-1},$$

$$F_i = \frac{2\varepsilon \sigma}{h^2} + \frac{2\mu}{h}(\alpha p_{i+1} - \alpha p_{i-1}) + 2\beta q_i,$$

$$G_i = \frac{\varepsilon \sigma}{h^2} + \frac{\mu}{2h}(3\alpha p_{i+1} + 2\beta p_i - \alpha p_{i-1}) - \alpha q_{i+1},$$

$$H_i = \alpha(f_{i+1} + f_{i-1}) + 2\beta f_i.$$

3 Error Analysis

Let expand the terms $y_{i\pm 1}$ and $M_{i\pm 1}$ in Eq. (12), using Taylor's series which gives the local truncation error $T_i(h)$:

$$T_i(h) = (1 - 2(\alpha + \beta))y_i'' + h^2\left(\frac{1}{12} - \alpha\right)y_i^{(4)} + h^4\left(\frac{1}{360} - \frac{\alpha}{12}\right)y_i^{(6)} + \dots \quad (18)$$

But from the values of $\alpha = \frac{1}{12}$ and $\beta = \frac{5}{12}$, Eq. (18)

leads to

$$\|T_i(h)\| \leq Ch^4 \quad (19)$$

where, $C = \frac{1}{240}|y_i^{(6)}|$.

Thus, we have

$$|y(x_i) - Y_N| \leq C(h^4) \quad (20)$$

where $y(x_i)$ and Y_N are exact and approximate solutions respectively, and C is constant independent h .

To apply the Richardson extrapolation technique, let Ω^{2N} obtained from each mesh interval Ω^N by dividing two, then denote the approximation of the solution on Ω^{2N} by Y_{2N} . Consider Eq. (20) works for any $h \neq 0$, which implies:

$$y(x_i) - Y_N \cong C(h^4) + R^N, \quad x_i \in \Omega^N \quad (21)$$

So that it also works for any $\frac{h}{2} \neq 0$ and results:

$$y(x_i) - Y_{2N} \cong C\left(\left(\frac{h}{2}\right)^4\right) + R^{2N}, \quad x_i \in \Omega^{2N} \quad (22)$$

where the terms, R^N and R^{2N} are of $O(h^6)$. Eliminating the constant C , and a combination of Eqs. (21) and (22) leads to $15y(x_i) - (16Y_{2N} - Y_N) \approx O(h^6)$, which proposes to denote:

$$(Y_N)^{ext} = \frac{1}{15}(16Y_{2N} - Y_N) \quad (23)$$

is also another approximation solution of $y(x_i)$ which obtained from the solutions of Y_N and Y_{2N} . This approximation solution with the truncation error,

$$|y(x_i) - (Y_N)^{ext}| \leq C(h^6) \quad (24)$$

Thus, the formulated quartic non-polynomial spline method in Eqs. (17) and extended to Eq. (23) with local truncation error in Eqs. (19) and (24) respectively, satisfies the consistency of the method if:

$$\lim_{h \rightarrow 0} T_i(h) = \lim_{h \rightarrow 0} Ch^4 = \lim_{h \rightarrow 0} Ch^6 = 0.$$

4 Stability of the Method

Let multiply both sides of the developed scheme in Eq. (17) by h^2 and consider the values of E_i , F_i and G_i for sufficiently small h , then we get:

$$E_i = G_i = \varepsilon \sigma, F_i = 2\varepsilon \sigma \quad (25)$$

Since, $i = 1, 2, \dots, N - 1$, considering Eq. (25), the matrix form of Eq. (17) is

$$AY = B, \quad (26)$$

where,

$$A = \begin{bmatrix} -2\varepsilon\sigma & \varepsilon\sigma & 0 & \dots & \dots & 0 \\ \varepsilon\sigma & -2\varepsilon\sigma & \varepsilon\sigma & 0 & \dots & \vdots \\ 0 & \varepsilon\sigma & -2\varepsilon\sigma & \varepsilon\sigma & \ddots & \vdots \\ \vdots & \ddots & \ddots & \ddots & \ddots & 0 \\ \vdots & \ddots & 0 & \varepsilon\sigma & -2\varepsilon\sigma & \varepsilon\sigma \\ 0 & \dots & 0 & 0 & \varepsilon\sigma & -2\varepsilon\sigma \end{bmatrix},$$

$$Y = \begin{bmatrix} y_1 \\ y_2 \\ \vdots \\ \vdots \\ y_{N-2} \\ y_{N-1} \end{bmatrix} \text{ and } B = \begin{bmatrix} h^2 H_1 - E_1 y_0 \\ h^2 H_2 \\ \vdots \\ \vdots \\ h^2 H_{N-2} \\ h^2 H_{N-1} - G_{N-1} y_N \end{bmatrix}.$$

Here, the matrix A is a tri-diagonal, irreducible, and diagonally dominant. Therefore, the system can be solved by Thomas Algorithm.

As discussed in the literature [16, 18] the eigenvalues of a tri-diagonal matrix A are given by:

$$\lambda_s = -2\varepsilon\sigma + 2\left\{\sqrt{(\varepsilon\sigma)(\varepsilon\sigma)}\right\} \cos \frac{s\pi}{N}, \quad s = 1(1)N - 1.$$

Hence, the eigenvalues of the matrix A in Eq. (26) are:

$$\lambda_s = -2\varepsilon\sigma + 2\sqrt{(\varepsilon\sigma)^2} \cos \frac{s\pi}{N} = -2\varepsilon\sigma \left(1 - \cos \frac{s\pi}{N}\right), \quad s = 1(1)N - 1.$$

But from trigonometric identity, we have

$$1 - \cos \frac{s\pi}{N} = 2 \sin^2 \frac{s\pi}{2N}. \text{ Thus, the eigenvalues of } A$$

$$\lambda_s = -2\varepsilon\sigma \left(2 \sin^2 \frac{s\pi}{2N}\right) = -4\varepsilon\sigma \sin^2 \frac{s\pi}{2N} \leq -4\varepsilon\sigma.$$

A developed method is stable if A is non-singular and

$$\|A^{-1}\| \leq C \quad \forall 0 < h < h_0.$$

where, C and h_0 are two constants that are free of h .

Since A is real and symmetric it follows that A^{-1} is also. So that, its eigenvalues are given by $\frac{1}{\lambda_s}$. The stability condition

of the method will be satisfied when

$$\|A^{-1}\| = \left|\frac{1}{\lambda_s}\right| = \left|\frac{-1}{4\varepsilon\sigma}\right| = \frac{1}{4\varepsilon\sigma} \leq C.$$

Thus, the developed quartic non-polynomial spline method is consistent and stable. Therefore, the proposed method is convergent.

5 Numerical Illustrations

In this section, we consider model examples of the singularly perturbed differential-difference equations with two parameters to validate our theoretical descriptions. Maximum absolute errors are computed by the formula:

$$Z_h = \max_i \left| y_i^h - y_i^{\frac{h}{2}} \right| \quad i = 1(1)N - 1,$$

where y_i^h is the numerical solution at the nodal point X_i

on the mesh interval of Ω^N and $y_i^{\frac{h}{2}}$ is the numerical solution at the nodal point X_i on the mesh interval of Ω^{2N} .

Example 1: Consider the singularly perturbed differential-difference problem

$$\begin{cases} \varepsilon y''(x) + \mu(1+x)y'(x-\delta) - e^{-x}y(x) = 0, & x \in (0,1) \\ y(x) = 1, & -\delta \leq x \leq 0, \quad y(1) = 1. \end{cases}$$

The exact solution is not available, so we calculate the maximum absolute errors by the double mesh principle. For computational purposes, we consider $\delta = 10^{-12}$ for both examples.

Example 2: Consider the singularly perturbed differential-difference problem

$$\begin{cases} \varepsilon y''(x) + \mu y'(x-\delta) - y(x) = -x, & x \in (0,1) \\ y(x) = 1, & -\delta \leq x \leq 0, \quad y(1) = 0. \end{cases}$$

The analytic solution of this problem is given by:

$$y(x) = \frac{(1-\mu)\left(e^{-(k_1+k_2)x/(2\varepsilon)} - e^{-(k_1+k_2)x/(2\varepsilon)}\right) + (1+\mu)\left(e^{-k_1x/(2\varepsilon)} - e^{-k_2x/(2\varepsilon)}\right)}{\left(e^{-k_1/(2\varepsilon)} - e^{-k_2/(2\varepsilon)}\right)} + (\mu+x)$$

$$\text{with } \varepsilon_1 = (\varepsilon - \mu\delta) \text{ and } k_{1,2} = \mu \pm \sqrt{\mu^2 + 4\varepsilon_1}$$

Table 1 Comparison of maximum absolute errors for Example 1, when $\varepsilon = 10^{-3}$

$\mu \downarrow$	$N \rightarrow 32$	64	128	256	512	1024
Present Method						
10^{-2}	6.5542e-05	1.6398e-05	4.0996e-06	1.0249e-06	2.5634e-07	6.4086e-08
10^{-4}	7.9774e-06	5.2550e-06	1.4139e-06	3.6245e-07	9.0642e-08	2.2661e-08
10^{-8}	1.4789e-05	4.2908e-07	7.5055e-09	8.8815e-11	7.2546e-12	2.0887e-12
10^{-10}	1.4791e-05	4.2964e-07	7.6475e-09	1.2503e-10	1.9034e-12	7.1987e-13
Results in [9]						
10^{-2}	7.074e-03	1.945e-03	5.018e-04	1.271e-04	3.184e-05	7.968e-06
10^{-4}	1.045e-02	2.830e-03	7.229e-04	1.817e-04	4.549e-05	1.137e-05
10^{-8}	1.047e-02	2.835e-03	7.242e-04	1.820e-04	4.557e-05	1.139e-05
10^{-10}	1.047e-02	2.835e-03	7.242e-04	1.820e-04	4.557e-05	1.139e-05

Table 2 Comparison of maximum absolute errors for Example 1, when $\mu = 10^{-4}$

$\varepsilon \downarrow$	$N \rightarrow 32$	64	128	256	512	1024
Present Method						
10^{-2}	6.9549e-07	1.8398e-07	4.6162e-08	1.1543e-08	2.8867e-09	7.2070e-10
10^{-4}	7.4475e-04	4.0798e-05	2.7815e-05	7.5115e-06	1.8890e-06	4.7538e-07
10^{-8}	1.3837e-03	5.9743e-05	3.9377e-05	1.0955e-05	2.8532e-06	7.1372e-07
10^{-10}	1.3837e-03	5.9743e-05	3.9377e-05	1.0955e-05	2.8532e-06	7.1372e-07
Results in [9]						
10^{-2}	1.252e-03	3.162e-04	7.946e-05	1.987e-05	4.970e-06	1.242e-06
10^{-4}	2.470e-02	1.301e-02	4.656e-03	1.624e-03	4.396e-04	1.102e-04
10^{-8}	2.123e-02	8.699e-03	3.120e-03	1.052e-03	3.347e-04	1.038e-04
10^{-10}	2.121e-02	7.835e-03	2.704e-03	8.976e-04	2.797e-04	8.430e-04

Table 3 Maximum absolute errors before and after applying the Richardson extrapolation for Example 1, when $\varepsilon < \mu = 10^{-3}$

$\varepsilon \downarrow$	$N \rightarrow 32$	64	128	256	512	1024
After						
10^{-4}	1.8079e-04	5.4565e-05	1.3834e-05	3.5207e-06	8.8021e-07	2.2005e-07
10^{-6}	1.8079e-04	5.4565e-05	1.3834e-05	3.5207e-06	8.8021e-07	2.2005e-07
10^{-8}	1.8079e-04	5.4565e-05	1.3834e-05	3.5207e-06	8.8021e-07	2.2005e-07
10^{-10}	1.8080e-04	5.4567e-05	1.3834e-05	3.5208e-06	8.8024e-07	2.2006e-07
Before						
10^{-4}	3.2137e-03	1.3165e-04	4.9202e-05	1.6322e-05	4.3208e-06	1.0952e-06
10^{-6}	3.2137e-03	1.3165e-04	4.9202e-05	1.6322e-05	4.3208e-06	1.0952e-06
10^{-8}	3.2137e-03	1.3165e-04	4.9202e-05	1.6322e-05	4.3208e-06	1.0952e-06
10^{-10}	3.2138e-03	1.3165e-04	4.9203e-05	1.6322e-05	4.3209e-06	1.0953e-06

Table 4 Maximum absolute errors with fitting (W. F) and without fitting (W.O. F) parameter for Example 1, when $\varepsilon < \mu = 10^{-3}$

$\varepsilon \downarrow$	$N \rightarrow 32$	64	128	256	512	1024
W. F						
10^{-4}	1.8079e-04	5.4565e-05	1.3834e-05	3.5207e-06	8.8021e-07	2.2005e-07
10^{-6}	1.8079e-04	5.4565e-05	1.3834e-05	3.5207e-06	8.8021e-07	2.2005e-07
10^{-8}	1.8079e-04	5.4565e-05	1.3834e-05	3.5207e-06	8.8021e-07	2.2005e-07
10^{-10}	1.8080e-04	5.4567e-05	1.3834e-05	3.5208e-06	8.8024e-07	2.2006e-07
W.O. F						
10^{-4}	1.3710e-03	8.5454e-04	3.9479e-04	1.0020e-04	2.5467e-05	6.3837e-06
10^{-6}	2.6758e-02	3.3937e-02	3.5052e-02	1.2619e-02	5.9584e-03	4.4740e-03
10^{-8}	2.8268e-02	4.0314e-02	6.1232e-02	8.5222e-02	1.3035e-01	2.5806e-01
10^{-10}	2.8283e-02	4.0349e-02	6.0781e-02	7.6575e-02	7.4437e-02	8.2861e-02

Table 5 Comparison of maximum absolute errors for Example 2, when $\varepsilon = 10^{-3}$

$\mu \downarrow$	$N \rightarrow 32$	64	128	256	512	1024
Present Method						
10^{-2}	9.2960e-04	2.3290e-04	5.8941e-05	1.4738e-05	3.6893e-06	3.6893e-06
10^{-5}	2.0555e-06	2.5750e-07	5.9506e-08	1.4797e-08	3.6979e-09	9.2472e-10
10^{-7}	1.1198e-06	2.3221e-08	9.3234e-10	1.5330e-10	3.7066e-11	9.4675e-12
10^{-10}	1.1103e-06	2.0857e-08	3.4127e-10	5.5301e-12	1.4166e-13	3.9091e-13
Results in [9]						
10^{-2}	1.470e-02	3.909e-03	1.005e-03	2.525e-04	6.327e-05	1.582e-05
10^{-5}	1.071e-02	3.666e-03	9.318e-04	2.339e-04	5.854e-05	1.464e-05
10^{-7}	1.066e-02	3.660e-03	9.303e-04	2.335e-04	5.844e-05	1.461e-05
10^{-10}	1.066e-02	3.660e-03	9.303e-04	2.335e-04	5.844e-05	1.461e-05

Table 6 Comparison of maximum absolute errors for Example 2, when $\varepsilon = 10^{-3}$.

$\mu \downarrow$	$N \rightarrow 32$	64	128	256	512	1024
After						
10^{-4}	1.0592e-05	2.3946e-06	5.9382e-07	1.4838e-07	3.7093e-08	9.2732e-09
10^{-6}	1.2048e-06	4.4520e-08	6.2575e-09	1.4846e-09	3.6988e-10	9.2715e-11
10^{-8}	1.1113e-06	2.1091e-08	3.9984e-10	2.0174e-11	3.7818e-12	1.1909e-12
10^{-10}	1.1103e-06	2.0857e-08	3.4127e-10	5.5301e-12	1.4166e-13	3.9091e-13
Before						
10^{-4}	7.5786e-04	5.7296e-05	5.8259e-06	9.2083e-07	1.9666e-07	4.7066e-08
10^{-6}	7.0795e-04	4.5377e-05	2.8778e-06	1.8573e-07	1.3000e-08	1.1592e-09
10^{-8}	7.0746e-04	4.5258e-05	2.8484e-06	1.7840e-07	1.1169e-08	7.0160e-10
10^{-10}	7.0745e-04	4.5257e-05	2.8481e-06	1.7833e-07	1.1151e-08	6.9702e-10

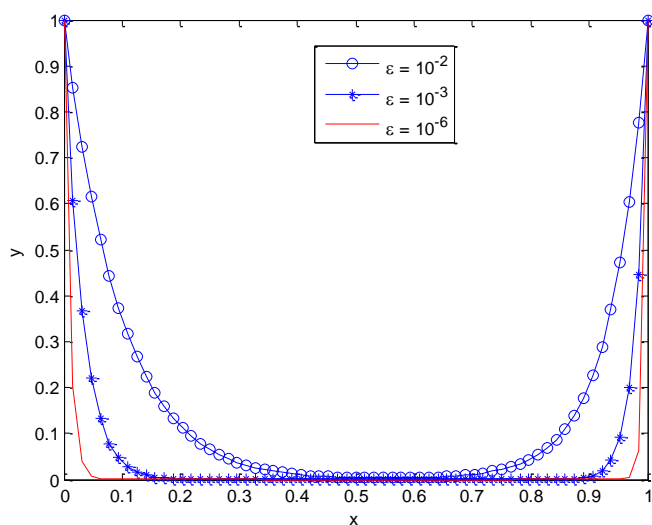


Fig. 1 Solution profiles for Example 1, when $\mu = 10^{-4}$, $\delta = 10^{-12}$ and $N = 64$.

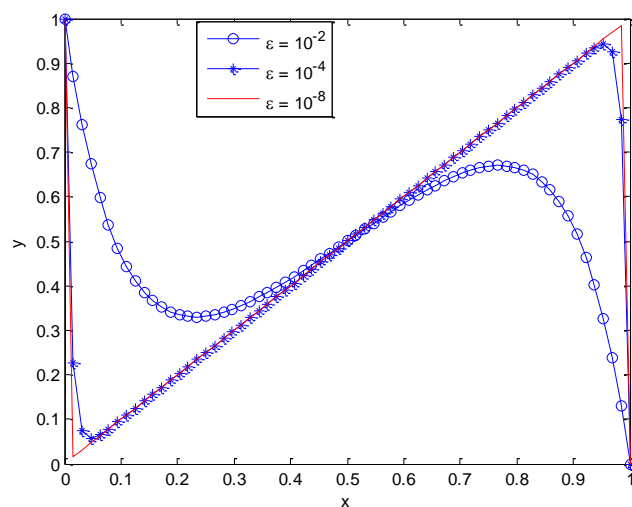


Fig. 3 Solution profiles for Example 2, when $\mu = 10^{-4}$, $\delta = 10^{-12}$ and $N = 64$.

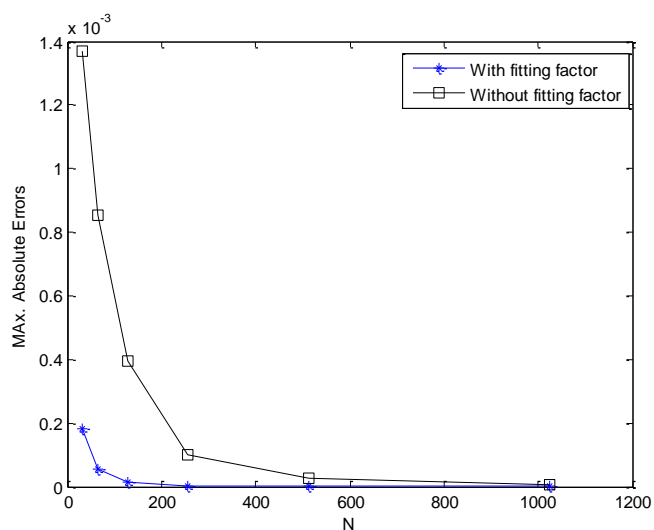


Fig. 2 Obtained maximum absolute errors when $\varepsilon = 10^{-4}$ and $\mu = 10^{-3}$

6 Discussion and Conclusion

In this paper, we presented a quartic non-polynomial spline method to solve the singularly perturbed differential-difference equation involving two parameters. First, this equation is transformed into an asymptotically equivalent differential equation, and then applying a quartic non-polynomial spline method. Convergence of the method has been established. To validate the method, numerical illustrations have been given in Table 1-6 and Fig. 1-3.

These results show, the present method gives a more accurate solution than some existing methods in the literature. Also, maximum absolute errors decrease as the number of mesh points N increases which implies convergence of the method. Moreover, we attempted to increase the order of convergence by Richardson's extrapolation and discovered that this well-known convergence acceleration technique has some limitations. We observe that even though this extrapolation technique improves the accuracy slightly, it does not increase the rate of convergence.

Generally, a quartic non-polynomial spline method is convergent and gives an accurate numerical solution for solving singularly perturbed differential-difference problems involving two parameters.

References

- [1] File, G. and Reddy, Y.N., 2013. Computational method for solving singularly perturbed delay differential equations with negative shift. *International Journal of Applied Science and Engineering*, 11(1), pp.101-113.
- [2] File, G., Gadisa, G., Aga, T. and Reddy, Y.N., 2017. Numerical solution of singularly perturbed delay reaction-diffusion equations with layer or oscillatory behaviour. *American Journal of Numerical Analysis*, 5(1), pp.1-10.
- [3] Gadisa, G., File, G. and Aga, T., 2018. Fourth order numerical method for singularly perturbed delay differential equations. *International Journal of Applied Science and Engineering*, 15(1), pp.17-32.
- [4] Kadalbajoo, M.K. and Kumar, V., 2007. B-spline method for a class of singular two-point boundary value problems using optimal grid. *Applied Mathematics and Computation*, 188(2), pp.1856-1869.
- [5] Kadalbajoo, M.K. and Sharma, K.K., 2004. Numerical analysis of singularly perturbed delay differential equations with layer behavior. *Applied Mathematics and Computation*, 157(1), pp.11-28.
- [6] Kadalbajoo, M.K. and Sharma, K.K., 2008. A numerical method based on finite difference for boundary value problems for singularly perturbed delay differential equations. *Applied Mathematics and Computation*, 197(2), pp.692-707.
- [7] Kadalbajoo, M.K. and Yadaw, A.S., 2008. B-Spline collocation method for a two-parameter singularly perturbed convection–diffusion boundary value problems. *Applied Mathematics and Computation*, 201(1-2), pp.504-513.
- [8] Kadalbajoo, M.K., Gupta, V. and Awasthi, A., 2008. A uniformly convergent B-spline collocation method on a nonuniform mesh for singularly perturbed one-dimensional time-dependent linear convection–diffusion problem. *Journal of Computational and Applied Mathematics*, 220(1-2), pp.271-289.
- [9] Sahu, S.R. and Mohapatra, J., 2019. Parameter uniform numerical methods for singularly perturbed delay differential equation involving two small parameters. *International Journal of Applied and Computational Mathematics*, 5(5), pp.1-19.
- [10] Akram, G. and Talib, I., 2014. Quartic non-polynomial spline solution of a third order singularly perturbed boundary value problem. *Research Journal of Applied Sciences, Engineering and Technology*, 7(23), pp.4859-4863.
- [11] Ala'yed, O.H., Ying, T.Y. and Saaban, A., 2015. New fourth order quartic spline method for solving second order boundary value problems. *MATEMATIKA: Malaysian Journal of Industrial and Applied Mathematics*, 31(2), pp.149-157.
- [12] Chakravarthy, P.P., Kumar, S.D., Rao, R.N. and Ghate, D.P., 2015. A fitted numerical scheme for second order singularly perturbed delay differential equations via cubic spline in compression. *Advances in Difference Equations*, 2015(1), pp.1-14.
- [13] Chakravarthy, P.P., Kumar, S.D. and Rao, R.N., 2017. An exponentially fitted finite difference scheme for a class of singularly perturbed delay differential equations with large delays. *Ain Shams Engineering Journal*, 8(4), pp.663-671.
- [14] Dugassa, T., File, G. and Aga, T., 2019. Stable Numerical Method for Singularly Perturbed Boundary Value Problems with Two Small Parameters. *Ethiopian Journal of Education and Sciences*, 14(2), pp.9-27.
- [15] Erdogan, F., 2009. An exponentially fitted method for singularly perturbed delay differential equations. *Advances in Difference Equations*, 2009, pp.1-9.
- [16] Siraj, M.K., Duressa, G.F. and Bullo, T.A., 2019. Fourth-order stable central difference with Richardson extrapolation method for second-order self-adjoint singularly perturbed boundary value problems. *Journal of the Egyptian Mathematical Society*, 27(1), pp.1-14.
- [17] Zahra, W.K. and El Mhlawy, A.M., 2013. Numerical solution of two-parameter singularly perturbed boundary value problems via exponential spline. *Journal of King Saud University-Science*, 25(3), pp.201-208.
- [18] Smith, G.D., Smith, G.D. and Smith, G.D.S., 1985. Numerical solution of partial differential equations: finite difference methods. *Oxford University Press*.

Morphogenesis of Silicovanadate Glasses: Investigation of Physical Properties

Md. Moinul Islam¹, Md. Abdur Rashid¹, Md. Parvez Ahamed¹, Md. Emran Hossain², M. Rafiqul Ahsan¹, M. Golam Mortuza¹, Mirza Humaun Kabir Rubel^{3,*}

¹Department of Physics, University of Rajshahi, Rajshahi-6205, Bangladesh

²Physics Discipline, University of Khulna, Khulna-9208, Bangladesh

³Department of Materials Science and Engineering, University of Rajshahi, Rajshahi-6205, Bangladesh

Received: March 13, 2021, Revised: April 29, 2021, Accepted: April 29, 2021, Available Online: May 21, 2021

ABSTRACT

In this article, we demonstrate the synthesis and various characterizations of silicovanadate glasses of $x\text{SiO}_2(100-x)\text{V}_2\text{O}_5$ for $x = (10-50)$ mol%, glasses which are prepared by the melt quenching method. FTIR spectra analysis confirms dominant chemical bonds among silicon, vanadium, and oxygen elements as expected. The assigned chemical bonds are Si-O-Si, O-Si-O, V-O-V, V=O, Si-O-V, O-H from FTIR spectra. The IR spectra of all glass specimens were baseline corrected and deconvoluted to distinct peaks of chemical bonds in overlapped Gaussians with employing computer program. The chemical bond's position shifted and affected due to the addition of vanadium pentoxide by the heat treatment process. The X-ray diffractions (XRD) patterns of glass samples exhibit partial crystalline nature for 10S90V and 50S50V that is influenced by high-temperature application. The differential thermal analysis (DTA) of base and heat-treated specimen determines the glass transition (T_g), crystallization, and liquidus temperature with prominent exothermic and endothermic reactions. It is seen that the pH of the glass specimens abruptly changes due to the surface effect of V_2O_5 while bulk effects become robust after about 30 minutes. The measured hardness of three glass samples shows high H_V -values and a slight linear increment is observed for higher V_2O_5 contents. The current-voltage (I-V) characteristic connected to the electrical conductivity of the glass specimen (20S80V) shows a relatively higher and non-linear trend of conductivity which reveals the behavior of a semiconductor. Moreover, temperature-dependent electrical resistivity measurement of the same sample (20S80V) manifests the semiconducting nature up to 427 °C as well.

Keywords: Si/V-based glass, FTIR, X-ray diffraction, DTA, pH, Current-Voltage characteristics, Electrical resistivity.



This work is licensed under a Creative Commons Attribution-Non Commercial 4.0 International License.

1 Introduction

Glass-ceramics are polycrystalline or amorphous substances possessing the properties of hardness, rigidity, brittleness which are prepared by controlled crystallization processes. Glass ceramics have widespread attentive technological applications in various fields such as electronic devices, optical devices, reflecting windows, ray absorbers, mechanical sensors, electro-optic devices, sealants, etc. [1]-[4]. Among various oxides glasses, the silicovanadate glasses have great scientific vast technological, and attractive industrial interest for their individual characteristics. To know the structural information, electrical conductivity, hardness, solubility, and optical properties of this silicovanadate glasses various characterization techniques such as X-ray diffraction, Fourier Transform IR study, Four probe method, Vickers hardness testing system, pH meter [5]-[8], etc., have been utilized where vanadium metal manifests various physical and chemical properties. However, some oxide glasses are generally insulating type in the aspect of conductivity but the addition of some transition metal such as VO, V_2O_5 , Fe_2O_3 , WO_3 , ZnO, etc. make these glasses semiconducting.

These binary oxide glasses are studied widely for their attractive potential applications in various fields such as optical and electrical memory switching, solid state devices, and optical fibers [9]. For making useful memory and switching devices in various fields V_2O_5 containing glasses are extensively used for its transition behavior. In order to get silicovanadate glasses,

V_2O_5 is used among various transition metals because of having electrical conductivity due to the electron hopping behavior between V^{5+} and V^{4+} ions [10]-[13]. In this $x\text{SiO}_2(100-x)\text{V}_2\text{O}_5$ binary system glasses, Si^{4+} ions act as network forming ions whereas vanadium ions might act diverse role either as network formers, modifiers, and/or intermediate in the amorphous glass network [14]. The most important property of the glassy materials is the viscosity which makes the glass in liquid nature and is also closely connected with the nature and structure of the melts [15]-[16]. Besides, the addition of the network modifier component in the composition increases the density as the network modifier ions attempt to occupy the interstices within the network. Noteworthy, the hardness of glasses makes strength and density of packing of the atoms in the localized structure [17]. During the course of this investigation, the microhardness (GPa) of silicate-based glasses has been studied to investigate mechanical performance on the basis of well-established factors [18]-[22]. The electrical conductivity of a glass system usually changes due to the presence of network modifiers [14]. V_2O_5 exhibits semi-conductivity for the presence of V^{5+} and V^{4+} oxidation states that originate electron hopping between these two ions [23]-[24]. Recently, the electrical properties of several new V/Fe-based glasses have been analyzed to relate the structure and electrical conductivity (σ) for their important applications [25]-[30]. Moreover, the chemical durability and possible improvement of the aforementioned glasses with electrical conductivity have also been analyzed [25]. Following this, the solubility of our prepared glasses in air condition has

*Corresponding Author Email Address: mhk_mse@ru.ac.bd

been measured by means of pH meter to explore physico-chemical changes in the specimens. Therefore, in this article, we have prepared and established a relationship between local structure and physical properties such as electrical conductivity, hardness, thermal behavior, and solubility of several silicovanadate glasses by FTIR, XRD, four-probe method, DTA, TCR, and pH meter for the first time.

2 Materials and Methods

For the synthesis of silicovanadate glasses by the conventional melt quenching method, commercially available reagents SiO_2 and V_2O_5 were chosen as starting compositions. The chemicals Vanadium oxide (V_2O_5) and Silica (SiO_2) were collected from Merck Specialties Pvt. Ltd. Worli, Mumbai-400018. These chemicals were used directly without any further purification. For the preparation of 20 gm batch of $x\text{SiO}_2(100-x)\text{V}_2\text{O}_5$ glass system the collected raw materials were homogeneously mixed both in an agate mortar and ball-milled machine for 6-8 hours. The mixture was then poured into a porcelain crucible and melted in an electric carbolite furnace at $\sim 1500^\circ\text{C}$ for 1 hour. Dull brown transparent glass specimens were observed after sudden quenching using steel block and hammer assembly. Afterward, the base glass samples were placed in an Aluminum crucible and heated at $500^\circ\text{C}/1\text{h}$ to study the differences in physical properties post heat treatment.

FTIR spectra of the silicate vanadate glasses were collected on a Spectrum 100, Perkin Elmer spectrophotometer by KBr disk method within the wavenumber of 400 and 4000 cm^{-1} to know all possible chemical bonds. X-ray diffraction patterns of base and heat-treated glasses were examined using the monochromatic CuK_α radiation by setting 2θ in the range of 5° to 50° at a scanning rate of 0.02° with Philips "X-pert Pro XRD system". Crystal phases were detected based on standards compiled by the International Center for Diffraction Data (ICDD). The important phase transformations and crystallization temperatures were investigated by a STA-8000 DTA model (Parkin Elmer) meter as well. Differential thermal analysis (DTA) was carried out from room temperature (RT) to 900°C by varying the heating rate from 5 to $10^\circ\text{C min}^{-1}$. During the measurement, about ten milligrams of $\alpha\text{-Al}_2\text{O}_3$ powder and finely pulverized glass were utilized as a reference sample. To investigate physical and chemical changes the solubility of the glass specimens is measured with the aid of a pH/mv meter (Model-PHS-25, China). In this experiment, the scale of the meter was calibrated using Potassium hydrogen phthalate (pH = 4.0) and the Sodium tetraborate (pH = 9.18) to read pH directly. Temperature-dependent electrical conductivity (σ) and resistivity (ρ) were carried out by employing dc four-probe method for 20S80V glass specimen only. The glass specimen was cut into a rectangular shape and each longitudinal edge was connected by the probe(s) using Ag solder. The electrical current (I) was recorded through alternating voltage between 1.0 and 15 V, on the other hand, the voltage (V) was registered by changing electrical current between 1.0 and 2.0 mA along both length and width direction. Moreover, the electrical conductivity (σ) of glass sample was evaluated on the basis of the following equation: $\sigma = R^{-1} \cdot S^{-1} \cdot l$; where R, S, and l are electrical resistivity (Ω) estimated from a slope of the straight line of V vs. I, surface area (cm^2) and electrode distance (cm), respectively.

The microhardness of the prepared glasses was ascertained by Vickers indentation (Matsuzawa microhardness tester (MXT- α 1) equipped with a pyramidal diamond indenter under (100 g

load, 20 s) by neglecting the size effects of indentation [17],[26]-[27]. The H_V -values (GPa) of glass samples were calculated from the expression as given, $H_V = 1854F/d^2$, here $F = 9.81\text{ N}$, and d is the average indentation diagonal in μm , as reported elsewhere [26]. The values are recorded on averages over 8–10 independent measurements. The indentations were examined and evaluated via the attached high-resolution microscope.

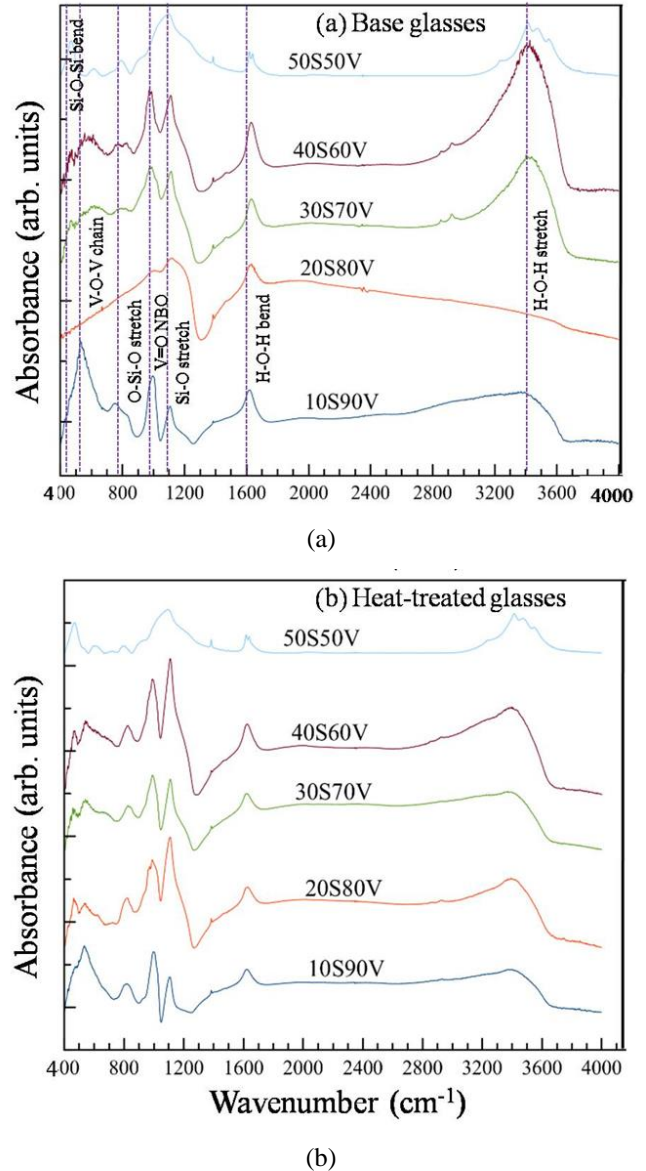


Fig. 1 Infrared spectra of (a) base glass and (b) heat-treated glass samples.

3 Results and Discussion

3.1 FTIR Analysis of Silicovanadate Glasses

Fourier Transform Infrared (FTIR) absorption spectra of glasses usually provide significant and valuable information on the arrangement of atoms, the chemical bonding between them, and the changes in atomic configurations caused by the increase or decrease of concentration of glass-forming systems. FTIR absorbance spectra of different silicate vanadate glasses are recorded from 400 cm^{-1} to 4000 cm^{-1} at room temperature. Fig. 1 (a) and 1(b) show FTIR spectra of $x\text{SiO}_2(100-x)\text{V}_2\text{O}_5$ of base glass and heat-treated glass samples respectively, with assigned prominent bonds and added vanadium pentoxide contents. The

interpretation of the IR-spectra is based on the literature data of a series of crystalline and amorphous vanadate phases [29]-[34]. The Structural groups are assigned respectively, Si-O-Si bonds for bending vibration in 458-466 cm^{-1} [35]-[37], V-O-V bonds for chain vibration in 512-552 cm^{-1} [38]-[41].

V-O-V bonds for bending vibration in 593-624 cm^{-1} [42], O-Si-O bonds for symmetric stretching vibration in 798 cm^{-1} [43], V-O-V bonds for asymmetric stretching vibration in 822-826 cm^{-1} [44], Si-O-V bonds for vibration in 911 cm^{-1} [45], V=O bonds for non-bridging in 980-998 cm^{-1} [46], Si-O-Si bonds for asymmetric stretching vibration in 1073 cm^{-1} [47], Si-O bonds for asymmetric stretching vibration in 1104-1227 cm^{-1} [48]-[50]. Whereas, O-H bonds for vibration in 1385-1523 cm^{-1} [51], H-O-H bonds for bending vibration in 1601-2028 cm^{-1} [52]-[56], H-O-H bonds for symmetric stretching vibration in 3403-3447 cm^{-1} [57]-[58] for hygroscopic nature. However, we did not observe any significant change in the FTIR spectra of our synthesized glass samples even after heat treatment. The structural groups and main bonds of heat-treated samples remain in almost harmonious peak positions like base glasses, except a slight change in their intensity. This means that the local structure of the synthesized glass specimens did not alter after heat treatment up to 500 °C. Table 1 displays several physical properties

including melting temperature during synthesis of all glasses. However, the melting temperature of 50S50V sample was undetermined or known due to a large amount of silica (melting temperature ~1700 °C) present.

Table 1 Melting temperature and optical quality of the glasses of various compositions.

Samples	Nominal composition (mol %)		Melting Temperature (°C)	Optical quality	X-ray diffraction
	Si ₂ O	V ₂ O ₅			
10S90V	10	90	1200	Transparent	Partially Crystallized
20S80V	20	80	1250	Transparent	Amorphous
30S70V	30	70	1300	Transparent	Amorphous
40S60V	40	60	1300	Transparent	Amorphous
50S50V	50	50	Unknown	Opaque	Amorphous

Table 2 Deconvoluted band positions of xSiO₂(100-x)V₂O₅ base and (heat-treated) glasses.

Chemical Bonds	Band position (cm^{-1})				
	10S90V	20S80V	30S70V	40S60V	50S50V
Si-O-Si (Bending)	466 (480)	- (463)	458 (458)	464 (462)	466 (467)
V-O-V (Chain)	528 (543)	- (532)	512 (536)	552 (539)	- (-)
V-O-V (Bending vibration)	593 (601)	- (591)	602 (632)	624 (602)	616 (610)
V-O (stretching Vibration)	763 (-)	736 (-)	- (-)	784 (-)	749 (728)
O-Si-O (symmetric Stretching Vibration)	- (-)	- (-)	- (-)	- (-)	798 (799)
V-O-V (Asymmetric Vibration)	826 (820)	- (815)	822 (830)	- (824)	- (-)
Si-O-V (Vibration)	- (-)	- (-)	- (-)	- (-)	911 (921)
V=O (Non bridging)	991 (987,1011)	998 (972,1007)	991 (953,997)	980 (948,992)	- (1002)
Si-O-Si (Asymmetric Stretching Vibration)	- (-)	- (-)	- (-)	- (-)	1073 (1088)
Si-O (Asymmetric Stretching Vibration)	1105,1168 (1103,1157)	1137,1212 (1100,1127, 1196)	1112,1174 (1107,1172)	1104,1192 (1105,1182)	1227 (1212,1261)
O-H (vibration)	1390,1523 (1400,1572)	1470 (1380,1503)	1441 (1405,1535)	1385,1512 (1415,1519)	- (-)
H-O-H (Bending vibration)	1619 (1630)	1616,1752, 2028 (1629)	1601,1633 (1628)	1632 (1627)	1635 (1618,1637)

In order to obtain the quantitative information, the spectra of the base and heat-treated glasses are deconvoluted to several Gaussians according to the presence of peaks and shoulders in the spectral shape. The high-frequency band peaks have a relatively higher intensity than low-frequency band peaks and consist of broad Gaussian. The shape of the absorption spectrum changes with increasing V₂O₅ content up to 90 mol%.

The structural bonds of base samples slightly shift in contrast to heat-treated samples. The FTIR spectra are divided into two regions, one in the lower wavenumber from 400 cm^{-1} to 1700 cm^{-1} and the other in the higher frequency range 1700 cm^{-1} -4000 cm^{-1} . As it is difficult to identify the exact position of the absorption band thus deconvolution of these bands was carried out to obtain the exact position of the absorption band [28]. The

deconvolution of 10S90V, 20S80V, 30S70V, 40S60V, and 15S50V base and heat-treated glasses with baseline correction are shown in Fig. A1.

The spectra exhibited different absorption bands due to various structural units of SiO_2 and V_2O_5 . Further, the deconvolution method also can calculate the relative area of each component band and band positions of base and heat-treated glasses (Fig. A2). The concentration of the structural group is proportional to the relative area of its component bands. The summary of the data on various absorption bands observed in the deconvolution IR spectra of $x\text{SiO}_2(100-x)\text{V}_2\text{O}_5$ of base and heat-treated glasses are presented in the values within (heat-treated) are indicated for heat-treated glasses.

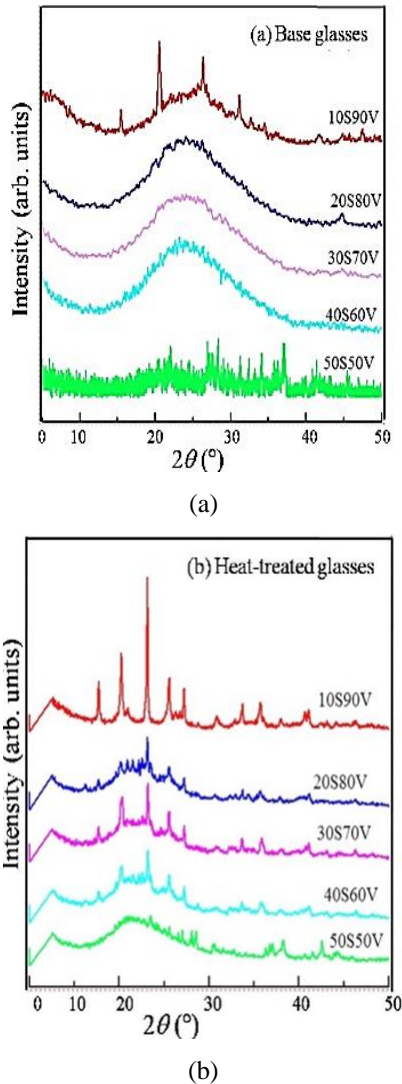


Fig. 2 The X-ray diffraction patterns of (a) base and (b) heat-treated glass samples.

3.2 XRD analysis of silicovanadate glasses

To know the crystalline nature of the prepared base and heat-treated glass samples X-ray diffraction patterns were collected and analyzed, which are shown in Fig. 2. The XRD patterns of base glass samples are shown in Fig. 2(a). All the base glass samples display weak diffuse diffraction patterns with amorphous halos except 10S90V composition. The sample 10S90V is partially crystallized because some peaks are observed at about 15° , 20° , 28° , 32° due to the formation of

several phases of silicovanadate compounds. However, few weak diffuse halos are observed in the 20S80V, 30S70V, 40S60V, and 50S50V base glasses that imply the homogeneous nature of prepared glasses. Moreover, the XRD patterns of heat-treated glass samples are cumulated and shown in Fig. 2(b).

X-ray diffraction study of heat-treated glass samples shows the formation of possible primary crystalline phases of SiV_2O_7 , $\text{Si}_2\text{V}_2\text{O}_6$, and $\text{Si}_2\text{V}_2\text{O}_9$ indicating the multiple combinations of elements [45]. The exact peak positions corresponding to phases of heat-treated glasses were not determined for the limited feature of the XRD machine. From X-ray diffraction patterns it is seen, the crystalline peak increases with increasing V_2O_5 contents in the case of heat-treated glass samples. Therefore, phase formation in our synthesized base glasses depends both on heat treatment and composition ratios of raw materials used.

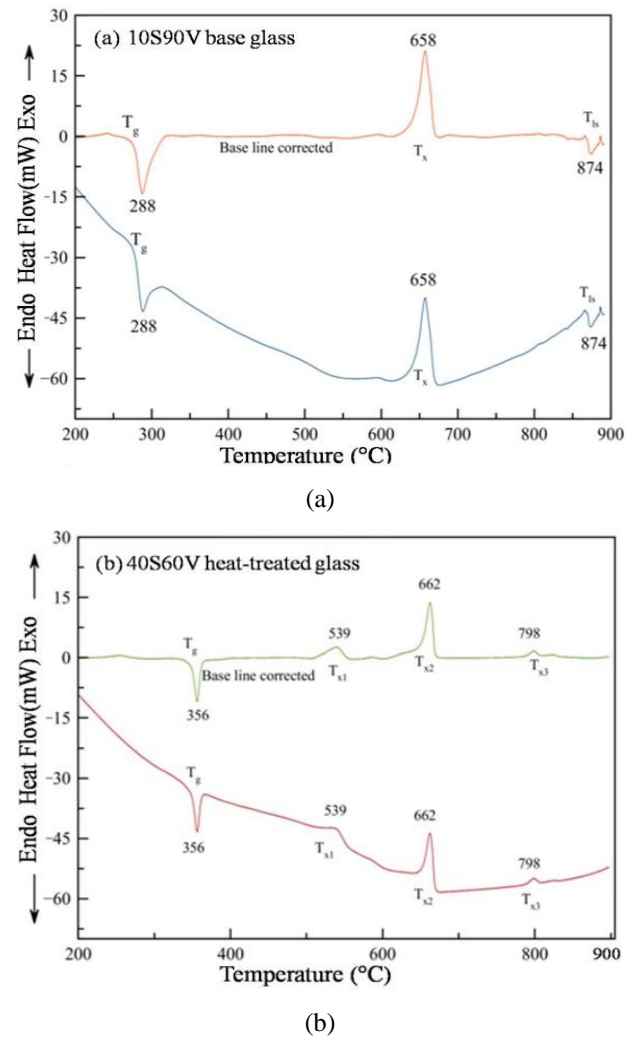


Fig. 3 DTA curves of (a) 10S90V base glass specimen and (b) 40S60V heat-treated sample.

3.3 DTA Analysis of Silicovanadate Glasses

Fig. 3 reveals the Differential Thermal Analysis (DTA) curves of 10S90V base and 40S60V heat-treated glass. The DTA traces for two glass samples are recorded in the temperature range of 30 to 900 °C, but the curves are presented from 200 to 900 °C. For 10S90V base glass, the glass transition temperature, T_g (288°C), crystallization temperature, T_x (658°C), and liquidus temperature T_l (874°C) are recorded. The endothermic

characteristics of the specimen are used to determine the T_g and T_{is} while exothermic characteristics give T_x . For this composition 10S90V, the curve represents a broad exothermic peak at 658 °C indicates T_x , and the endothermic peak at 874 °C is a measure of the liquidus temperature (T_{is}). Whereas, the base glass 40S60V was heat-treated at 500 °C to collect DTA data as well. In this heat-treated glass sample, the glass transition temperature is raised to 356 °C (for endothermic reaction) with three exothermic peaks that can be visually resolved in one large and two small peaks due to the crystallization. In the sample the first peak at 539 °C, the second peak at 662 °C and the third peak at 798 °C originate due to the crystallization of various phases.

Moreover, several exothermic peaks were observed owing to the formation of various possible silicovanadate compounds such SiV_2O_7 , $Si_2V_2O_6$, and $Si_2V_2O_9$ at 539 °C, 662 °C, and 798 °C respectively, as expected from X-ray diffraction data. However, the liquidus temperature (T_{is}) could not be determined because of the poor endothermic response of the specimen. All DTA traces exhibit typical glass transitions with the inflection point between 250 to 380 °C.

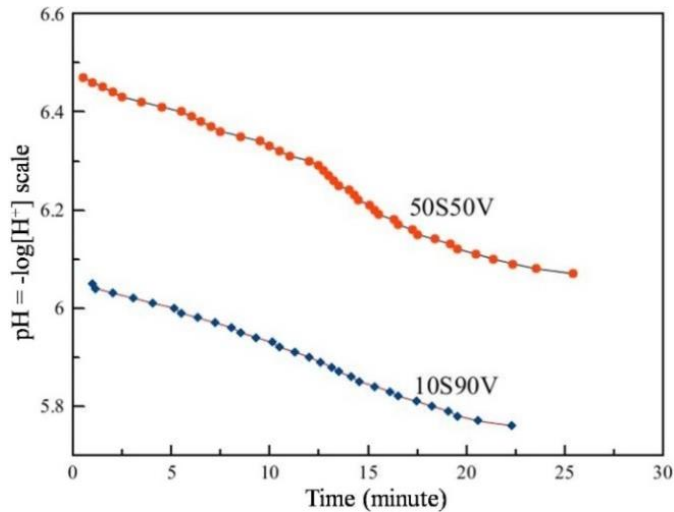


Fig. 4 Variation of pH of glass powder solution with time

3.4 pH Analysis of Silicovanadate Glasses

The pH measurement of glass samples is related to chemical durability which is defined as the stability of specimens under chemical attack. Lack of chemical durability that changes pH is mainly occurred owing to the dissolution of constituent elements in the chemical environment. It is known that higher chemical durability lowers the leaching rate of elements. A high leaching rate (lower chemical durability) is observed for high content of vanadate in contrast to more silica content glasses. The pH of the glass powder solution of 10S90V and 50S50V compositions in distilled H_2O are measured for 30 minutes, shown in Fig. 4. The recorded pH of the distilled water before the experimentation was 7.02. Initially, the solution of 50S50V glass powder shows the value of pH near 6.50 as seen from the curve. It is confirmed that the solution of this glass sample is acidic because the value of pH is less than 7 as there is no alkali or alkaline elements in our synthesized products. After stirring the solution by the magnetic stirrer, the value of pH gradually decreases owing to the leaching of silica and vanadate compositions in exponential form but after approximately 30 minutes the value of pH hardly changed. On the other hand, the solution of 10S90V powder sample exhibits pH ~6.10 at the beginning which shows a more acidic nature than 50S50V glass. This means that the glass

composition 10S90V exhibits lower chemical durability than that of 50S90V composition. Therefore, due to the formation of acid in distilled water the pH of the glass solution decreases as the hydrogen ion concentration increases. However, initially, the abrupt change of pH of the specimen is observed for the surface effect of V_2O_5 but strong bulk consequence becomes prominent with time. If we carry out pH measurement for all compositions from 10S90V to 50S50V it is expected that chemical inertness (less leaching rate) will increase sequentially.

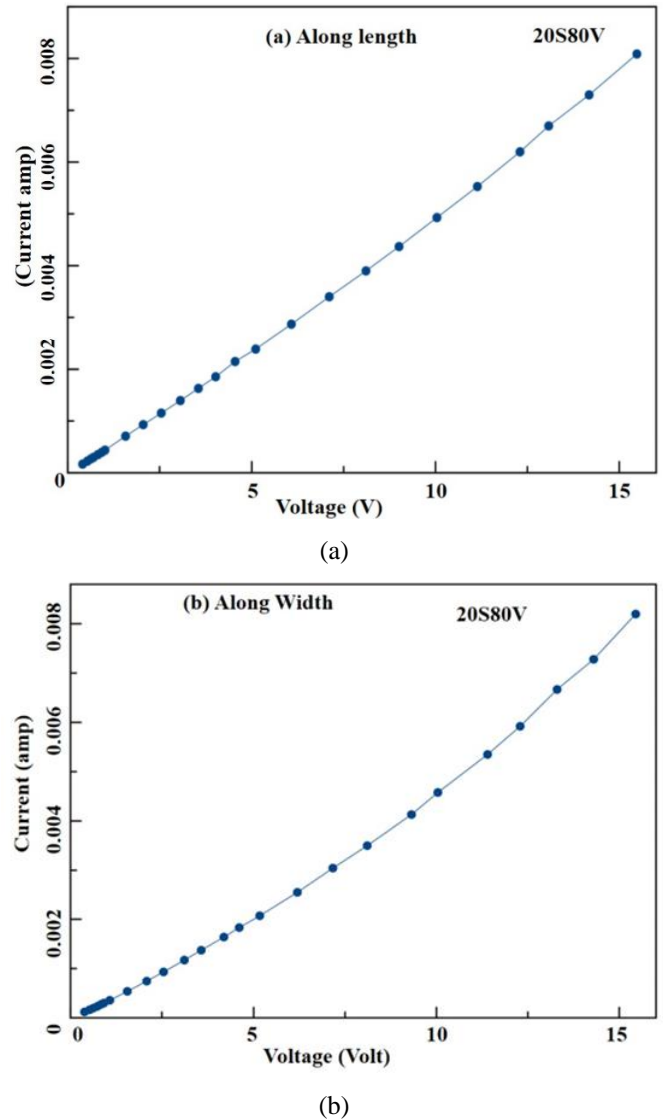


Fig. 5 $I \sim V$ Characteristic curve of the 20S80V base glass specimen along (a) length (b) width.

3.5 Vickers Hardness Analysis of Silicovanadate Glasses

Vicker hardness (H_v) data for 10S90V, 30S70V, and 40S60V base glass samples are listed in Table 3. The microhardness value of glass samples are almost comparable but vary slightly with the variation of compositions. The maximum hardness (~5.42 GPa) is observed for the glass sample 10S90V is slightly higher than two other samples (30S90V and 40S60V). However, the microhardness of glass-ceramics is mainly governed by the various cation–oxygen bond-strengths, and the glass network connectivity, and the cross-linking degree of its various segments [20]-[21],[57],[58]. The V-O-V and V=O bonds are weaker compared to Si-O-Si and O-Si-O that prevented the sequential intra-network links in the glassy

structure [46]-[48]. But the bonds of V and its local structure usually join distinct network segments, which might solidify and stiff the structure for the enhancement of H_v [59].

Table 3 Vickers hardness for 10S90V, 30S70V, and 40S60V base glass samples.

Samples	Diagonal distance (μm)		H_v (GPa)
	d_1	d_2	
10S90V	59.25(3)	56.63(6)	5.42(4)
30S70V	59.63(6)	59.69(7)	5.11(1)
40S60V	62.82(8)	57.69(7)	5.00

3.6 Electrical Conductivity (σ) of Silicovanadate Glasses

Current (Amp) versus voltage (V) characteristic curves for 20S80V specimen along the length and the width of the specimen are presented in Fig. 5(a) and 5(b) respectively. The I - V characteristic curves related to electrical conductivity (σ) increased gradually but not linearly with applied voltage. The deviated patterns of glass specimen from straight-line follow the relation, $I = KV^n$ where n is greater than one, which is a behavior of semiconductor. Moreover, the observed value of σ in this glass material is in the range of semi-conductivity. Moreover, Fig. 6 reveals the measured conductivity in Siemens per meter (S m^{-1}) reaches its highest value at about 440 °C. At this temperature all the impurity atoms are ionized and the number of electrons becomes maximum to get the utmost conductivity. On the other hand, the conductivity shows a sharp decreasing trend from 442 to 582 °C due to the decrease in drift mobility of electrons with the rise of temperature in this range.

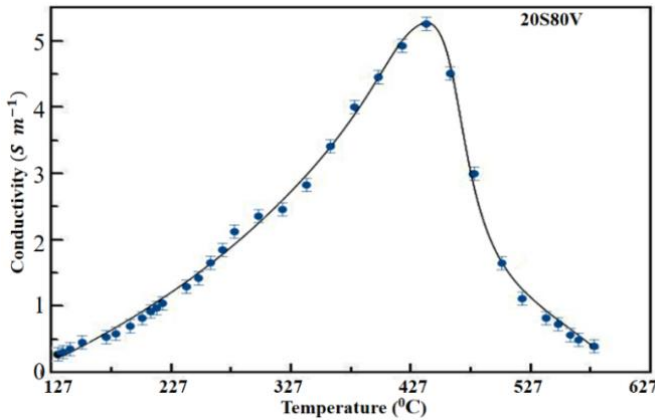


Fig. 6 Variation of conductivity with a temperature of 20S80V base glass.

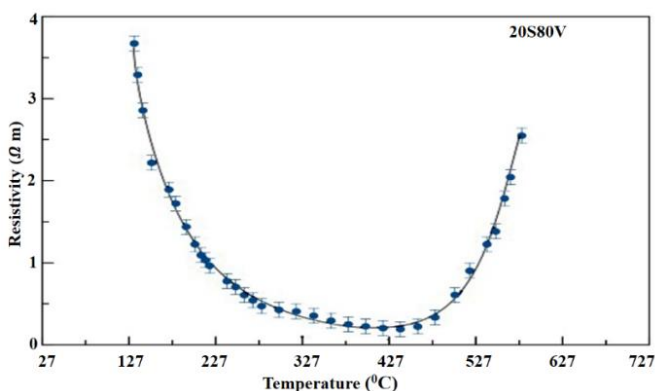


Fig. 7 Variation of resistivity with temperatures.

The measured resistivity of the specimen 20S80V decreases with increasing temperatures up to 427 °C is a behavior of semiconductor but metallic behavior is observed above this temperature (Fig. 7). This scenario is due to the increasing concentration of conduction electrons at elevated temperatures.

4 Conclusion

In this study, we have synthesized several silicovanadate glass samples with the variation of compositions by familiar melt quenching method. It was observed that the melting temperature of the glass samples depended on the amount of V_2O_5 present. The infrared spectra of $x\text{SiO}_2(100-x)V_2O_5$ glass system was interpreted in term of various chemical bonds. The FTIR chemical band positions in the glasses have a general tendency to shift towards the high-frequency region with the increase of V_2O_5 concentration. The FTIR spectra indicate that the glass samples contain various local structural units such as Si-O-Si, V-O-V, V-O, O-Si-O, Si-O-V, and V=O. The effect of V_2O_5 is obvious for certain bonding mechanisms where V^{5+} might play a significant role. The formation of O-H bonds expresses the hygroscopic nature of the glass which provides additional information about the structural units. The X-ray diffraction patterns of the 50S50V, 40S60V, 30S70V, 20S80V, and 10S90V base samples show an almost amorphous nature with several haloes. After heat treatment, the glasses have been crystallized with the formation of different silicovanadate compounds. The characterization of samples by the DTA technique measured the T_g , T_x , and T_s temperatures for glass specimens and possible randomly distributed grain of different crystalline phases. The solubility measurements of glass materials manifest the acidic nature and the pH of the sample solution decreases with the increase of V_2O_5 in the glass composition. The measured hardness of glass samples exhibits high H_v - values due to the presence of significant V-bonds in the glass structure. The higher and nonlinear conductivity patterns (I - V curve) of 20S80V glass can be considered for the semi-conductivity of the specimen which has also been supported by temperature-dependent electrical resistivity measurement data.

Acknowledgments

The authors highly debt to Center Science laboratory, Department of Materials Science and Engineering, University of Rajshahi, Bangladesh for FTIR data and Vickers hardness test. The authors also acknowledge the support from the Department of Glass and Ceramics, Rajshahi University of Engineering and Technology, Bangladesh for XRD measurement.

References

- [1] Morey, G.W., 1954. Properties of glass, Monograph series (American Chemical Society), New York, Reinhold.
- [2] Greer, A.L., 1997. Metallic glasses. Current Opinion in Solid State and Materials Science, 2(4), pp.412-416.
- [3] Ahsan, M.R., Uddin, M.A. and Mortuza, M.G., 2005. Infrared study of the effect of P_2O_5 in the structure of lead silicate glasses.
- [4] Seafriends.org.nz., 1994, Retrieved 2012, Mining the sea sand. Website: <http://www.seafriends.org.nz/oceano/seasand.htm>
- [5] Sharma, B.K., 1991. Industrial chemistry. Krishna Prakashan Media.

- [6] ElBatal, F.H., Marzouk, S.Y., Nada, N. and Desouky, S.M., 2007. Gamma-ray interaction with copper-doped bismuth–borate glasses. *Physica B: Condensed Matter*, 391(1), pp.88-97.
- [7] Pönitzsch, A., Nofz, M., Wondraczek, L. and Deubener, J., 2016. Bulk elastic properties, hardness and fatigue of calcium aluminosilicate glasses in the intermediate-silica range. *Journal of Non-Crystalline Solids*, 434, pp.1-12.
- [8] Sindhu, S., Sanghi, S., Agarwal, A., Kishore, N. and Seth, V.P., 2007. Effect of V₂O₅ on structure and electrical properties of zinc borate glasses. *Journal of Alloys and Compounds*, 428(1-2), pp.206-213.
- [9] Singh, G.P., Kaur, P., Kaur, S. and Singh, D.P., 2011. Role of V₂O₅ in structural properties of V₂O₅-MnO₂-PbO-B₂O₃ glasses. *Materials Physics and Mechanics*, 12, pp.58-63.
- [10] Seshasayee, M. and Muruganandam, K., 1998. Molecular dynamics study of V₂O₅ glass. *Solid State Communications*, 105(4), pp.243-246.
- [11] Mott, N.F., 1968. Conduction in glasses containing transition metal ions. *Journal of Non-Crystalline Solids*, 1(1), pp.1-17.
- [12] John, V., 1992. Introduction to engineering materials. 3rd Edition, *Macmillan Education Ltd*.
- [13] Dekker, A. J., 1995. Solid-state physics, *Macmillan India Limited, New Delhi*, 110064.
- [14] Cicconi, M.R., Lu, Z., Uesbeck, T., van Wüllen, L., Brauer, D.S. and De Ligny, D., 2020. Influence of Vanadium on optical and mechanical properties of aluminosilicate glasses. *Frontiers in Materials*, 7, p.161.
- [15] Lewis, C.E., 1959. The biological effects of vanadium: II. The signs and symptoms of occupational vanadium exposure. *Journal of Occupational and Environmental Medicine*, 1(10), p.572.
- [16] Kumar, V., Pandey, O.P. and Singh, K., 2010. Structural and optical properties of barium borosilicate glasses. *Physica B: Condensed Matter*, 405(1), pp.204-207.
- [17] Limbach, R., Rodrigues, B.P. and Wondraczek, L., 2014. Strain-rate sensitivity of glasses. *Journal of Non-crystalline Solids*, 404, pp.124-134.
- [18] Stevansson, B. and Edén, M., 2013. Structural rationalization of the microhardness trends of rare-earth aluminosilicate glasses: interplay between the RE³⁺ field-strength and the aluminum coordinations. *Journal of Non-crystalline Solids*, 378, pp.163-167.
- [19] Becher, P.F., Waters, S.B., Westmoreland, C.G. and Riester, L., 2002. Compositional effects on the properties of Si-Al-RE-based oxynitride glasses (RE= La, Nd, Gd, Y, or Lu). *Journal of the American Ceramic Society*, 85(4), pp.897-902.
- [20] Rouxel, T., 2007. Elastic properties and short-to medium-range order in glasses. *Journal of the American Ceramic Society*, 90(10), pp.3019-3039.
- [21] Smedskjaer, M.M., Jensen, M. and Yue, Y., 2010. Effect of thermal history and chemical composition on hardness of silicate glasses. *Journal of Non-crystalline Solids*, 356(18-19), pp.893-897.
- [22] Zheng, Q., Potuzak, M., Mauro, J.C., Smedskjaer, M.M., Youngman, R.E. and Yue, Y., 2012. Composition–structure–property relationships in boroaluminosilicate glasses. *Journal of Non-crystalline Solids*, 358(6-7), pp.993-1002.
- [23] Seshasayee, M. and Muruganandam, K., 1998. Molecular dynamics study of V₂O₅ glass. *Solid State Communications*, 105(4), pp.243-246.
- [24] Kubuki, S., Matsuda, K., Akiyama, K., Homonnay, Z., Sinkó, K., Kuzmann, E. and Nishida, T., 2013. Enhancement of electrical conductivity and chemical durability of 20R2O• 10Fe2O3• xWO3•(70– x) V2O5 glass (R= Na, K) caused by structural relaxation. *Journal of Non-crystalline Solids*, 378, pp.227-233.
- [25] Ghosh, A. and Chakravorty, D., 1993. Electrical conduction in some sol-gel silicate glasses. *Physical Review B*, 48(8), p.5167.
- [26] Ghosh, A., 1990. Ac conduction in iron bismuthate glassy semiconductors. *Physical Review B*, 42(2), p.1388.
- [27] Dutta, D. and Ghosh, A., 2005. Dynamics of Ag⁺ ions in binary tellurite glasses. *Physical Review B*, 72(2), p.024201.
- [28] Striepe, S., Da, N., Deubener, J. and Wondraczek, L., 2012. Micromechanical properties of (Na, Zn)-sulfophosphate glasses. *Journal of Non-crystalline Solids*, 358(6-7), pp.1032-1037.
- [29] Striepe, S., Smedskjaer, M.M., Deubener, J., Bauer, U., Behrens, H., Potuzak, M., Youngman, R.E., Mauro, J.C. and Yue, Y., 2013. Elastic and micromechanical properties of isostatically compressed soda–lime–borate glasses. *Journal of Non-crystalline Solids*, 364, pp.44-52.
- [30] Krishna Mohan, N., Sahaya Baskaran, G. and Veeraiah, N., 2006. Dielectric and spectroscopic properties of PbO–Nb₂O₅–P₂O₅: V₂O₅ glass system. *Physica Status Solidi (a)*, 203(8), pp.2083-2102.
- [31] Subbalakshmi, P., Sastry, P.S. and Veeraiah, N., 2001. Dielectric relaxation and ac conduction phenomena in PbO–WO₃–P₂O₅ glass system. *Physics and Chemistry of Glasses*, 42(4-5), pp.307-314.
- [32] Iordanova, R., Dimitrov, V., Dimitriev, Y. and Klissurski, D., 1994. Glass formation and structure of glasses in the V₂O₅- MoO₃- Bi₂O₃ system. *Journal of Non-crystalline Solids*, 180(1), pp.58-65.
- [33] Iordanova, R., Dimitriev, Y., Dimitrov, V., Kassabov, S. and Klissurski, D., 1996. Glass formation and structure in the V₂O₅- Bi₂O₃- Fe₂O₃ glasses. *Journal of Non-crystalline Solids*, 204(2), pp.141-150.
- [34] Merzbacher, C.I. and White, W.B., 1991. The structure of alkaline earth aluminosilicate glasses as determined by vibrational spectroscopy. *Journal of Non-Crystalline Solids*, 130(1), pp.18-34.
- [35] Wan, J., Cheng, J. and Lu, P., 2008. The coordination state of B and Al of borosilicate glass by IR spectra. *Journal of Wuhan University of Technology-Mater. Sci. Ed.*, 23(3), pp.419-421.
- [36] Kohli, J.T., Condrate, R.A. and Shelby, J.R., 1993. Raman and infrared spectra of rare earth aluminosilicate glasses. *Physics and Chemistry of Glasses*, 34(3), pp.81-87.
- [37] Hayri, E.A., Greenblatt, M., Bruna, P. and Gerhardt, R., 1989. Na₂O- P₂O₅- SiO₂ gels: Preparation and characterization. *Journal of Non-crystalline Solids*, 111(2-3), pp.167-172.
- [38] Khalifa, F.A., El Hadi, Z.A., El-Keshen, A.A. and Moustaffa, F.A., 1996. Synthesis and infrared spectra of high lead silicate glasses with di-, tri-or tetravalent cations: A structure correlation. *Indian Journal of Pure & Applied Physics*, 34(4), pp.201-210.

- [39] Rada, S., Neumann, M. and Culea, E., 2010. Experimental and theoretical investigations on the structure of the lead–vanadate–tellurate unconventional glasses. *Solid State Ionics*, 181(25-26), pp.1164-1169.
- [40] Rada, S., Ristoiu, T., Rada, M., Dan, V., Coroiu, I., Barlea, M., Rusu, T. and Culea, E., 2010. Towards understanding of the photosensitive properties in lead–vanadate–tellurate unconventional glasses. *Materials Research Bulletin*, 45(11), pp.1598-1602.
- [41] Rada, M., Rus, L., Rada, S., Pascuta, P., Stan, S., Dura, N., Rusu, T. and Culea, E., 2015. Role of vanadium ions on structural, optical and electrochemical properties of the vanadate-lead glasses. *Journal of Non-Crystalline Solids*, 414, pp.59-65.
- [42] Gandhi, Y., Venkatramaiah, N., Kumar, V.R. and Veeraiah, N., 2009. Spectroscopic and dielectric properties of ZnF₂–As₂O₃–TeO₂ glass system doped with V₂O₅. *Physica B: Condensed Matter*, 404(8-11), pp.1450-1464.
- [43] El-Bata, H.A., Ghoheim, K.A., Abd El-shafi, N. and Azooz, M.A., 2000. Infrared spectra and crystallization of some Li₂O–SiO₂ glasses and the effect of CaO, Al₂O₃ and K₂O additives. *Indian Journal of Pure & Applied Physics*, 38(2), pp.101-109.
- [44] Dimitrov, V., Dimitriev, Y. and Montenero, A., 1994. IR spectra and structure of V₂O₅–GeO₂–Bi₂O₃ glasses. *Journal of Non-Crystalline Solids*, 180(1), pp.51-57.
- [45] Srikumar, T., Rao, C.S., Gandhi, Y., Venkatramaiah, N., Ravikumar, V. and Veeraiah, N., 2011. Microstructural, dielectric and spectroscopic properties of Li₂O–Nb₂O₅–ZrO₂–SiO₂ glass system crystallized with V₂O₅. *Journal of Physics and Chemistry of Solids*, 72(3), pp.190-200.
- [46] Rao, P.T. and Vasundhara, B., 2015. Thermal and FT-IR Properties of Semiconducting SnO₂–PbO–V₂O₅ Glass System. *New Journal of Glass and Ceramics*, 5(03), p.53.
- [47] Wang, D.S. and Pantano, C.G., 1992. Structural characterization of CaO–B₂O₃–Al₂O₃–SiO₂ xerogels and glasses. *Journal of Non-crystalline Solids*, 142, pp.225-233.
- [48] King, P.L., Ramsey, M.S., McMillan, P.F., and Swayze, G.A., 2004. Infrared Spectroscopy in Geochemistry, Exploration Geochemistry and Remote Sensing. *Mineral. Assoc. Canada Short Course Series*, 33, pp.57-91.
- [49] Wong, J., 1976. Vibrational spectra of vapor-deposited binary phosphosilicate glasses. *Journal of Non-Crystalline Solids*, 20(1), pp.83-100.
- [50] King, P.L., Ramsey, M.S., McMillan, P.F., and Swayze, G.A., 2004. Infrared Spectroscopy in Geochemistry, Exploration Geochemistry and Remote Sensing. *Mineral. Assoc. Canada Short Course Series*, 33, pp.93-133.
- [51] Ahsan, M.R. and Mortuza, M.G., 2005. Infrared spectra of xCaO (1–x–z) SiO₂zP₂O₅ glasses. *Journal of Non-Crystalline Solids*, 351(27-29), pp.2333-2340.
- [52] Chen, A. and James, P.F., 1988. Amorphous phase separation and crystallization in a lithium silicate glass prepared by the sol-gel method. *Journal of Non-crystalline Solids*, 100(1-3), pp.353-358.
- [53] Rao, N.S., Purnima, M., Bale, S., Kumar, K.S. and Rahman, S., 2006. Spectroscopic investigations of Cu²⁺ in Li₂O–Na₂O–B₂O₃–Bi₂O₃ glasses. *Bulletin of Materials Science*, 29(4), pp.365-370.
- [54] Mandal, S. and Hazra, S., 2000. Structural and physical properties of Fe₂O₃-doped lead vanadate glass. *Journal of Materials Research*, 15(1), pp.218-221.
- [55] Higazy, A.A. and Bridge, B., 1985. Infrared spectra of the vitreous system Co₃O₄–P₂O₅ and their interpretation. *Journal of Materials Science*, 20(7), pp.2345-2358.
- [56] Innocenzi, P., 2003. Infrared spectroscopy of sol–gel derived silica-based films: a spectra-microstructure overview. *Journal of Non-crystalline Solids*, 316(2-3), pp.309-319.
- [57] Lofaj, F., Satet, R., Hoffmann, M.J. and de Arellano Lopez, A.R., 2004. Thermal expansion and glass transition temperature of the rare-earth doped oxynitride glasses. *Journal of the European Ceramic Society*, 24(12), pp.3377-3385.
- [58] Hanifi, A.R., Genson, A., Pomeroy, M.J. and Hampshire, S., 2012. Independent but additive effects of fluorine and nitrogen substitution on properties of a calcium aluminosilicate glass. *Journal of the American Ceramic Society*, 95(2), pp.600-606.
- [59] Iftekhar, S., Pahari, B., Okhotnikov, K., Jaworski, A., Svensson, B., Grins, J. and Edén, M., 2012. Properties and structures of RE₂O₃–Al₂O₃–SiO₂ (RE= Y, Lu) glasses probed by molecular dynamics simulations and solid-state NMR: the roles of aluminum and rare-earth ions for dictating the microhardness. *The Journal of Physical Chemistry C*, 116(34), pp.18394-18406.

Appendix A

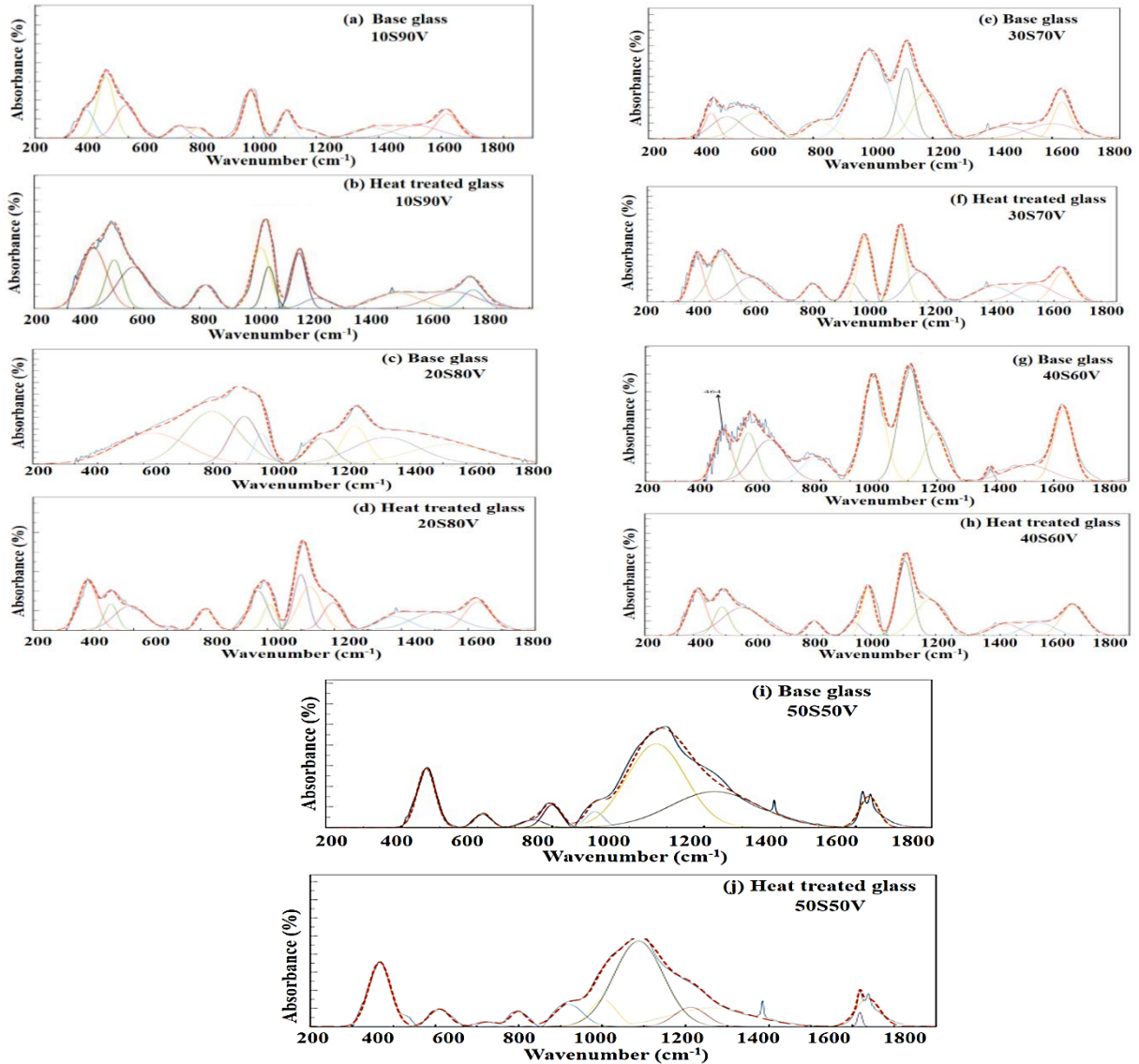


Fig. A1 (a), (b), (c), (d), (e), (f), (g), (h), (i) and (j) show the deconvoluted spectra of $x\text{SiO}_2(100-x)\text{V}_2\text{O}_5$ system base and heat treated glasses with $x = 10, 20, 30, 40$ and 50 mol % respectively.

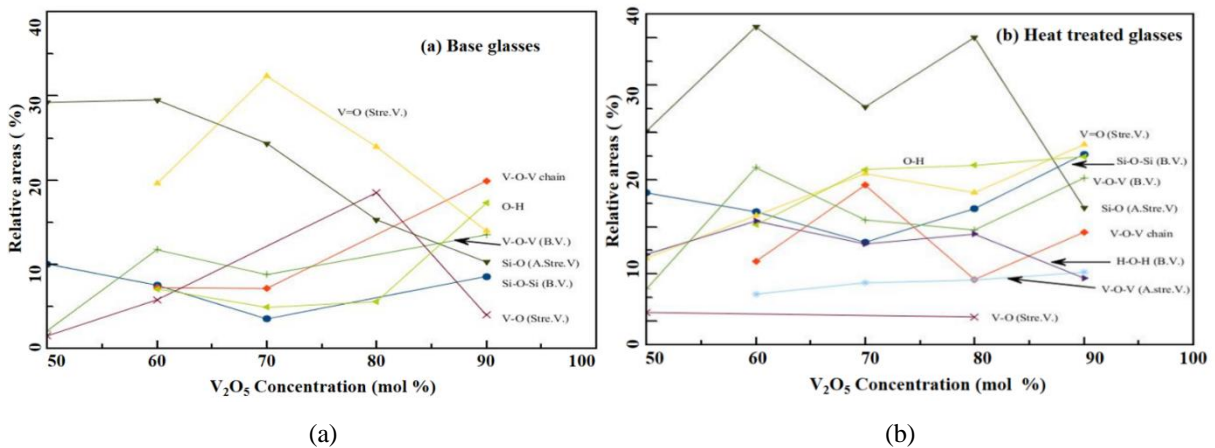


Fig. A2 (a) and (b) Relative areas of the chemical bonds as a function of V_2O_5 Concentration in mol% of $x\text{SiO}_2(100-x)\text{V}_2\text{O}_5$ base and heat treated glasses respectively.

Numerical Investigation of Liquid–Liquid Mixing in Modified T Mixer with 3D Obstacles

Md. Readul Mahmud

Department of Physical Sciences, Independent University, Bangladesh (IUB), Dhaka-1229, Bangladesh

Received: April 15, 2021, Revised: May 08, 2021, Accepted: May 11, 2021, Available Online: June 14, 2021

ABSTRACT

The fluids inside passive micromixers are laminar in nature and mixing depends primarily on diffusion. Hence mixing efficiency is generally low, and requires a long channel length and longtime compare to active mixers. Various designs of complex channel structures with/without obstacles and three-dimensional geometries have been investigated in the past to obtain an efficient mixing in passive mixers. This work presents a design of a modified T mixer. To enhance the mixing performance, circular and hexagonal obstacles are introduced inside the modified T mixer. Numerical investigation on mixing and flow characteristics in microchannels is carried out using the computational fluid dynamics (CFD) software ANSYS 15. Mixing in the channels has been analyzed by using Navier–Stokes equations with water–water for a wide range of the Reynolds numbers from 1 to 500. The results show that the modified T mixer with circular obstacles has far better mixing performance than the modified T mixer without obstacles. The reason is that fluids' path length becomes longer due to the presence of obstacles which gives fluids more time to diffuse. For all cases, the modified T mixer with circular obstacle yields the best mixing efficiency (more than 60%) at all examined Reynolds numbers. It is also clear that efficiency increase with axial length. Efficiency can be simply improved by adding extra mixing units to provide adequate mixing. The value of the pressure drop is the lowest for the modified T mixer because there is no obstacle inside the channel. Modified T mixer and modified T mixer with circular obstacle have the lowest and highest mixing cost, respectively. Therefore, the current design of modified T with circular obstacles can act as an effective and simple passive mixing device for various micromixing applications.

Keywords: Micro device, CFD, SAR, Mixing efficiency, Mixing cost.



This work is licensed under a [Creative Commons Attribution-Non Commercial 4.0 International License](https://creativecommons.org/licenses/by-nc/4.0/).

1 Introduction

Mixing different ingredients is a common scenario of everyday life but achieve good or homogeneous mixing is not always easy. Micro-devices and micro-mixers serve the purpose to achieve excellent mixing in micro-scale [1]. The application of micro-devices is increasing every day in various chemical processes and synthesis [2], particle synthesis, [3] biomedical and biochemical analysis [4], dynamic cell separation [5], Bio Micro-Electro-Mechanical Systems (BioMEMS), and micro-total analysis systems [6]. Micromixers possess a high surface-to-volume ratio due to their small linear dimensions, a characteristic from which derives most of their advantages over conventional-size chemical processes equipment [7]. In the micro-scale, the flow is mostly laminar at a low Reynolds number and the mixing entirely depends on the molecular diffusion [8]. Hence long length and a long time are required to yield good mixing [9]. Microdevices offer many advantages over traditional equipment such as process safety, low cost to manufacture, better process control, simpler process optimization, rapid design implementation, and easier scale-up through numbering up [7], [10]–[12]. Another major advantage of micromixers is the consumption of significantly less amount of sample and reagent than other known experimental platforms due to its small dimension [13]–[14].

Micromixers are generally divided into two categories, active and passive [15]–[16]. Passive mixers have no active components but use the long channel length and specific geometric configuration to increase the interfacial area between fluids for higher mixing [12]. On contrary, active mixers use active elements to achieve mixing such as acoustic/ultrasonic,

dielectrophoretic, electrokinetic time-pulse, pressure perturbation, electro-hydrodynamic, magnetic or thermal techniques to enhance the mixing performance [17]. Though active mixer is more compact and offers higher efficiency [18], passive mixers are economical, convenient, and can easily be incorporated into LOC systems, and protect sensitive bio-reagents [19].

The earliest and the simplest passive mixers are T shape and Y shape micromixers. The detailed evaluation and working principle of passive mixer including T-shaped micromixers have been investigated extensively in recent years [19]–[24]. Many authors investigate the flow regime, the influence of secondary flow, vortex flow, and mixing performance of T mixers numerically or/and experimentally [2], [11], [25]–[27]. Simple T mixer has low efficiency due to its laminar flow and absence of chaotic advection at low Reynolds number. As a result, good mixing requires long channel length and longtime [28]. To negate this disadvantage, obstacles or grooves are introduced inside the mixers to introduce chaotic advection. Many T mixers have been investigated [12], [29]–[33] which provide an improved mixing quality but incurred a considerably large pressure drop due to the presence of obstacles. Therefore, it is still a challenge to design and optimize T-shaped micromixers with obstacles to achieve higher mixing efficiency with lower mixing costs.

In this present work, a simple T mixer and a modified T mixer are presented. The purpose of the work is to improve the efficiency of the modified T mixer by introducing 3D obstacles. Circular-shaped and hexagonal-shaped obstacles are introduced inside the modified T mixers to enhance the mixing performance.

Numerical simulation is performed using ANSYS Fluent 15 over a wide range of Reynolds numbers from 1 to 500. The numerical data for a simple T mixer is compared with published work to validate the numerical work. Finally, the overall comparative analysis is performed to propose the best-performing mixer.

2 Design of Device

A simple T shape mixer generally has two inlets and one outlet. The geometry of a simple T mixer investigated by Gianni Orsi et al. [34] is presented in Fig. 1. The inlet channels present a square cross-section, i.e., $W_i = H = 0.1 \text{ mm}$, whereas the outflow channel has an aspect ratio 2:1, i.e., $W_o = 2H =$

0.2 mm . A modified T shape mixer was designed with same inlets and outlet configuration (Fig. 1). The mixing length is kept constant for both mixers, $L = 80H = 8 \text{ mm}$.

To improve the mixing performance, two different types of 3D obstacles namely, circular and hexagonal shapes are placed inside the modified T mixer. The proposed modified T mixer consists of 8 identical elements, each element is 1 mm long; the minimum and maximum width is 0.1 mm and 0.2 mm , respectively. Fig. 2 shows the dimension and location of different obstacles inside of an element, as an example of the proposed modified T mixer.

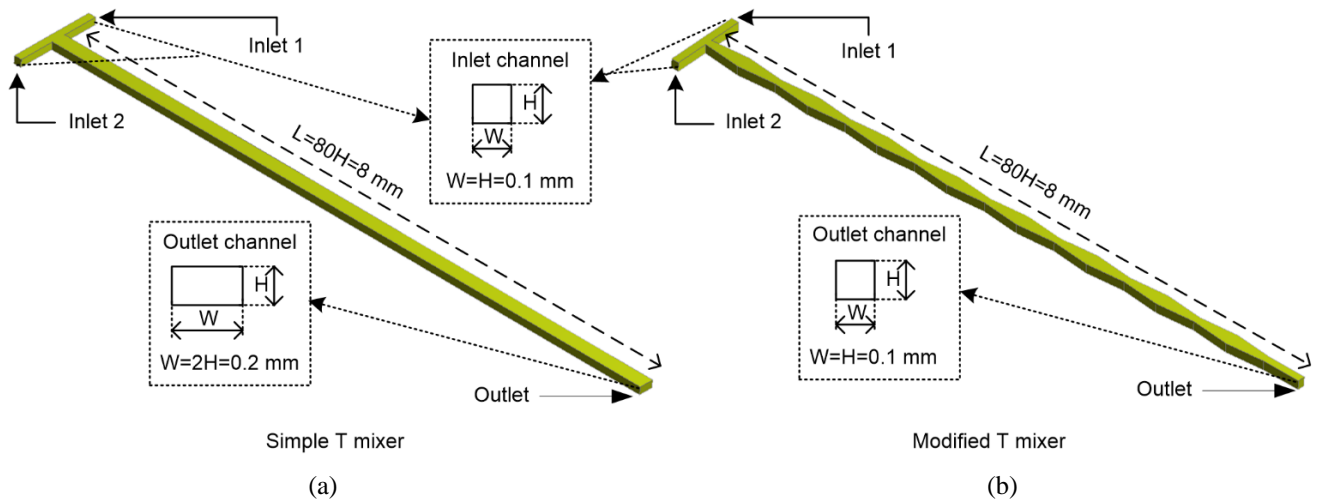


Fig. 1 (a) Simple T mixer and (b) modified T mixer with dimension

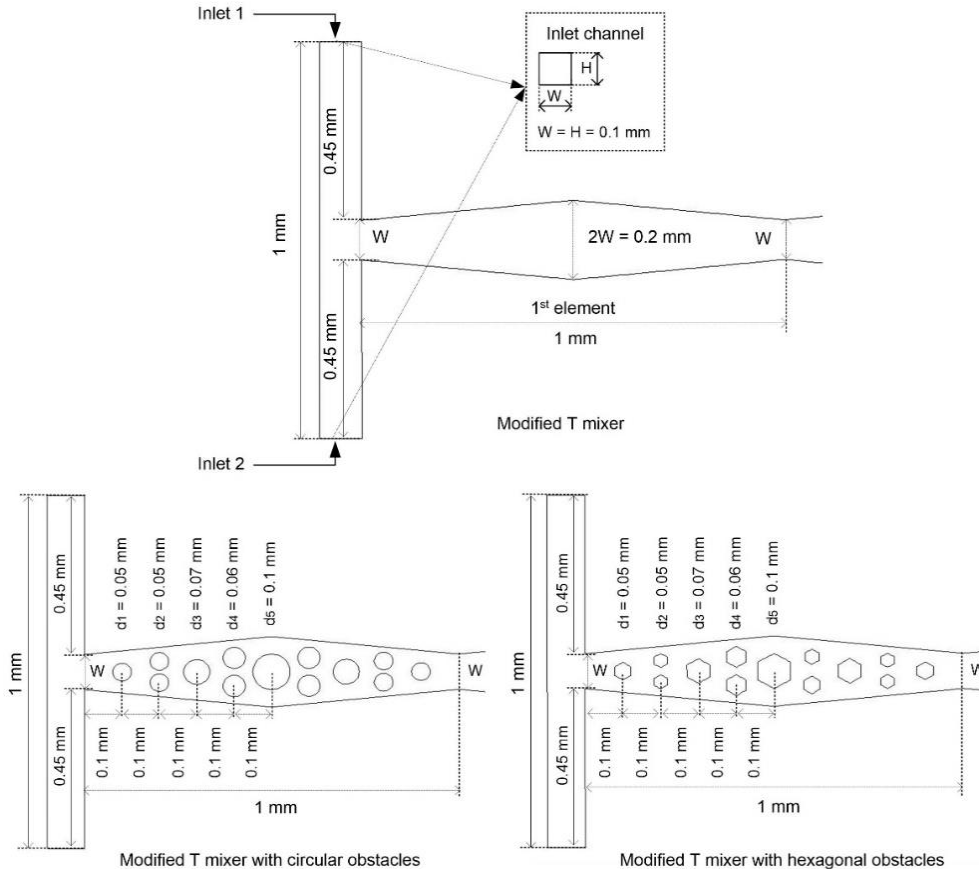


Fig. 2 A single element of modified T, modified T with circular obstacle and modified T with hexagonal mixer

3 Simulation Setup and Numerical Methodology

A commercial software ANSYS Fluent 15 is used for numerical simulation purpose. The fluids are considered as Newtonian, steady, incompressible, and the flow field solves using continuity, Navier-Stokes, and advection-diffusion equations as given below [12], [35]-[36]:

$$\nabla \cdot V = 0 \quad (1)$$

$$\rho V \nabla \cdot V = -\nabla P + \mu \nabla^2 V \quad (2)$$

$$JV \cdot \nabla C = D \nabla^2 C \quad (3)$$

Where V, ρ, P, μ, C , and D are the fluid velocity, fluid density, fluid pressure, fluid viscosity, fluid molar concentration, and diffusivity, respectively.

Numerical simulation is performed considering no-slip velocity condition at all walls, uniform concentration, and two inlets are set to velocity inlet and one outlet is set to pressure outlet with zero (0) gauge pressure [37]. The two inlet fluids are considered to have the same properties as water at 20°C with density $\rho = 998.2 \text{ Kg/m}^3$, dynamics viscosity $\mu = 0.001 \text{ Pa}\cdot\text{s}$ and diffusivity $D = 1 \times 10^{-9} \text{ m}^2/\text{s}$ [1], [4]. The fluid concentration at the two inlets is set to 1 and 0, respectively. The SIMPLER algorithm is used to couple the velocity and pressure fields [10]. Numerical simulation always affects by artificial diffusive flux and it is impossible to rid of the numerical error completely. But these errors can be reduced by applying a higher-order solving scheme and decreasing mesh size. Hence, second-order upwind scheme have been used for solving the governing equations [38]. The convergence criterion was set 1×10^{-6} for all parameters.

The Reynolds numbers (Re) are calculated using the following equation using hydraulic diameter (d) [34].

$$Re = \frac{\rho V d}{\mu} \quad (4)$$

$$d = \frac{2WH}{W + H} \quad (5)$$

Where W and H are the mixing channel width and height, respectively. The mixing index is calculated by using the following equations [39]-[40].

$$\sigma = \sqrt{\frac{1}{N} \sum_{i=1}^N (C_i - C_{av})^2} \quad (6)$$

$$\eta = 1 - \sqrt{\frac{\sigma^2}{\sigma_{max}^2}} \quad (7)$$

Where, C_i, C_{av}, σ and σ_{max} are the concentration at the i^{th} node, average concentration, standard deviation, and maximum standard deviation which is 0.5, respectively. The mixing efficiency is denoted by η which ranged from 0 to 1. Complete mixing is equivalent to 1 and non-mixing is equivalent to 0.

To have a comprehensive comparative performance of the mixers, mixing cost (M_C) which is the ratio of efficiency to pressure-drop is computed by following equation [19], [41]:

$$M_C = \frac{\eta}{\Delta P} \quad (8)$$

where $M_C, \Delta P$ and η denote the mixing cost in $1/Pa$, the pressure drop in Pa , and the mixing efficiency, respectively.

3.1 Meshing

Uniform hexahedral mesh was created by applying the sweep method in the Fluent platform. Fig. 3 shows the grid system of the modified T mixer and modified T mixer with circular obstacles, as an example.

The grid independence study was performed for various nodes for all mixers. Fig. 4 shows the grid dependency test of modified T mixer with circular obstacle for six different number of nodes from 3.45×10^5 to 9.31×10^5 . The mixing index was calculated at the outlet at $Re = 50$. It is clear that mixing index decreases considerably with the increase of members of nodes, as expected. However, the variation is very small, about 0.98 % in mixing index between 7.11×10^5 to 9.31×10^5 nodes. Hence 7.11×10^5 nodes are used for further analysis of modified T mixer which will cost-effectively provide acceptable numerical data. Similarly, analyses were performed, and $4.9 \times 10^5, 5.21 \times 10^5, 6.61 \times 10^5$ grid cells were chosen for simple T mixer, modified T mixer, and modified T mixer with hexagonal obstacles, respectively.

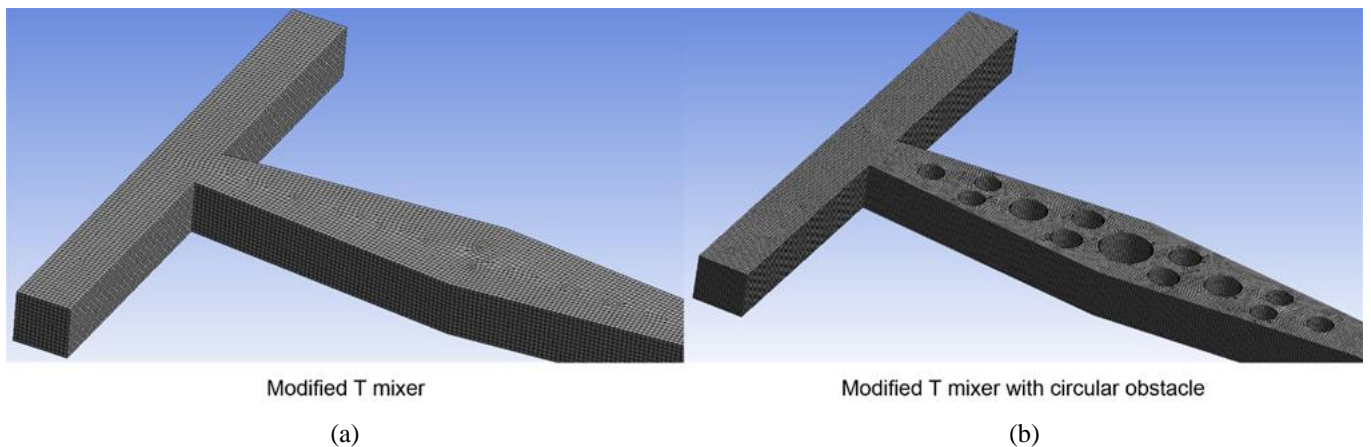


Fig. 3 Uniform hexagonal grid systems inside the (a) modified T and (b) modified T with circular obstacles mixers

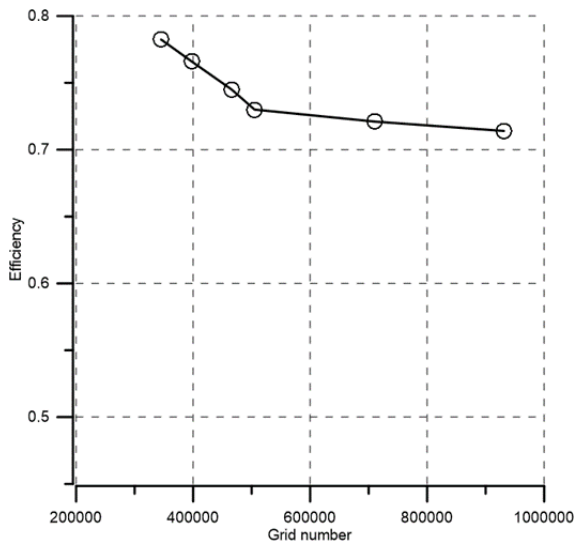


Fig. 4 Dependency of mixing efficiency at the outlet of modified T mixer with circular obstacles at $Re = 50$

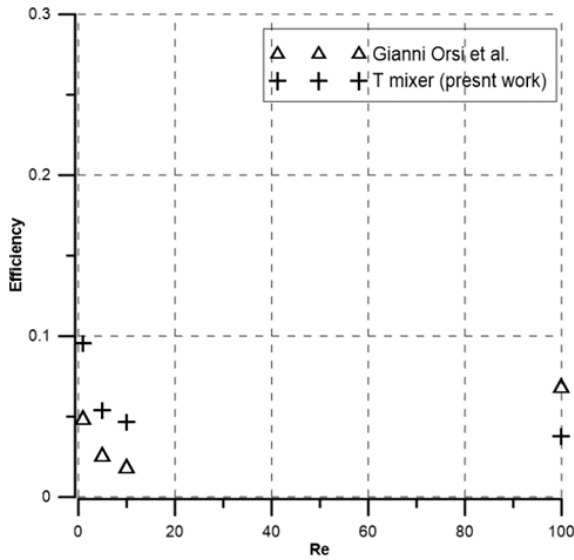


Fig. 5 Comparison of mixing efficiency at a distance of 0.5 mm ($L = 0.5 \text{ mm}$) of a simple T mixer

4 Results and Discussion

Since this work involves numerical simulation, qualitative validation of the CFD model was performed by comparing published data. For this purpose, a simple T mixer is constructed keeping the geometrical configuration exactly the same as the published work by Gianni Orsi et al. [36]. The mixing efficiency of a simple T mixer is compared with the published data [36] for water-water mixing and is demonstrated in Fig. 5. The data shows a similar trend and the similarity between them is in an acceptable range because it is quite difficult to replicate exact simulation results due to lack of detailed information. Hence it can be safely assumed that the simulation model is acceptable for the purpose of this work.

Now the comparison between a simple T mixer and the modified T mixer is present in Fig. 6. The mixing efficiency is calculated at the outlet for both mixers ($L = 8 \text{ mm}$). The efficiency is relatively low for both mixers, less than 30%, but the modified T mixer shows three times higher efficiency compare to the simple T mixer. Hence modified T mixer is chosen for further analysis with different shaped obstacles.

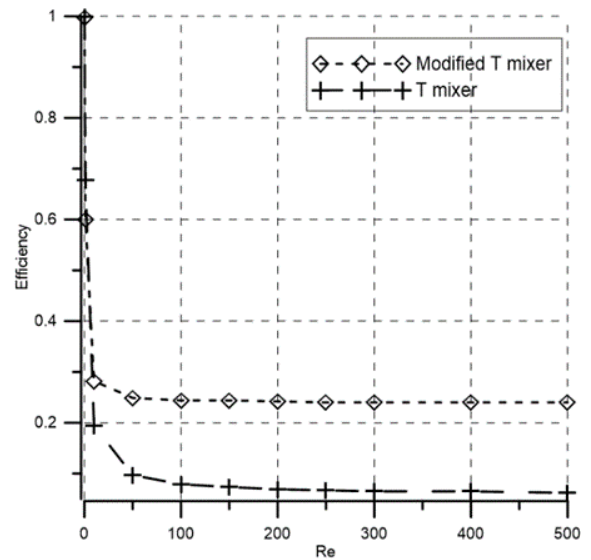


Fig. 6 Mixing efficiency at the outlet ($L = 8.5 \text{ mm}$) of a simple T and the modified T mixer

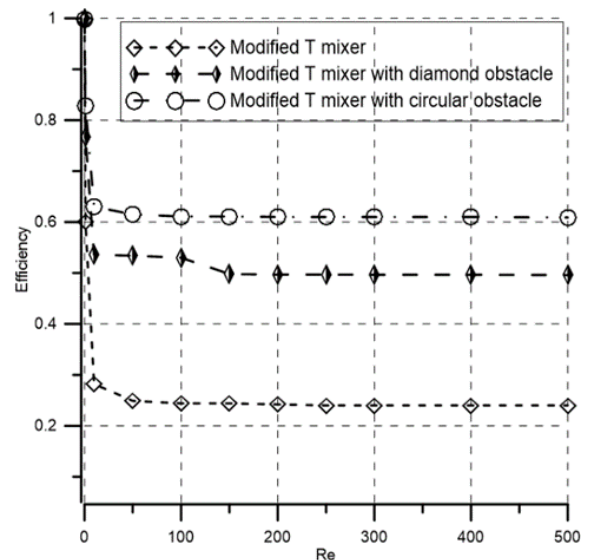


Fig. 7 Mixing efficiency at the outlet of modified T mixers

To improve the mixing performance, circular-shaped and hexagonal-shaped obstacles are placed inside the modified T mixer. Fig. 7 presents the progress of mixing at different Reynolds numbers inside the modified T mixer with circular obstacles and modified T mixer with hexagonal obstacles. The efficiency is computed at the outlet of all mixers on the XY plane for $1 \leq Re \leq 500$. All mixers have good mixing efficiency, (more than 70%) at low Reynolds numbers ($Re \leq 1$). It is also found that mixing efficiency of three mixers subsequently decreases with the increase of Reynolds numbers. T mixer with circular obstacle shows the highest efficiency ($\eta > 60\%$) throughout the Reynolds numbers range compare to the other two mixers. At low Reynolds numbers ($Re \leq 1$) fluids have more time to mix inside the mixer channel, hence all mixers show good efficiency. At high Reynolds numbers ($Re \geq 10$), mixing time decrease and as a consequence efficiency decreases as well. The fluids concentration inside the three mixers at $Re = 1$ and $Re = 100$ are presented in the Fig. 8. It is clear that fluids homogeneity decreases at higher Reynolds numbers ($Re = 100$) which indicate efficiency will be higher at low Reynolds number ($Re = 1$) for all three mixers, as confirmed in Fig. 7.

The distributions of the mass fraction of liquid 1 (water) along the horizontal mid-line, i.e. $x = 8 \text{ mm}$, $y = 0$, $z = 0.05 \text{ mm}$ at the outlet of the four micromixers as shown in Fig. 9. A constant value of the mass fraction equal to 0.5 represents ideal mixing. The distributions of the mass fraction of liquid 1 for the modified T mixer with hexagonal and circular obstacles are close to the ideal distribution, at the minimum and maximum Reynolds number compare to the modified T mixer.

The lowest mass fraction values correspond to the modified T mixer with circular obstacle exhibiting the highest mixing efficiency among the investigated micromixers corresponds to Fig. 7. The change in mass fraction of liquid 1 becomes steeper

as the Reynolds number increases for all mixers. This implies a lower mixing performance at higher Reynolds numbers.

The fluids streamlines presented in Fig. 10 show flow patterns of the three micromixers at $Re = 100$. In case of modified T mixers, the streamlines were parallel and smooth, but streamlines become rough inside the rest two mixers. The two modified T micromixers with obstructions show the split-and-recombination streamlines, which increase the path length of the fluids and responsible for good mixing compared to the modified T mixer.

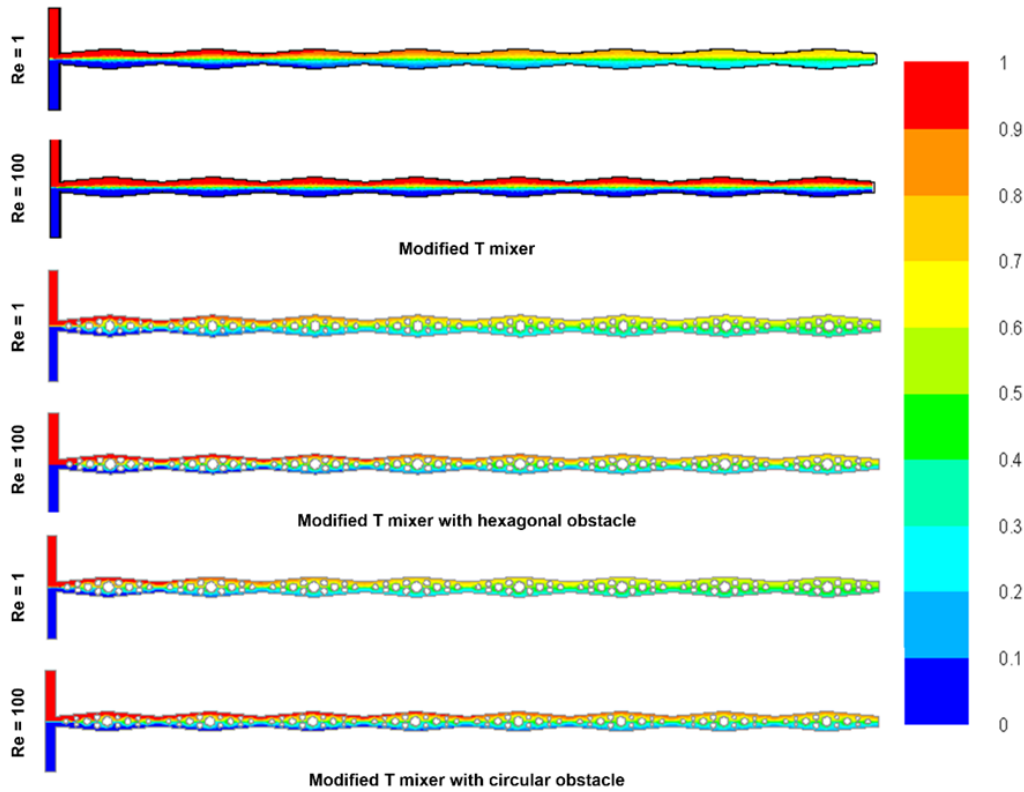


Fig. 8 Concentration of mass fraction of liquids along the channel length of modified T mixer

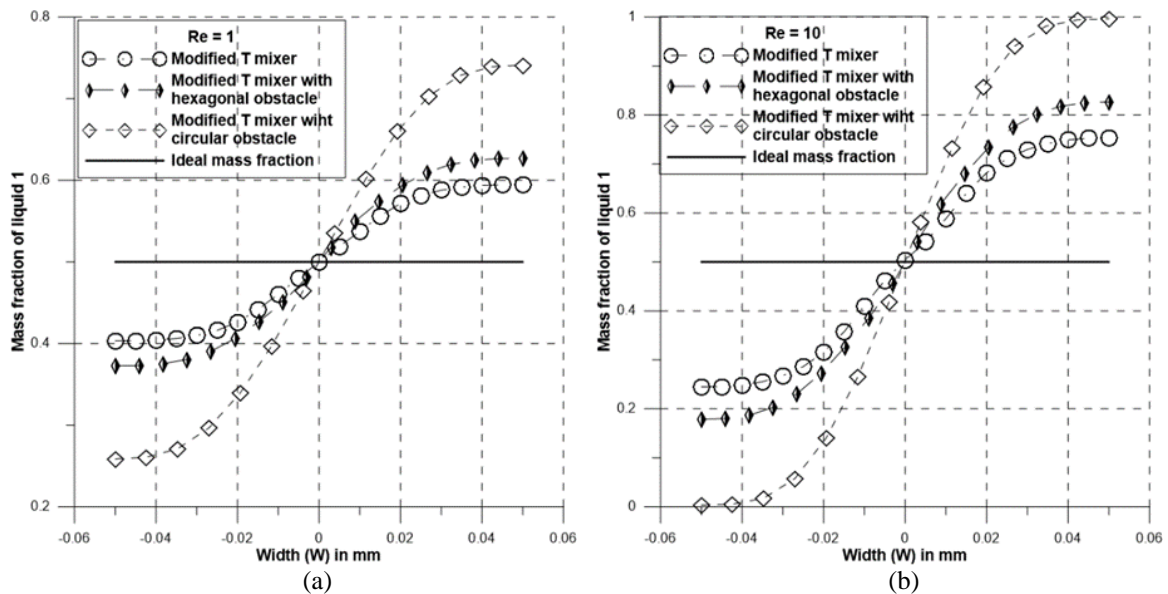


Fig. 9 Distributaries of mass fraction of liquid 1 along the horizontal mid-line ($z = 0.05 \text{ mm}$) at the outlet of modified T mixers at (a) $Re = 1$ and (b) $Re = 10$

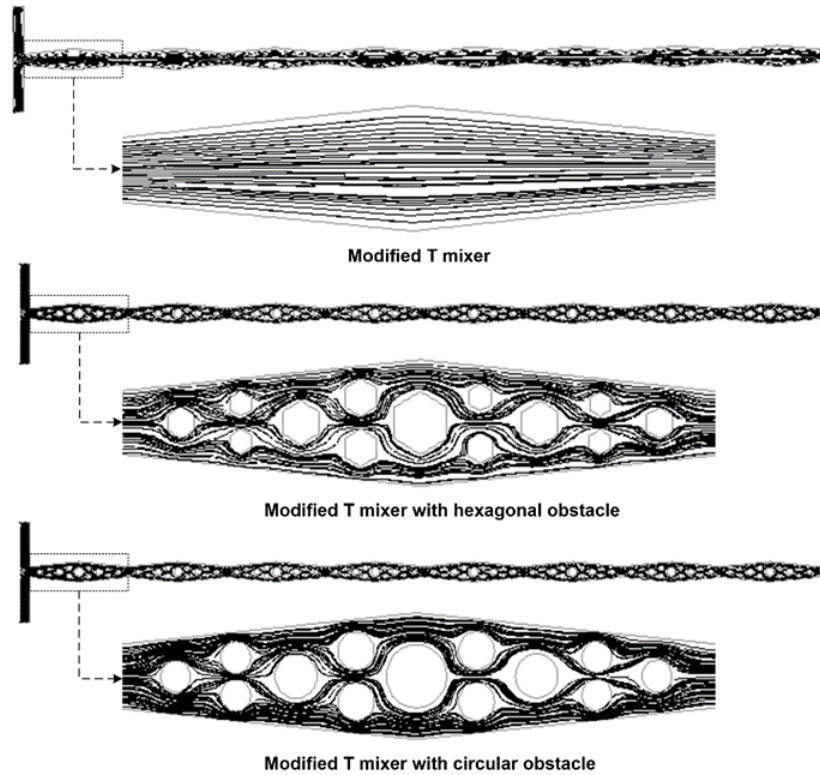


Fig. 10 Fluids streamline inside the modified T mixers at $Re = 100$

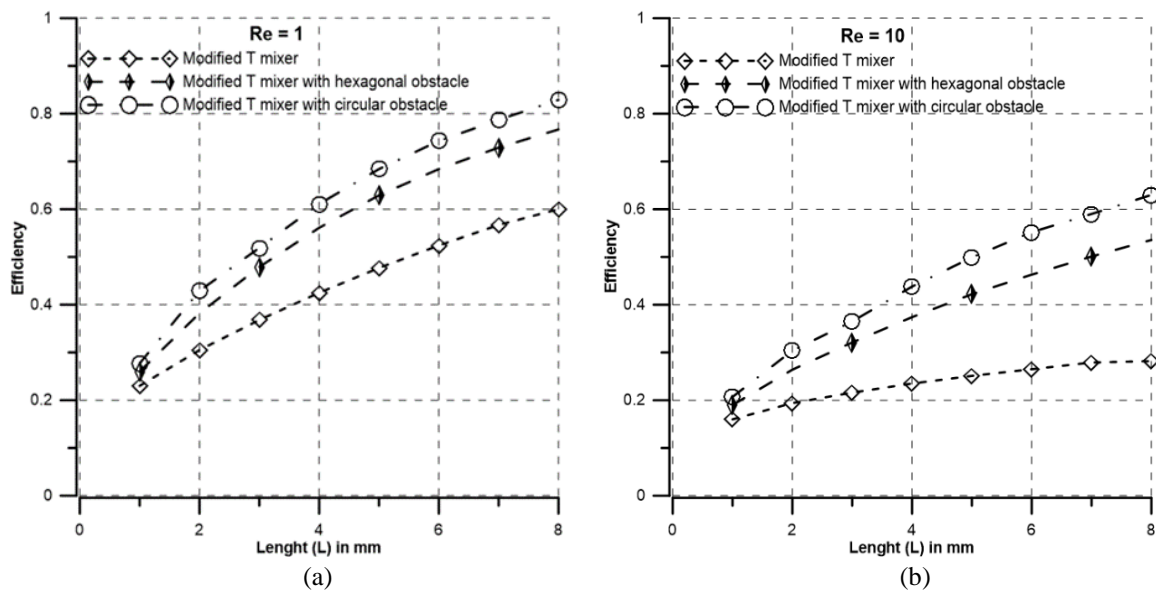


Fig. 11 Mixing efficiency along the length of modified T mixers at (a) $Re = 1$ and (b) $Re = 10$

Mixing efficiency is calculated at several cross-sections along the three micromixer channels at different Reynolds numbers. The efficiency along the axial length at $Re = 1$ and $Re = 100$ is presented in Fig. 11. The highest mixing indices correspond to the T mixer with circular obstacles. Modified T mixer shows the lowest efficiency among the three mixers because of the absence of obstacles. Efficiency increases with the increase of channel length due to a longer mixing time for diffusion.

Efficiency also decreases at a higher Reynolds number, which corresponds to Fig. 7. The two new micromixer designs, modified T and modified T with hexagonal obstacles have mixing indices of 60% and 77% respectively, at the outlet for $Re = 1$. Whereas, the efficiency is 82% in the case of the

modified T mixer with circular obstacles. At $Re = 10$, efficiency decrease to 28%, 53%, and 63% at the outlet of modified T, modified T with hexagonal obstacles, and modified T with circular obstacles, respectively.

The pressure-drop variation as a function of Reynolds numbers for micromixers is shown in Fig. 12. The energy required to drive the fluid from the inlet to the outlet depends on the pressure drop which in turn increases with an increase in Reynolds numbers and vice versa. The lowest pressure drop is observed for the modified T mixer due to the absence of obstacles. Whereas, modified T mixer with circular obstacles shows the highest pressure drop. To have better overall mixing performance, a parameter named, mixing cost is computed. The best design of a micromixer can be determined by computing the

mixing cost for three micromixers. The computed mixing cost for three mixers at $Re = 1$ and $Re = 100$ is present in Fig. 13. The mixing cost of the modified T mixer with circular obstacles is the lowest one compare to the studied three mixers. Modified T mixer with circular obstacles, has the highest efficiency and lowest mixing cost, indicates the best performing mixers among three micromixers.

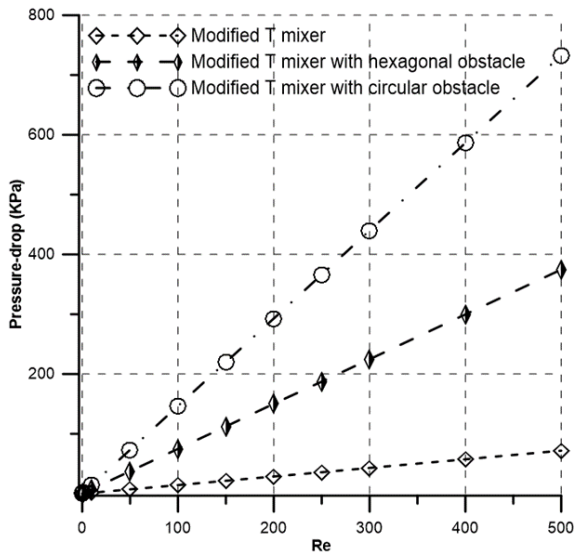


Fig. 12: Pressure-drop at the outlet of modified T mixers

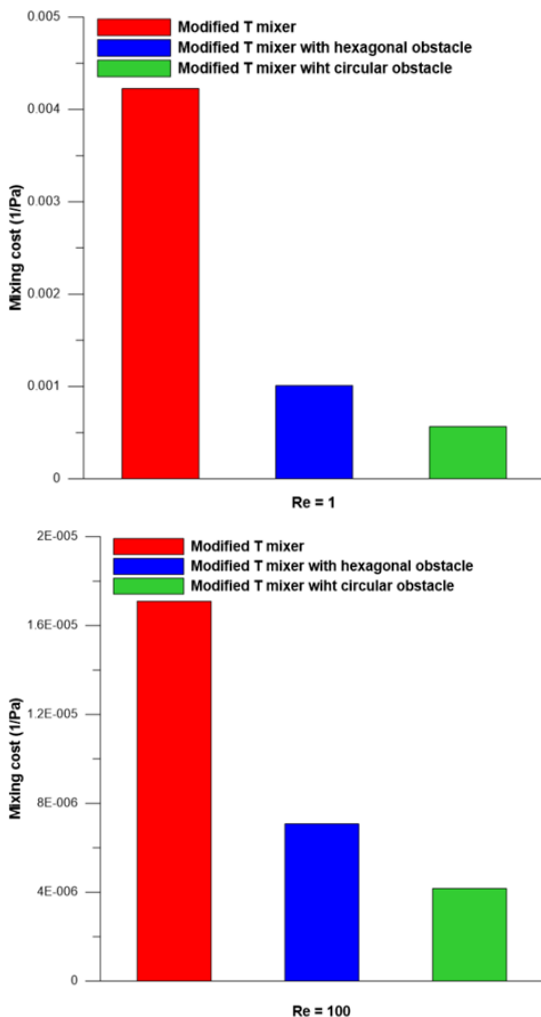


Fig. 13: Mixing cost of modified T mixers at (a) $Re=1$ and (b) $Re=100$

5 Conclusion

T mixer is one of the earliest and simplest passive micromixer designs. It is easy to construct and apply in various applications but it has the limitation of poor mixing except at very low Reynolds numbers ($Re < 1$). Many T mixers incorporate 2D and 3D dimensional baffles or obstacles to overcome these limitations. However, pressure drop always increases due to the presence of obstacles. In the present study, a simple T and a modified T mixer are designed and analyzed for a wide range of Reynolds numbers by ANSYS Fluent 15. The numerical data yield from the simple T mixer is compared with published results to justify the present numerical work. A small improvement in mixing performance over the Reynolds numbers ranging from 1 to 500 is obtained by the modified T mixer over a simple T mixer. Two kinds of obstacles, namely circular and hexagonal are introduced in the modified T mixers to observe the further increase in mixing performance. The modified T mixer with circular obstacles and modified T mixer with hexagonal obstacles have shown considerable improvement in mixing, but both designs have no notable effect to improve the secondary flow. However, the path lengths of fluids increase inside the modified T mixers with obstacles which in turn give fluids more time to mix, and as a consequence efficiency increases at Reynolds numbers at the mid and high range of Reynolds numbers ($10 \leq Re \leq 500$). Modified T mixer with circular obstacles shows 60% more efficiency compare to a simple T mixer irrespective of Reynolds numbers. Mixing cost is also computed, which allows for a comparison of the performance of all presented micromixers. Though the modified T mixer with circular obstacles provides the highest pressure drop, it also has the highest efficiency and lowest mixing cost at all examined Reynolds numbers ($1 \leq Re \leq 500$).

References

- [1] Rahmannedzad, J. and Mirbozorgi, S.A., 2019. CFD analysis and RSM-based design optimization of novel grooved micromixers with obstructions. *International Journal of Heat and Mass Transfer*, 140, pp.483-497.
- [2] Engler, M., Kockmann, N., Kiefer, T. and Woias, P., 2004. Numerical and experimental investigations on liquid mixing in static micromixers. *Chemical Engineering Journal*, 101(1-3), pp.315-322.
- [3] Bothe, D., Stenich, C. and Warnecke, H.J., 2006. Fluid mixing in a T-shaped micro-mixer. *Chemical Engineering Science*, 61(9), pp.2950-2958.
- [4] Schikarski, T., Trzenschiok, H., Peukert, W. and Avila, M., 2019. Inflow boundary conditions determine T-mixer efficiency. *Reaction Chemistry & Engineering*, 4(3), pp.559-568.
- [5] Wang, X.B., Yang, J., Huang, Y., Vykoukal, J., Becker, F.F. and Gascoyne, P.R., 2000. Cell separation by dielectrophoretic field-flow-fractionation. *Analytical Chemistry*, 72(4), pp.832-839.
- [6] Hossain, S., Ansari, M.A. and Kim, K.Y., 2009. Evaluation of the mixing performance of three passive micromixers. *Chemical Engineering Journal*, 150(2-3), pp.492-501.
- [7] Adeosun, J.T. and Lawal, A., 2009. Numerical and experimental studies of mixing characteristics in a T-junction microchannel using residence-time distribution. *Chemical Engineering Science*, 64(10), pp.2422-2432.
- [8] Shah, I., Kim, S.W., Kim, K., Doh, Y.H. and Choi, K.H., 2019. Experimental and numerical analysis of Y-shaped split and recombination micro-mixer with different mixing units. *Chemical Engineering Journal*, 358, pp.691-706.

- [9] Viktorov, V., Mahmud, M.R. and Visconte, C., 2015. Comparative analysis of passive micromixers at a wide range of Reynolds numbers. *Micromachines*, 6(8), pp.1166-1179.
- [10] Mouheb, N.A., Malsch, D., Montillet, A., Sollic, C. and Henkel, T., 2012. Numerical and experimental investigations of mixing in T-shaped and cross-shaped micromixers. *Chemical Engineering Science*, 68(1), pp.278-289.
- [11] Hoffmann, M., Schlüter, M. and Rübiger, N., 2006. Experimental investigation of liquid-liquid mixing in T-shaped micro-mixers using μ -LIF and μ -PIV. *Chemical Engineering Science*, 61(9), pp.2968-2976.
- [12] Dundi, T.M., Raju, V.R.K. and Chandramohan, V.P., 2019. Characterization of mixing in an optimized designed T-T mixer with cylindrical elements. *Chinese Journal of Chemical Engineering*, 27(10), pp.2337-2351.
- [13] Wong, S.H., Ward, M.C. and Wharton, C.W., 2004. Micro T-mixer as a rapid mixing micromixer. *Sensors and Actuators B: Chemical*, 100(3), pp.359-379.
- [14] Shamloo, A., Vatankhah, P. and Akbari, A., 2017. Analyzing mixing quality in a curved centrifugal micromixer through numerical simulation. *Chemical Engineering and Processing: Process Intensification*, 116, pp.9-16.
- [15] Mondal, B., Mehta, S.K., Patowari, P.K. and Pati, S., 2019. Numerical study of mixing in wavy micromixers: comparison between raccoon and serpentine mixer. *Chemical Engineering and Processing: Process Intensification*, 136, pp.44-61.
- [16] Gidde, R., 2020. On the study of teardrop shaped split and collision (TS-SAC) micromixers with balanced and unbalanced split of subchannels. *International Journal of Modelling and Simulation*, pp.1-10.
- [17] Huang, J.J., Lo, Y.J., Hsieh, C.M., Lei, U., Li, C.I. and Huang, C.W., 2011, February. An electro-thermal micro mixer. In 2011 6th IEEE International Conference on Nano/Micro Engineered and Molecular Systems (pp. 919-922). IEEE.
- [18] Chen, X. and Zhang, L., 2017. A review on micromixers actuated with magnetic nanomaterials. *Microchimica Acta*, 184(10), pp.3639-3649.
- [19] Raza, W., Hossain, S. and Kim, K.Y., 2020. A review of passive micromixers with a comparative analysis. *Micromachines*, 11(5), p.455.
- [20] Cai, G., Xue, L., Zhang, H. and Lin, J., 2017. A review on micromixers. *Micromachines*, 8(9), p.274.
- [21] Nam-Trung, N. and Zhigang, W., 2005. Micromixers—a review. *Journal of Micromechanics and Microengineering*, 15(2), p.R1.
- [22] Lee, C.Y., Wang, W.T., Liu, C.C. and Fu, L.M., 2016. Passive mixers in microfluidic systems: A review. *Chemical Engineering Journal*, 288, pp.146-160.
- [23] Barabash, V.M., Abiev, R.S. and Kulov, N.N., 2018. Theory and practice of mixing: a review. *Theoretical Foundations of Chemical Engineering*, 52(4), pp.473-487.
- [24] Lee, C.Y. and Fu, L.M., 2018. Recent advances and applications of micromixers. *Sensors and Actuators B: Chemical*, 259, pp.677-702.
- [25] Bothe, D., Stemich, C. and Warnecke, H.J., 2008. Computation of scales and quality of mixing in a T-shaped microreactor. *Computers & Chemical Engineering*, 32(1-2), pp.108-114.
- [26] Bothe, D., Lojewski, A. and Warnecke, H.J., 2011. Fully resolved numerical simulation of reactive mixing in a T-shaped micromixer using parabolized species equations. *Chemical Engineering Science*, 66(24), pp.6424-6440.
- [27] Galletti, C., Roudgar, M., Brunazzi, E. and Mauri, R., 2012. Effect of inlet conditions on the engulfment pattern in a T-shaped micro-mixer. *Chemical Engineering Journal*, 185, pp.300-313.
- [28] Nimafar, M., Viktorov, V. and Martinelli, M., 2012. Experimental comparative mixing performance of passive micromixers with H-shaped sub-channels. *Chemical Engineering Science*, 76, pp.37-44.
- [29] Chen, L., Wang, G., Lim, C., Seong, G.H., Choo, J., Lee, E.K., Kang, S.H. and Song, J.M., 2009. Evaluation of passive mixing behaviors in a pillar obstruction poly (dimethylsiloxane) microfluidic mixer using fluorescence microscopy. *Microfluidics and Nanofluidics*, 7(2), pp.267-273.
- [30] Tseng, L.Y., Yang, A.S., Lee, C.Y. and Hsieh, C.Y., 2011. CFD-based optimization of a diamond-obstacles inserted micromixer with boundary protrusions. *Engineering Applications of Computational Fluid Mechanics*, 5(2), pp.210-222.
- [31] Fang, Y., Ye, Y., Shen, R., Zhu, P., Guo, R., Hu, Y. and Wu, L., 2012. Mixing enhancement by simple periodic geometric features in microchannels. *Chemical Engineering Journal*, 187, pp.306-310.
- [32] Ansari, M.A., Kim, K.Y. and Kim, S.M., 2018. Numerical and experimental study on mixing performances of simple and vortex micro T-mixers. *Micromachines*, 9(5), p.204.
- [33] Santana, H.S., Silva Jr, J.L., Tortola, D.S. and Taranto, O.P., 2018. Transesterification of sunflower oil in microchannels with circular obstructions. *Chinese Journal of Chemical Engineering*, 26(4), pp.852-863.
- [34] Orsi, G., Roudgar, M., Brunazzi, E., Galletti, C. and Mauri, R., 2013. Water-ethanol mixing in T-shaped microdevices. *Chemical Engineering Science*, 95, pp.174-183.
- [35] Jeguirim, M., Belhachemi, M., Limousy, L. and Bennici, S., 2018. Adsorption/reduction of nitrogen dioxide on activated carbons: textural properties versus surface chemistry—a review. *Chemical Engineering Journal*, 347, pp.493-504.
- [36] Cortes-Quiroz, C.A., Azarbadegan, A. and Zangeneh, M., 2017. Effect of channel aspect ratio of 3-D T-mixer on flow patterns and convective mixing for a wide range of Reynolds number. *Sensors and Actuators B: Chemical*, 239, pp.1153-1176.
- [37] Mariotti, A., Galletti, C., Salvetti, M.V. and Brunazzi, E., 2019. Unsteady flow regimes in a T-shaped micromixer: Mixing and characteristic frequencies. *Industrial & Engineering Chemistry Research*, 58(29), pp.13340-13356.
- [38] Gobby, D., Angeli, P. and Gavriilidis, A., 2001. Mixing characteristics of T-type microfluidic mixers. *Journal of Micromechanics and Microengineering*, 11(2), p.126.
- [39] Viktorov, V., Mahmud, M.R. and Visconte, C., 2016. Design and characterization of a new HC passive micromixer up to Reynolds number 100. *Chemical Engineering Research and Design*, 108, pp.152-163.
- [40] Shinde, A.B., Patil, A.V. and Patil, V.B., 2020. Enhance the mixing performance of water and ethanol at micro level using geometrical modifications. *Materials Today: Proceedings*.
- [41] Chung, C.K. and Shih, T.R., 2007. A rhombic micromixer with asymmetrical flow for enhancing mixing. *Journal of Micromechanics and Microengineering*, 17(12), p.2495.

Fabrication and Characterization of α -Fe₂O₃ Nanoparticles Dispersed Epoxy Nanocomposites

Muhammad Abdullah Al Mamun^{1*}, Md. Abdus Sabur¹, Md. Abdul Gafur², Hrithita Aftab¹ and G. M. Shafiur Rahman¹

¹Department of Materials Science and Engineering, University of Rajshahi, Rajshahi-6205, Bangladesh

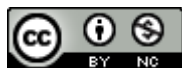
²Institute of Pilot Plant and Process Development Centre, Bangladesh Council of Scientific and Industrial Research (BCSIR), Dhanmondi, Dhaka-1205, Bangladesh

Received: April 09, 2021, Revised: June 02, 2021, Accepted: June 06, 2021, Available Online: June 21, 2021

ABSTRACT

In this work, epoxy resin matrix based polymer nanocomposites were fabricated incorporating sol-gel synthesized hematite (α -Fe₂O₃) nanoparticles. The effect of nanoparticles on chemical, mechanical, electrical, optical and thermal properties in polymer matrix was evaluated. Different functional groups were present in α -Fe₂O₃ nanoparticles, neat epoxy and α -Fe₂O₃/epoxy nanocomposites that obtained from Fourier-Transform Infrared spectroscopy (FTIR). Vibrating Sample Magnetometer (VSM) analysis revealed that the α -Fe₂O₃ nanoparticles have superparamagnetic character. By incorporation of nanoparticles into the epoxy matrix decreased the tensile strength and elongation at break, and increased Young's modulus. In addition, the addition of nanoparticles into the epoxy matrix gradually reduced and increased of the flexural strength and hardness, respectively. The improvement in light absorbance of α -Fe₂O₃/epoxy nanocomposites was increased with increasing the α -Fe₂O₃ content. Conversely, the optical band gap was decreased with increasing nanoparticle addition.

Keywords: α -Fe₂O₃ Nanoparticles, Nanocomposites, Mechanical Properties, Epoxy Resin, Thermogravimetric Analysis (TGA).



This work is licensed under a [Creative Commons Attribution-Non Commercial 4.0 International License](https://creativecommons.org/licenses/by-nc/4.0/).

1 Introduction

Organic-inorganic nanohybrid materials have been widely studied because of their unique properties resulting from the combination of both organic polymer and inorganic nanoparticles [1]-[8]. Also, there has been strong emphasis on the advancement of polymer nanohybrids, in which at least one of the dimensions of the filler has nanometer scale. Researchers have long known that decreasing filler dimension increases the specific surface area of the filler, which in turn may effectively improve the transfer of the load between the polymer matrix and fillers. These nanohybrid materials may exhibit significant enhancements in thermal, mechanical, and electrical properties that are difficult to achieve using conventional fillers with micro scale dimensions, such as carbon, glass, or aramid fibres. In order to reduce the gap between the performances of today's engineering polymers and the ever-increasing demand of engineering applications, new nanohybrids are needed with optimum nanofillers dispersion, improved load transfer-ability from polymer to filler particles, and enhanced thermal properties. Generally, the reinforcement of nano-particles into the polymer matrix enhances the mechanical, dimensional, and thermal stability of the host polymer matrix.

Hematite (α -Fe₂O₃) nanoparticle is an inorganic nanofiller, exhibits some excellent properties like- low cost, environmentally friendly, low toxicity, corrosion and chemically resistance, biocompatibility, and good substrate adherence [7],[8]. Because of these excellent properties, α -Fe₂O₃ nanoparticles are used in water treatment [9], contrast reagents/drug delivery [10], sensor technology [11],[12], optical coatings, magnetic storage [13], field-effect transistors [14], catalysts [15], pigments [16],

etc. α -Fe₂O₃ nanoparticles can be synthesized by several methods, for instance, chemical vapour deposition, hydrothermal synthesis [17], sonochemical technique, chemical precipitation [18], sol-gel technique [19], microemulsion technique [20], hydrolysis [21], ball milling [22], laser ablation, sputtering, and spray pyrolysis [23]. In the past decades until now, there have been numerous investigations of different magnetic nanoparticle-based polymer nanocomposites [24]-[30]. A few examples are mentioned here. In 2008, Dusko Dudic et al. studied the electrical properties of a composite comprising epoxy resin and α -Fe₂O₃ nanorods [24]. In 2017, Prasanna B P et al. synthesized polyaniline/ α -Fe₂O₃ nanocomposite electrode material for super-capacitor applications [25]. In 2016, Ali Mirzaei et al. synthesized and characterized mesoporous α -Fe₂O₃ nanoparticles to investigate the electrical properties of fabricated thick films [26].

On the other hand, epoxy resin is a thermosetting polymer with some excellent properties e.g. light weight, chemically resistance, oil and fuel resistance, electrical insulator, etc. Because of these features epoxy can be used in LEDs, printed circuit boards, inductors, marine applications, coatings, structural adhesives, electrical insulators, and other electrical, electronics, and industrial applications [27]. In 2011, Richard Voo et al. studied different properties of epoxy nanocomposite films [28]. In 2016, A. Kanapitsas et al. studied the dielectric, magnetic, and hydration behaviour of barium ferrite/epoxy nanocomposites [29]. In 2016, Masoomah Gazderazi et al. studied the mechanical and thermal properties of hybridizing MWCNT with nano metal oxides and TiO₂ in epoxy composite [30]. The incorporation of nanofillers into the polymer matrix not

*Corresponding Author Email Address: mamun_mse@ru.ac.bd

only improves the mechanical properties, besides it also helps to extend the application of fabricated nanocomposite [31],[34].

According to previous reports, most work in this field has been done to fabricate α -Fe₂O₃ nanocomposites or Epoxy composites individually. Also, less importance was given to evaluate the mechanical, thermal, and optical properties of α -Fe₂O₃/epoxy nanocomposites. Therefore, the main objective of this work is to synthesized α -Fe₂O₃ nanoparticles which are further dispersed into the epoxy matrix to improve the mechanical and thermal properties as well as optical and electrical properties of α -Fe₂O₃/epoxy nanocomposites.

In the present study, nanocomposites containing epoxy and α -Fe₂O₃ nanoparticles with various compositions were fabricated by solution casting method on flat glass mold. The samples were characterized by various experimental techniques, and the influence of α -Fe₂O₃ nanoparticles on the mechanical, thermal, optical, and electrical properties of α -Fe₂O₃/epoxy nanocomposites was investigated.

2 Experimental Details

2.1 Materials

All the chemical reagents were of analytical grade and used without further purification. Anhydrous ferric nitrate (Fe(NO₃)₃), Anhydrous citric acid (C₆H₈O₇) were purchased from Merck (India) with a purity \geq 98 %, whereas epoxy resin and diethylene triamine (DETA) hardener were purchased from Sigma-Aldrich (India).

2.2 Synthesis of α -Fe₂O₃ Nanoparticles

Hematite (α -Fe₂O₃) nanoparticles were chemically synthesized by sol-gel process, where 200 mL (0.1M) of anhydrous ferric nitrate, Fe(NO₃)₃ used as a precursor solution which gelled by using 800 mL (0.1M) of anhydrous citric acid, C₆H₈O₇ solution as ligand molecules, and singly distilled water as the solvent. Ferric nitrate solution drop-wise added to the citric acid solution with maintaining vigorous stirring by magnetic stirrer. The mixture was heated to 70 °C and continuous stirring was maintained until the gel formation. The produced gel was then dried by evaporation. After that, the dried gel was annealed at 250 °C for 1.5 hours. Finally, the powder was grinding by mortar and pestle, typically yielding 0.85gm of α -Fe₂O₃ nanoparticles.

2.3 Fabrication of α -Fe₂O₃/Epoxy Nanocomposites

In order to fabricate the nanocomposites, a certain amount of α -Fe₂O₃ nanoparticles was added into epoxy resin and mixed carefully for 15 minutes to get a uniform dispersion of the nanoparticles within the resin. After that, the curing agent diethylene triamine (DETA) was added with continuous stirring (epoxy-curing agent ratio was 10:1 by weight). Finally, the above mixture was cast into a flat glass mold and out-gassed overnight. The produced composite sheets had an approximate thickness of 2 mm. Due to their high aspect ratio and large surface area, the contents of the α -Fe₂O₃ nanoparticles in the composite were chosen to be 0.5, 1.0, 2.5, and 5.0 wt% respectively.

2.4 Characterization Techniques

2.4.1 X-Ray Diffraction (XRD)

The XRD patterns of α -Fe₂O₃ nanoparticles were obtained using a BRUKAR ADVANCE D8 Diffractometer. The diffraction patterns were measured at room temperature using Cu

K α radiation ($\lambda = 1.5406 \text{ \AA}$) where Bragg's angles varying from 10° to 70°.

2.4.2 Scanning Electron Microscopy (SEM)

The morphologies and microstructures of α -Fe₂O₃ nanoparticles were observed using JEOLUSER 7610F Scanning Electron Microscope, which operated at 5 kV.

2.4.3 Fourier-Transform Infrared Spectroscopy (FTIR)

The presence of different functional groups in α -Fe₂O₃ nanoparticles, neat epoxy and α -Fe₂O₃/epoxy nanocomposites were observed using PERKIN-ELMER FRONTIER FTIR/MIR Spectrometer. The FTIR spectra were recorded in the 450-4000 cm⁻¹ region.

2.4.4 Vibrating Sample Magnetometer (VSM)

The magnetization-magnetic field hysteresis loops of α -Fe₂O₃ nanoparticles were measured by using *MICROSENSE EV9 Vibrating Sample Magnetometer* at room temperature.

2.4.5 Tension and Flexural testing

The tensile tests of neat epoxy and α -Fe₂O₃/epoxy nanocomposites were conducted according to ASTM D882 (2012) using a Universal Testing Machine (Hounsfield UTM 10KN, UK). The clamping length for each specimen on each jaw was 15 mm, and no extensometer was used for the tensile tests. The tests were performed at a crosshead speed of 5 mm/min. Each value reported is the average of five sample tests. The flexural strength of neat epoxy and α -Fe₂O₃/epoxy nanocomposites were measured using HOUNSFIELD H10KN UTM according to the standard method used for flexural properties (ASTM D790-98 2003). The speed for the flexural test was set at 5 mm/min. In addition, each value reported is the average of five sample tests.

2.4.6 Hardness Testing

The hardness of neat epoxy and α -Fe₂O₃/epoxy nanocomposites were measured using SHIMADZU HVM-2 VICKER'S Micro-Hardness Tester. The specimen was placed on a hard, horizontal glass surface. The diamond indenter was held vertically and the scale was measured with 10 seconds, after the pressure was in firm contact with the specimen. Each sample was investigated five times at a certain load with 10 s indentation time.

2.4.7 Thermogravimetric Analysis (TGA)

The TGA curves of α -Fe₂O₃ nanoparticles, neat epoxy and α -Fe₂O₃/epoxy nanocomposites were determined using EXSTAR 6000, TG/DTA 6300 Thermal Analyzer. The rate of heating was 20 °C/min and the mass of the specimen was 2-3 mg. The measurements were carried out in nitrogen atmosphere.

2.4.8 UV-Vis Spectroscopy

The optical absorption of neat epoxy and α -Fe₂O₃/epoxy nanocomposites were recorded at room temperature using SHIMADZU UV-1601 Spectrophotometer in the range of 190-1100 nm.

2.4.9 DC Resistivity

The DC resistivity of neat epoxy and α -Fe₂O₃/epoxy nanocomposites were determined using KEITHLEY 6517B Electrometer at room temperature where the applied voltages were 10, 20, 30, 40, 50 volts, respectively for every sample.

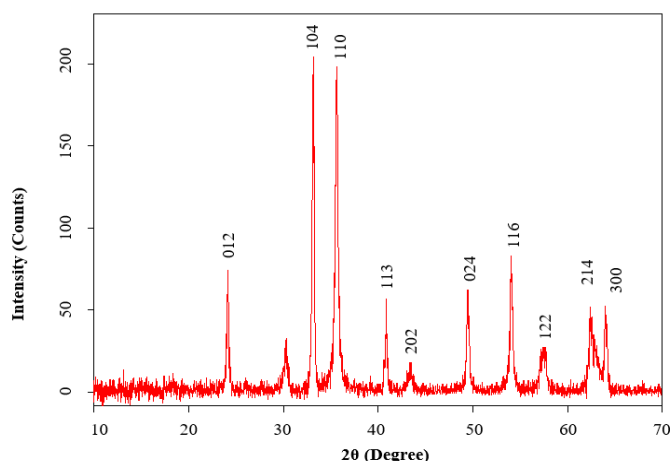


Fig. 1 XRD patterns of α -Fe₂O₃ nanoparticles

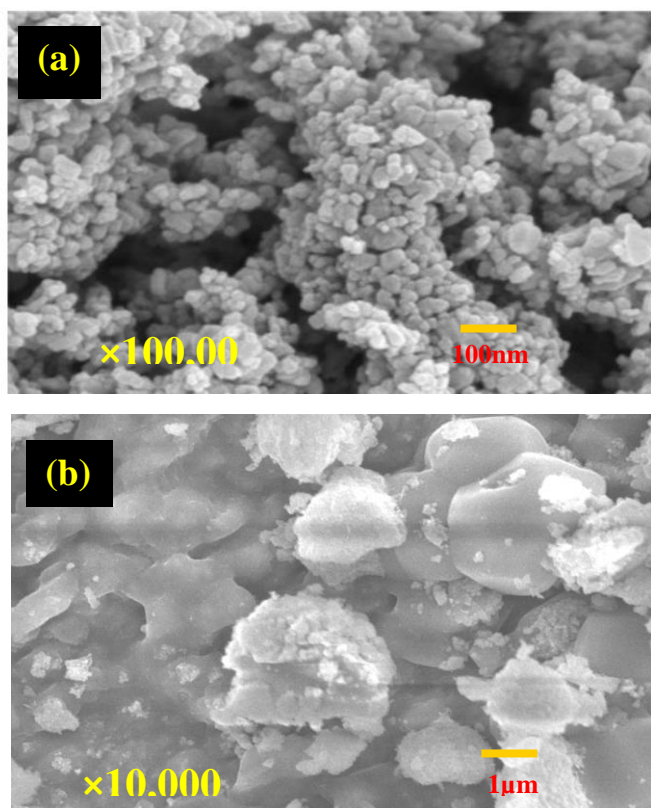


Fig. 2 SEM images of (a) α -Fe₂O₃ nanoparticles and (b) α -Fe₂O₃/Epoxy nanocomposite.

3 Results and Discussion

3.1 XRD Analysis

The XRD patterns of α -Fe₂O₃ nanoparticles produced by the sol-gel process were illustrated in Fig. 1. The XRD peaks were recorded with the 2θ value varying from 10° to 70° with Cu K α radiation ($\lambda=1.5406\text{\AA}$). The XRD patterns of α -Fe₂O₃ were indexed as pure hexagonal structures. The peaks were appeared at 2θ values of 24.118° , 33.2432° , 35.6757° , 40.89° , 43.41° , 49.47° , 54.069° , 57.46° , 62.327° , and 64.0° and represented by the (012), (104), (110), (113), (202), (024), (116), (122), (214) and (300) crystalline structures correspond to pure α -Fe₂O₃ nanoparticles. The diffraction peaks matched with standard JCPDS card no. 87-1164 [35], indicating that the α -Fe₂O₃

nanoparticles are crystalline structures. The average crystallite sizes were calculated by using the Debye-Scherrer equation:

$$D = \frac{K\lambda}{\beta \cos\theta}$$

where K is the shape factor (the typical value is 0.94), λ is the wavelength of the incident beam, β is the broadening of the diffraction line measured in radians at half of its maximum intensity (FWHM) and θ is the Bragg's angle and D is the diameter of the crystallite size [36]. The average crystallite sizes of α -Fe₂O₃ from the XRD data were found to be around 32 nm. No other peaks were observed in the calcined compound, which indicates the formation of a pure hexagonal structure of α -Fe₂O₃ nanoparticles.

3.2 SEM Analysis

The SEM images of α -Fe₂O₃ nanoparticles and α -Fe₂O₃/epoxy nanocomposites are illustrated in Fig. 2(a) and (b), with $\times 100,000$ and $\times 10,000$ magnification, respectively. Fig. 2(a) shows α -Fe₂O₃ nanoparticles are well defined and oriented spindle-like with small spherical shaped particles. The average crystallite size of α -Fe₂O₃ which was calculated from the SEM image was found to be around 29 nm. From Fig. 2(a), it is clear that α -Fe₂O₃ nanoparticles are mainly present as granules with small spherical-shaped particles and are well crystalline.

Due to the very tiny particle size, the number of existing atoms/molecules on the surface was increased excessively. Therefore, the agglomeration of nanoparticles was seen due to the presence of inter-particle forces such as electrostatic forces, van der Waals forces.

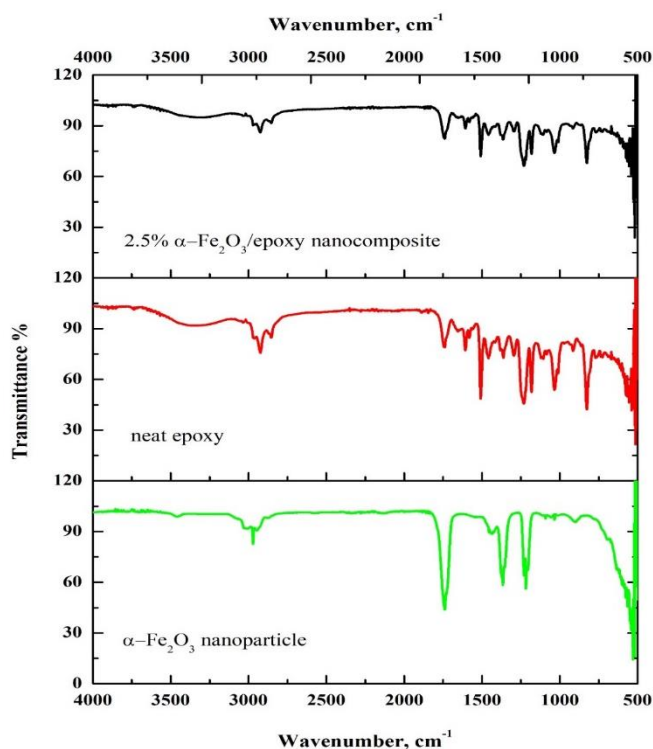


Fig. 3 FTIR spectrum of α -Fe₂O₃ nanoparticles, neat epoxy and 2.5% α -Fe₂O₃/epoxy nanocomposite

During the synthesis and process of nanoparticles this agglomeration commonly occurs [34]. From Fig. 2(b), it is seen that the α -Fe₂O₃ nanoparticles are more or less uniformly confined in the epoxy matrix. The inclusion of nano-sized particles impart new properties compared to polymer matrix

itself. The mechanical properties of composites either positively or negatively influences by the size of nanoparticles [35].

In composite systems, it is found that the mechanical properties such as strength, rigidity and yield strength varies with the size of incorporated particles [35].

3.3 FTIR Analysis

Fig. 3 shows the FTIR spectra of α -Fe₂O₃ nanoparticles, neat epoxy, and 2.5% α -Fe₂O₃/epoxy nanocomposite. For α -Fe₂O₃ nanoparticles, the band at 3466 cm⁻¹ is assigned to the stretching vibration of water, indicating the existence of a little water absorbed on the sample. The high-frequency band at 544 cm⁻¹ refers to Fe-O deformation in the octahedral and tetrahedral sites which gives evidence for the formation of α -Fe₂O₃.

There is no peak at 2900 cm⁻¹ indicating the C-H stretching band, which means all organic compounds are removed from the samples after calcination at 250 °C. For neat epoxy, the O-H, C-H, C=O, C=C, C=N, and C-O stretching vibration peaks are located at 3370, 2926, 1748, 1510, 1238, and 1037 cm⁻¹, respectively. The C-H bending vibration peak is located at 1366 cm⁻¹. For 2.5% α -Fe₂O₃/epoxy nanocomposite, the O-H, C-H, C=O, C=C, C-N, and C-O stretching vibration peaks are located at 3328, 2933, 1749, 1509, 1234, and 1039 cm⁻¹, respectively. The C-H bending vibration peak is located at 1371 cm⁻¹.

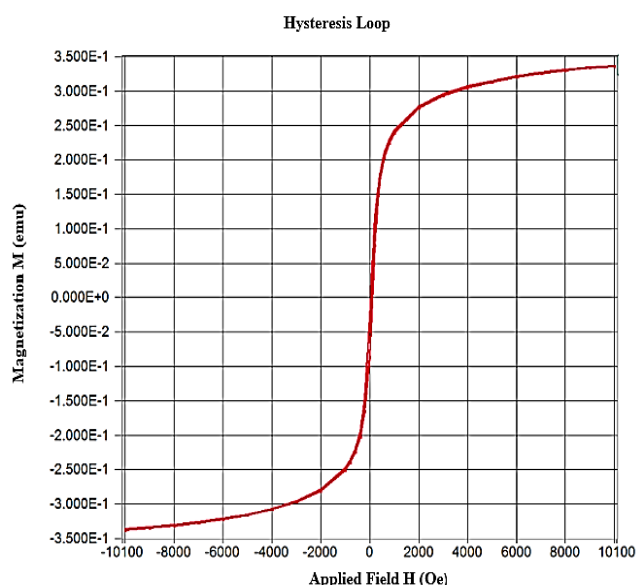


Fig. 4 Magnetization-magnetic field hysteresis curve of α -Fe₂O₃ nanoparticles.

3.4 VSM Analysis

The magnetic properties of α -Fe₂O₃ nanoparticles were measured by a vibrating sample magnetometer. Fig. 4 illustrates the magnetic hysteresis curve of α -Fe₂O₃ nanoparticles recorded at room temperature. It exhibits superparamagnetic behavior due to nanoscale particle size. The saturation magnetization (M_s), coercivity (H_c), and remnant magnetization (M_r) of α -Fe₂O₃ nanoparticles were 337.137×10^{-3} emu, 33.312 Oe, and 28.90×10^{-3} emu, respectively. It should be mentioned that the magnetic properties of the materials depend on the particle's size, shape, magnetization direction, crystallinity, etc.

3.5 Tensile Properties Analysis

Fig. 5 represents the stress-strain curves of neat epoxy, 0.5, 1.0, 2.5, and 5.0 wt% of α -Fe₂O₃/epoxy nanocomposites. Epoxy

is a brittle material because it fails in tension at relatively low values of strain. In Fig. 5, the stress-strain curves which remain straight initially represent the elastic region, where the stress and strain are directly proportional. The elastic modulus of the material was measured from the slope of 0.1 to 0.25% tensile strain. Fig. 6 demonstrates the measured tensile properties of α -Fe₂O₃/epoxy nanocomposites. It can be seen that the presence of α -Fe₂O₃ nanoparticles enhanced the tensile stress-strain behavior of the epoxy polymer. Nanocomposites show higher tensile modulus. The increase in modulus is expected because the modulus of α -Fe₂O₃ nanoparticles is about 359 GPa.

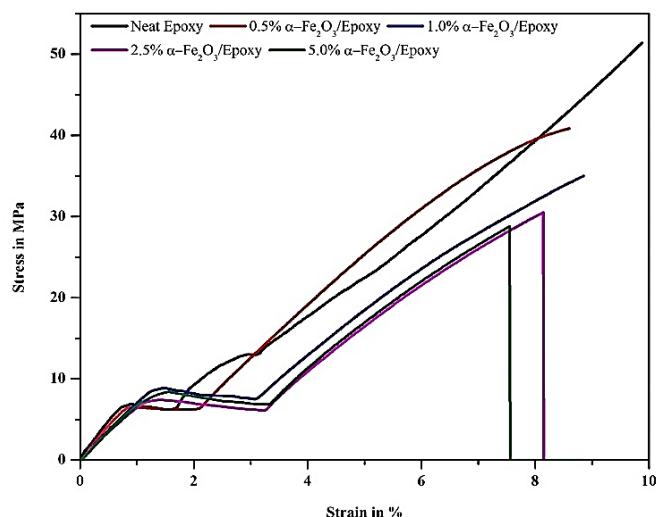


Fig. 5 Stress-strain curve of α -Fe₂O₃/epoxy nanocomposites.

The incorporation of α -Fe₂O₃ nanoparticles into epoxy matrix decreased the tensile strength of the nanocomposites because epoxy resin and α -Fe₂O₃ nanoparticles both are brittle materials. Sometimes, agglomeration of nanoparticles inside the polymer matrices becomes responsible for decreasing the tensile strength. This implies that the interfacial bonding between matrix and particle is not strong enough to bear large mechanical stress, as because of inhomogeneous dispersion of nanoparticles. The presence of highly stiff α -Fe₂O₃ nanoparticles in the polymer matrix is responsible for lowering the elastic modulus and elongation of the polymer [37].

Table 1 Flexural properties of neat epoxy and α -Fe₂O₃/epoxy nanocomposites

Materials	Flexural Strength (MPa)	Strain at Break (%)	Energy (Joule)
Neat epoxy	84.50	1.735	0.0601
0.5% α -Fe ₂ O ₃ /epoxy	76.50	2.127	0.0633
1.0% α -Fe ₂ O ₃ /epoxy	64.50	2.279	0.0338
2.5% α -Fe ₂ O ₃ /epoxy	59.30	1.563	0.0236
5.0% α -Fe ₂ O ₃ /epoxy	53.00	1.850	0.0293

3.6 Flexural Properties Analysis

The three-point flexural test was carried out to determine the flexural properties of α -Fe₂O₃/epoxy nanocomposites, whose force-extension curves are shown in Fig. 7. The neat epoxy, 0.5, 1.0, 2.5, and 5.0 wt% of α -Fe₂O₃/epoxy nanocomposites exhibit

84.5, 76.5, 64.5, 59.3 and 53.0 MPa flexural strength with 1.735, 2.127, 2.279, 1.563 and 1.850% strain at break, respectively which are illustrated in Table 1. From Table 1 we can see that, the addition of α -Fe₂O₃ nanoparticles into the epoxy matrix gradually reduced the flexural strength of the nanocomposites, the reason is due to the compressive characteristics of epoxy resin and α -Fe₂O₃ nanoparticles. The addition of filler is not much effective in flexural characteristics of the matrix but it may increase in the case of laminates with filler matrix [38].

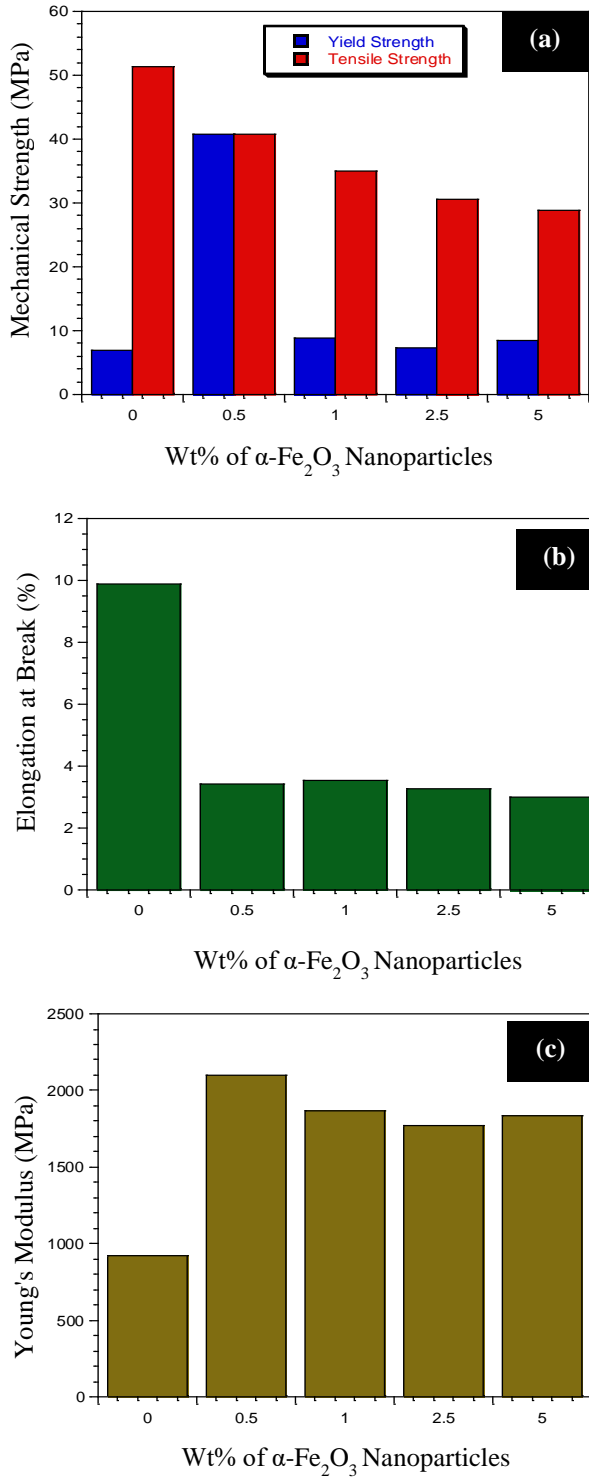


Fig. 6 Effect of different nanoparticles addition on (a) Mechanical Strength (b) Elongation, and (c) Young's modulus in epoxy polymer matrix.

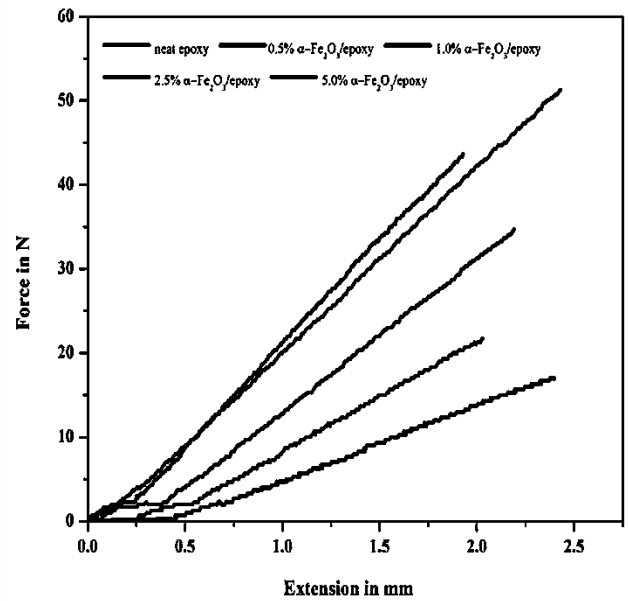


Fig. 7 Force-extension curves of α -Fe₂O₃/epoxy nanocomposites

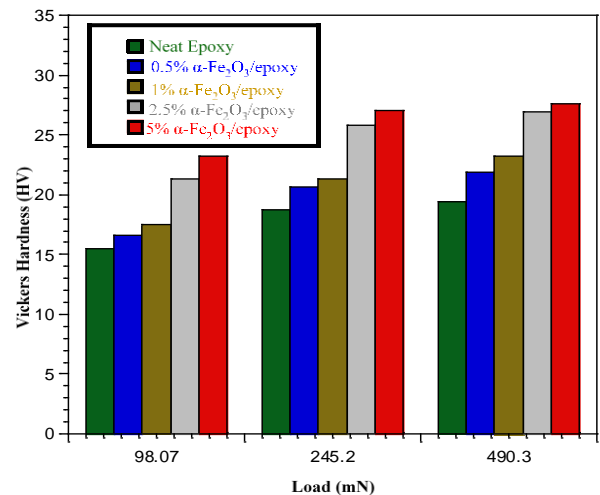


Fig. 8 Vickers hardness number of neat epoxy and α -Fe₂O₃/epoxy nanocomposites.

3.7 Hardness Analysis

Hardness is the ability of a material to resist plastic deformation, usually by penetration. However, it may also refer to the resistance to bending, scratching, abrasion or cutting. The hardness of neat epoxy, 0.5, 1.0, 2.5, and 5.0 wt% of α -Fe₂O₃/epoxy nanocomposites was measured by Vickers's micro-hardness tester. These tests were performed at three different loads 98.07, 245.2, and 490.3 mN, respectively, and the results are shown in Fig. 8. The measured values of hardness increased considerably for α -Fe₂O₃/epoxy nanocomposites due to the addition of stiff nanoparticles in the polymer matrix. The successful interaction between nanoparticles and polymer matrix helped to transfer the applied load from matrix to nanoparticles. Thus, the applied load became suppressed by the stiff nanoparticles and the hardness value increased in the composites compared to that of the neat epoxy matrix. In addition incorporation of α -Fe₂O₃ nanoparticles into epoxy resist the movement of dislocation within the structure of the epoxy matrix, increases hardness.

3.8 TG Analysis

Fig. 9 shows the TG curve of α -Fe₂O₃ nanoparticles, neat epoxy, and 5.0% α -Fe₂O₃/epoxy nanocomposite, respectively. The decomposition process consists of three regions. They were 20-300 °C, 300-500 °C, and 500-600 °C, respectively. The first weight loss indicates the evaporation of absorbed water due to the initial breakdown of the complex and spontaneous combustion. H₂O and CO₂ provide an oxidizing environment for the combustion of the organic components [39], citrate ions in the gel cause spontaneous combustion. The second weight-loss indicates the dehydration of the O-H group in the α -Fe₂O₃ structure and epoxy that lead to two degradation systems involving both inter and intra-molecular transfer reaction, the oxidation of complexes, and formation of semi-organic carbon metal/metal oxide [40]-[42].

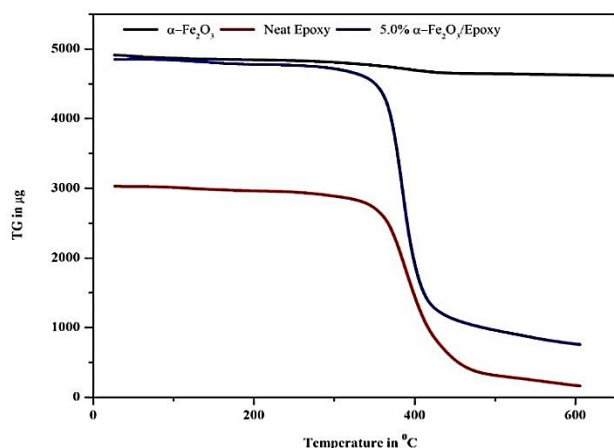


Fig. 9 TGA curve of α -Fe₂O₃ nanoparticles, neat epoxy and 5.0% α -Fe₂O₃/epoxy nanocomposite

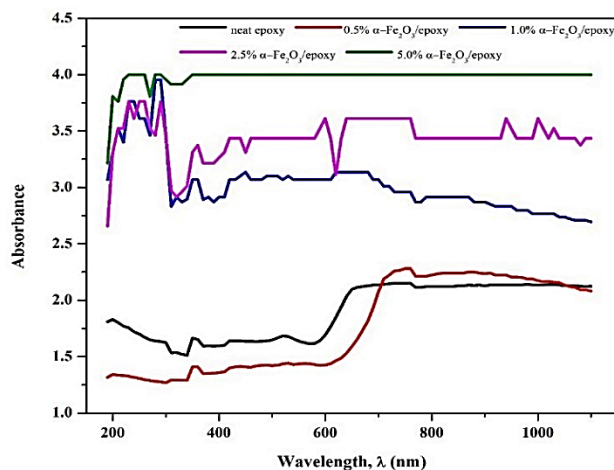


Fig. 10 Absorbance vs wavelength curve of α -Fe₂O₃/epoxy nanocomposites

The third weight loss indicates the formation of the corresponding metal oxide phase. Above 600 °C there is no weight loss i.e. the TGA curve is steady, exhibiting the absolute volatility of water, organic compounds, citrates in the composites, the completion of crystallization route, and the immediate formation of pure materials.

3.9 UV-Vis Spectroscopy Analysis

UV-Vis spectroscopy is used to determine the optical band gap energy of crystalline and amorphous materials. In this method, electron excitation from the valance band to the conduction band, is used to verify the character and value of the optical band gap. UV-visible spectra of fabricated specimens were measured in the 190-1100 nm range, (Fig. 10). The spectrum of neat epoxy shows a single absorption peak at 526 nm, which represents the polaron/bipolaron transition. On the other hand, spectra of α -Fe₂O₃/epoxy nanocomposites show several peaks within the entire range in shells increase the absorption cross-section of the nanocomposite and thus enhance plasma-exciton interactions [43]-[45]. The optical band gap is determined using the following relationship [46]:

$$ahv^{\frac{1}{n}} = A(hv - E_g) \quad (1)$$

For direct band gap materials this equation becomes-

$$ahv = A(hv - E_g)^2 \quad (2)$$

where α is the absorption coefficient, A is a constant, E_g is the optical band gap of the material and the exponent n depends on the nature of electronic transition, it is equal to 1/2 for direct allowed, 3/2 for direct forbidden transitions, and 2 for indirect allowed transition. An extrapolation of the linear region of a plot of the graph of $(\alpha hv)^2$ on the y-axis versus photon energy (hv) on the x-axis, gives the value of the optical band gap, E_g [47]. The optical band gap is calculated and shown in Fig. 11. From Fig. 10, we can see that, the absorbance of α -Fe₂O₃/epoxy nanocomposites increased with increasing the α -Fe₂O₃ content. The increased light absorption phenomena can be attributed to the well dispersion and successful interaction of nanoparticles inside the polymer matrix.

Conversely, from Fig. 11, we can see that, the optical band gap of neat epoxy, 0.5, 1.0, 2.5, and 5.0 wt% of α -Fe₂O₃/epoxy nanocomposites were 3.2, 2.8, 2.4, 1.8, and 1.4 eV, respectively. This decrease of E_g can be attributed to the formation of complex due to interaction between nanoparticles and polymer matrix. In addition, the increase of density of defects i.e. particle clusters leads to the expansion of valance band inside the forbidden gap of polymeric system. Therefore, band tailing occurred and as a consequence shrinkage of E_g was happened [48].

3.10 DC Resistivity Analysis

Fig. 12 shows the I-V curves of neat epoxy, 0.5, 1.0, 2.5 and 5.0 wt% of α -Fe₂O₃/epoxy nanocomposites, where all the tests were performed at room temperature. This figure indicates that 5.0 % α -Fe₂O₃ nanoparticles containing epoxy nanocomposite have the higher value of dc current, I (about 27.342 nA) at 50 volts, whereas neat epoxy shows the minimum value of dc current, I (about 18.741 pA) at 10 volts. On the other hand, Fig. 13 shows the variation of measured dc resistivity (ρ) of neat epoxy, 0.5, 1.0, 2.5 and 5.0 wt% of α -Fe₂O₃/epoxy nanocomposites. This figure illustrates that neat epoxy exhibits the highest value of dc resistivity, ρ (about 3.017 T Ω mm) because epoxy is an excellent electrically insulating material, whereas 2.5% α -Fe₂O₃/epoxy nanocomposite exhibits the lowest value of dc resistivity, ρ (about 0.923 T Ω mm).

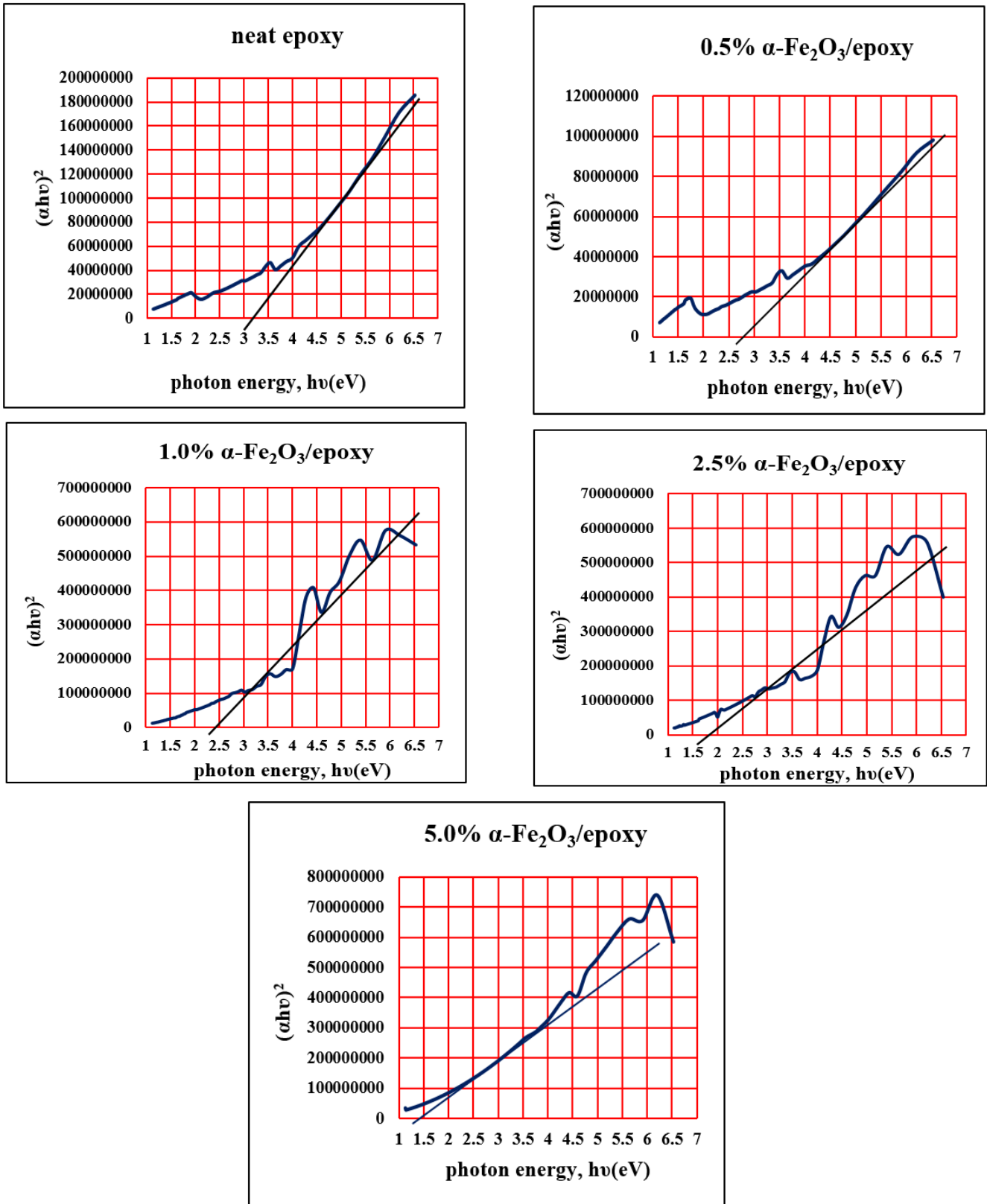


Fig. 11 Optical band gap of α - Fe_2O_3 /epoxy nanocomposites

By increasing the α - Fe_2O_3 content into epoxy, the dc resistivity of the nanocomposite sheets decreased gradually due to the formation of polarons in the both epoxy and α - Fe_2O_3 molecules after applying voltage [49]. By increasing α - Fe_2O_3

content, the dc resistivity changes slightly, which attributed to saturation of charge carriers.

However, 1.0% α - Fe_2O_3 /epoxy nanocomposite exhibited a little inconsistency of dc resistivity may be due to the non-

uniform dispersion and agglomeration of α -Fe₂O₃ nanoparticles into the epoxy matrix. Moreover, this happened due to the dispersion of higher amount of nanoparticles than the critical volume fraction in the polymer matrix.

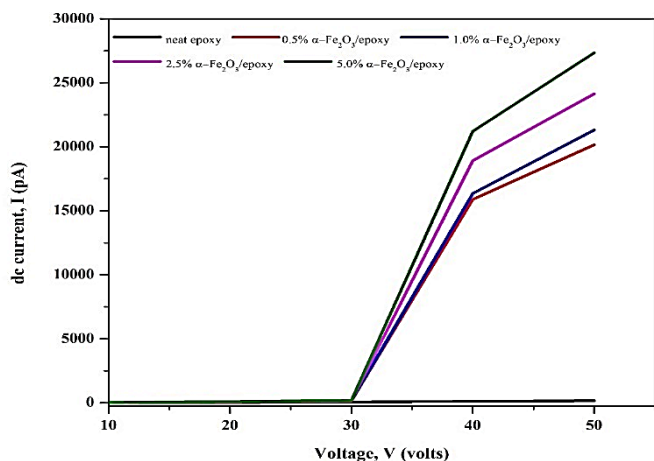


Fig. 12 I-V curves of α -Fe₂O₃/epoxy nanocomposites

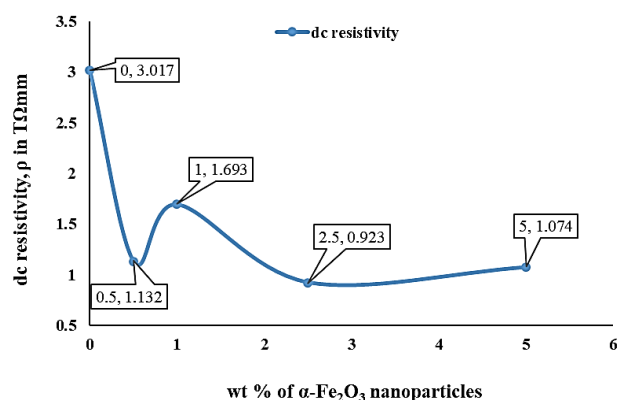


Fig. 13 Effect of α -Fe₂O₃ nanoparticles on the dc resistivity of α -Fe₂O₃/epoxy nanocomposites

4 Conclusions

In this study, we synthesized α -Fe₂O₃ nanoparticles by sol-gel process which further dispersed into the epoxy matrix to fabricate nanocomposites. The chemical, mechanical, electrical, optical and thermal properties of the fabricated polymer nanocomposites were evaluated. The XRD and SEM confirmed the formation of nanoparticles. FTIR analysis ensured the presence of different functional groups into the nanomaterials. Using VSM measurement, the saturation magnetization (M_s), coercivity (H_c) and remnant magnetization (M_r) of α -Fe₂O₃ nanoparticles were found to be 337.137×10^{-3} emu, 33.312 Oe and 28.90×10^{-3} emu, respectively. Incorporation of α -Fe₂O₃ nanoparticles into epoxy matrix gradually decreased tensile strength, elongation, flexural strength, optical band gap energy and dc resistivity of α -Fe₂O₃/epoxy nanocomposites, however, increased the young modulus, surface hardness and thermal stability of α -Fe₂O₃/epoxy nanocomposites. The fabricated nanocomposites can be used to produce various products in medical, construction, automotive, etc. sectors with better properties based on the obtained results.

References

- [1] Huynh, W.U., Dittmer, J.J. and Alivisatos, A.P., 2002. Hybrid nanorod-polymer solar cells. *Science*, 295(5564), pp.2425-2427.
- [2] Lu, Y., Yang, Y., Sellinger, A., Lu, M., Huang, J., Fan, H., Haddad, R., Lopez, G., Burns, A.R., Sasaki, D.Y. and Shelnut, J., 2001. Self-assembly of mesoscopically ordered chromatic polydiacetylene/silica nanocomposites. *Nature*, 410(6831), pp.913-917.
- [3] Wang, G.F., Tao, X.M. and Wang, R.X., 2008. Flexible organic light-emitting diodes with a polymeric nanocomposite anode. *Nanotechnology*, 19(14), p.145201.
- [4] McDonald, S.A., Konstantatos, G., Zhang, S., Cyr, P.W., Klem, E.J., Levina, L. and Sargent, E.H., 2005. Solution-processed PbS quantum dot infrared photodetectors and photovoltaics. *Nature Materials*, 4(2), pp.138-142.
- [5] Podsiadlo, P., Kaushik, A.K., Arruda, E.M., Waas, A.M., Shim, B.S., Xu, J., Nandivada, H., Pumphlin, B.G., Lahann, J., Ramamoorthy, A. and Kotov, N.A., 2007. Ultrastrong and stiff layered polymer nanocomposites. *Science*, 318(5847), pp.80-83.
- [6] Wang, L., Yoon, M.H., Lu, G., Yang, Y., Facchetti, A. and Marks, T.J., 2006. High-performance transparent inorganic-organic hybrid thin-film n-type transistors. *Nature Materials*, 5(11), pp.893-900.
- [7] Shan, H., Liu, C., Liu, L., Li, S., Wang, L., Zhang, X., Bo, X. and Chi, X., 2013. Highly sensitive acetone sensors based on La-doped α -Fe₂O₃ nanotubes. *Sensors and Actuators B: Chemical*, 184, pp.243-247.
- [8] Sun, Y., Guo, G., Yang, B., Cai, W., Tian, Y., He, M. and Liu, Y., 2011. One-step solution synthesis of Fe₂O₃ nanoparticles at low temperature. *Physica B: Condensed Matter*, 406(4), pp.1013-1016.
- [9] Fang, X.L., Chen, C., Jin, M.S., Kuang, Q., Xie, Z.X., Xie, S.Y., Huang, R.B. and Zheng, L.S., 2009. Single-crystal-like hematite colloidal nanocrystal clusters: synthesis and applications in gas sensors, photocatalysis and water treatment. *Journal of Materials Chemistry*, 19(34), pp.6154-6160.
- [10] Gupta, A.K. and Gupta, M., 2005. Synthesis and surface engineering of iron oxide nanoparticles for biomedical applications. *Biomaterials*, 26(18), pp.3995-4021.
- [11] Mirzaei, A., Janghorban, K., Hashemi, B., Bonavita, A., Bonyani, M., Leonardi, S.G. and Neri, G., 2015. Synthesis, characterization and gas sensing properties of Ag@ α -Fe₂O₃ core-shell nanocomposites. *Nanomaterials*, 5(2), pp.737-749.
- [12] Neri, G., Bonavita, A., Galvagno, S., Siciliano, P. and Capone, S., 2002. CO and NO₂ sensing properties of doped-Fe₂O₃ thin films prepared by LPD. *Sensors and Actuators B: Chemical*, 82(1), pp.40-47.
- [13] Mitra, S., Das, S., Mandal, K. and Chaudhuri, S., 2007. Synthesis of a α -Fe₂O₃ nanocrystal in its different morphological attributes: growth mechanism, optical and magnetic properties. *Nanotechnology*, 18(27), p.275608.
- [14] Fan, Z., Wen, X., Yang, S. and Lu, J.G., 2005. Controlled p-and n-type doping of Fe₂O₃ nanobelt field effect transistors. *Applied Physics Letters*, 87(1), p.013113.
- [15] Wagloehner, S., Reichert, D., Leon-Sorzano, D., Balle, P., Geiger, B. and Kureti, S., 2008. Kinetic modeling of the oxidation of CO on Fe₂O₃ catalyst in excess of O₂. *Journal of Catalysis*, 260(2), pp.305-314.
- [16] Pailhé, N., Wattiaux, A., Gaudon, M. and Demourgues, A., 2008. Impact of structural features on pigment properties of α -Fe₂O₃ haematite. *Journal of Solid State Chemistry*, 181(10), pp.2697-2704.
- [17] Hu, C., Gao, Z. and Yang, X., 2007. Facile synthesis of single crystalline α -Fe₂O₃ ellipsoidal nanoparticles and its catalytic performance for removal of carbon monoxide. *Materials Chemistry and Physics*, 104(2-3), pp.429-433.
- [18] Eivari, H.A. and Rahdar, A., 2013. Some properties of iron oxide nanoparticles synthesized in different conditions. *World Appl. Program*, 3(2), pp.52-55.

- [19] Bandgar, D.K., Navale, S.T., Khuspe, G.D., Pawar, S.A., Mulik, R.N. and Patil, V.B., 2014. Novel route for fabrication of nanostructured α -Fe₂O₃ gas sensor. *Materials Science in Semiconductor Processing*, 17, pp.67-73.
- [20] Ramesh, R., Ashok, K., Bhalero, G.M., Ponnusamy, S. and Muthamizhchelvan, C., 2010. Synthesis and properties of α -Fe₂O₃ nanorods. *Crystal Research and Technology*, 45(9), pp.965-968.
- [21] Yan, H., Su, X., Yang, C., Wang, J. and Niu, C., 2014. Improved photocatalytic and gas sensing properties of α -Fe₂O₃ nanoparticles derived from β -FeOOH nanospindles. *Ceramics International*, 40(1), pp.1729-1733.
- [22] Mahmoud, M.H., Hamdeh, H.H., Ho, J.C., O'shea, M.J. and Walker, J.C., 2000. Mössbauer studies of manganese ferrite fine particles processed by ball-milling. *Journal of Magnetism and Magnetic Materials*, 220(2-3), pp.139-146.
- [23] Shinde, S.S., Moholkar, A.V., Kim, J.H. and Rajpure, K.Y., 2011. Structural, morphological, luminescent and electronic properties of sprayed aluminium incorporated iron oxide thin films. *Surface and Coatings Technology*, 205(12), pp.3567-3577.
- [24] Dudić, D., Marinović-Cincović, M., Nedeljković, J.M. and Djoković, V., 2008. Electrical properties of a composite comprising epoxy resin and α -hematite nanorods. *Polymer*, 49(18), pp.4000-4008.
- [25] Prasanna, B.P., Avadhani, D.N., Raghu, M.S. and Kumar, Y., 2017. Synthesis of polyaniline/ α -Fe₂O₃ nanocomposite electrode material for supercapacitor applications. *Materials Today Communications*, 12, pp.72-78.
- [26] Mirzaei, A., Janghorban, K., Hashemi, B., Hosseini, S.R., Bonyani, M., Leonardi, S.G., Bonavita, A. and Neri, G., 2016. Synthesis and characterization of mesoporous α -Fe₂O₃ nanoparticles and investigation of electrical properties of fabricated thick films. *Processing and Application of Ceramics*, 10(4), pp.209-217.
- [27] Tang, C. and Liu, W., 2010. Preparation of dual-curable polysiloxane and the properties of its cured films with epoxy resin. *Journal of Plastic Film & Sheeting*, 26(3), pp.241-257.
- [28] Voo, R., Mariatti, M. and Sim, L.C., 2011. Properties of epoxy nanocomposite thin films prepared by spin coating technique. *Journal of Plastic Film & Sheeting*, 27(4), pp.331-346.
- [29] Kanapitsas, A., Tsonos, C., Psarras, G.C. and Kriptou, S., 2016. Barium ferrite/epoxy resin nanocomposite system: Fabrication, dielectric, magnetic and hydration studies. *Express Polymer Letters*, 10(3), p.227.
- [30] Gazderazi, M. and Jamshidi, M., 2016. Hybridizing MWCNT with nano metal oxides and TiO₂ in epoxy composites: Influence on mechanical and thermal performances. *Journal of Applied Polymer Science*, 133(34).
- [31] Bhadra, S., Khastgir, D., Singha, N.K. and Lee, J.H., 2009. Progress in preparation, processing and applications of polyaniline. *Progress in Polymer Science*, 34(8), pp.783-810.
- [32] Katsoulis, C., Kandare, E. and Kandola, B.K., 2011. The effect of nanoparticles on structural morphology, thermal and flammability properties of two epoxy resins with different functionalities. *Polymer Degradation and Stability*, 96(4), pp.529-540.
- [33] Wang, Z., Volinsky, A.A. and Gallant, N.D., 2014. Crosslinking effect on polydimethylsiloxane elastic modulus measured by custom-built compression instrument. *Journal of Applied Polymer Science*, 131(22).
- [34] Mohammadzadehmoghadam, S., Dong, Y. and Jeffery Davies, I., 2015. Recent progress in electrospun nanofibers: reinforcement effect and mechanical performance. *Journal of Polymer Science Part B: Polymer Physics*, 53(17), pp.1171-1212.
- [35] Bagheri, S., Chandrappa, K. and Hamid, S.B.A., 2013. Generation of hematite nanoparticles via sol-gel method. *Research Journal of Chemical Sciences*, 3(7), pp.62-68.
- [36] He, C., Sasaki, T., Shimizu, Y. and Koshizaki, N., 2008. Synthesis of ZnO nanoparticles using nanosecond pulsed laser ablation in aqueous media and their self-assembly towards spindle-like ZnO aggregates. *Applied Surface Science*, 254(7), pp.2196-2202.
- [37] Chicot, D., Mendoza, J., Zaoui, A., Louis, G., Lepingle, V., Roudet, F. and Lesage, J., 2011. Mechanical properties of magnetite (Fe₃O₄), hematite (α -Fe₂O₃) and goethite (α -FeO·OH) by instrumented indentation and molecular dynamics analysis. *Materials Chemistry and Physics*, 129(3), pp.862-870.
- [38] Siva Sankari, S., Murugan, N., Sivaraj, S., 2014. Effect of Filler Materials on the Mechanical and Thermal Properties of Epoxy Resin. *AMM* 592–594, 206–210.
- [39] Guo, L., Shen, X., Meng, X. and Feng, Y., 2010. Effect of Sm³⁺ ions doping on structure and magnetic properties of nanocrystalline NiFe₂O₄ fibers. *Journal of Alloys and Compounds*, 490(1-2), pp.301-306.
- [40] Wang, Z., Liu, X., Lv, M., Chai, P., Liu, Y. and Meng, J., 2008. Preparation of ferrite MFe₂O₄ (M= Co, Ni) ribbons with nanoporous structure and their magnetic properties. *The Journal of Physical Chemistry B*, 112(36), pp.11292-11297.
- [41] Sivakumar, P., Ramesh, R., Ramanand, A., Ponnusamy, S. and Muthamizhchelvan, C., 2011. Synthesis and characterization of NiFe₂O₄ nanosheet via polymer assisted co-precipitation method. *Materials Letters*, 65(3), pp.483-485.
- [42] Zhang, C.Y., Shen, X.Q., Zhou, J.X., Jing, M.X. and Cao, K., 2007. Preparation of spinel ferrite NiFe₂O₄ fibres by organic gel-thermal decomposition process. *Journal of Sol-gel Science and Technology*, 42(1), pp.95-100.
- [43] Rand, B.P., Peumans, P. and Forrest, S.R., 2004. Long-range absorption enhancement in organic tandem thin-film solar cells containing silver nanoclusters. *Journal of Applied Physics*, 96(12), pp.7519-7526.
- [44] Schaadt, D.M., Feng, B. and Yu, E.T., 2005. Enhanced semiconductor optical absorption via surface plasmon excitation in metal nanoparticles. *Applied Physics Letters*, 86(6), p.063106.
- [45] Morfa, A.J., Rowlen, K.L., Reilly III, T.H., Romero, M.J. and van de Lagemaat, J., 2008. Plasmon-enhanced solar energy conversion in organic bulk heterojunction photovoltaics. *Applied Physics Letters*, 92(1), p.013504.
- [46] Jestl, M., Maran, I., Köck, A., Beinstingl, W. and Gornik, E., 1989. Polarization-sensitive surface plasmon Schottky detectors. *Optics letters*, 14(14), pp.719-721.
- [47] Ogwu, A.A., Darma, T.H. and Bouquerel, E., 2007. Electrical resistivity of copper oxide thin films prepared by reactive magnetron sputtering. *Journal of Achievements in Materials and Manufacturing Engineering*, 24(1), pp.172-177.
- [48] Praveena, S.D., Ravindrachary, V. and Bhajantri, R.F., 2016. Dopant-induced microstructural, optical, and electrical properties of TiO₂/PVA composite. *Polymer Composites*, 37(4), pp.987-997.
- [49] Khairy, M., 2014. Synthesis, characterization, magnetic and electrical properties of polyaniline/NiFe₂O₄ nanocomposite. *Synthetic metals*, 189, pp.34-41.

Production and Characterization of Biodiesel from Avocado Peel Oils using Experimental Analysis (ANOVA)

Tafere Aga Bullo^{1*} and Feyissa Bekele Fana²

¹Department of Chemical Engineering, Faculty of Engineering, Jimma University, Jimma Institute of Technology, Ethiopia

²Department of Chemical Engineering, Faculty of Engineering, Wollo University, Wollo Institute of Technology, Ethiopia

Received: May 04, 2021, Revised: June 22, 2021, Accepted: June 23, 2021, Available Online: June 28, 2021

ABSTRACT

The crisis of energy due to the increasing awareness of the depletion of fossil fuel resources, biodiesel is an alternative energy source and promising potential energy that grows rapidly, due to its high contribution to the environment friendly, renewable, non-toxicity, biodegradability, essentially sulfur-free, and as a strategical source of renewable energy in substitution to diesel oil and contributes a minimal amount of net greenhouse gases. In this study, the extracted oil used for biodiesel production from waste avocado peel was investigated in a laboratory approach. Experimental results evaluate the major optimum process parameters for base-catalyzed transesterification on biodiesel yield as well as its properties. The most important variables affecting methyl ester yield during the transesterification reaction are the molar ratio of alcohol to oil and the reaction temperature. A 95.2% FAME conversion was obtained using a methanol/oil ratio of 6:1, 1.21g NaOH, reaction time 67.5 min, and 60 °C reaction temperature. Important properties of (characterization) produced biodiesel are, (pHof 7.8, specific gravity of 0.88, density at 15 °C, kg/m³, the kinematic viscosity of biodiesel was found to be 4.22 m².s⁻¹ at 40 °C, the flashpoint was 161 °C and Cetane number of 49 are well-matched the relevant international standards for biodiesel quality produced. This result shows that the oil obtained from avocado peel can be used for biodiesel production as an alternative fuel as compared to those of ASTM and EN standards.

Keywords: Avocado Peel Oils, Biodiesel, Soxhlet Extraction, Transesterification.



This work is licensed under a [Creative Commons Attribution-Non Commercial 4.0 International License](https://creativecommons.org/licenses/by-nc/4.0/).

1 Introduction

Energy is one of the most important resources for humankind and its sustainable development. Today, the energy crisis becomes one of the global issues challenging. Fuels are of great importance because they can be burned to yield significant amounts of energy [1]. Biodiesel is the most promising renewable alternative fuel and the challenge of energy problem and sustainability in our today's world increases the number of population and sustainability have been problems due to the industrial revolution. Since it has considerable attention due to its renewability, reliable, secure, biodegradability, clean, environmental eco-friendly, nontoxicity, energy-efficient, less emission of gaseous and sustainable energy resources substitution of fulfilling energy security needs without sacrificing engine's operational performance thus it provides a feasible solution to the twin crises of fossil fuel depletion and environmental degradation [2]. It meets the currently increasing huge demands of world energy which is dependent on petroleum-based fuel resources. However, energy is often known as the primary success of a country's development. It is often used as an indicator to measure the level of economic growth in a country. The occurrence of oil depletion, global warming, and the greenhouse effect has become an alarming condition where it is needed to search for an alternative energy source [3].

Now a day the world has been stimulated with technological development to use vegetable-oil-derived fuel in a diesel engine. Biodiesel is nothing but, chemically treated triglycerides that is an alternative to petrodiesel. However, using vegetable oil to replace fuel caused the food versus fuel issue all over the world. So the idea of using waste vegetable oil (WVO) has been

introduced as an economical solution, which also gives a waste management solution [4].

The chemical process used to produce biodiesel is called transesterification. However, due to the high free fatty acid content of the cheaper non-edible feedstock conventional alkali-catalysed transesterification is not possible for biodiesel production. An acid pre-treatment is essential for converting the free fatty acid to corresponding methyl/ethyl ester followed by which usual transesterification is employed [5].

Base catalysed transesterification is the most commonly used technique as it is the most economical process base-catalysed involves stripping the glycerine from the fatty acids with a catalyst such as sodium or potassium hydroxide, and replacing it with anhydrous alcohol, usually methanol [6]. Biodiesel is a good alternative fuel for internal combustion engines is defined as a mixture of monoalkyl esters of long-chain fatty acids (FAME) derived from a renewable feedstock, such as vegetable oil or animal fat, are the most promising energy sources for our country [7].

Biodiesel is a renewable energy resource and biodegradable fuel to guarantee the sustainability of energy and produced from a wide range of naturally occurring fats and extract oils by a transesterification reaction process in which the triglycerides are broken down and fatty acid methyl esters (FAMES) are formed. The fatty acid dissemination of the original oil is reserved in the biodiesel; hence the physical and chemical properties of the biodiesel have some dependence on the feedstock used. Biodiesel is substitute energy for diesel engines that is produced by chemically reacting a vegetable oil or animal fat with an alcohol such as methanol through a transesterification reaction method.

Biodiesel is a carbon-free fuel because there is no overall increase in CO₂ in the atmosphere due to recycling by the growing plants used to feed the biodiesel industry. Emissions of CO₂, CO₃, CO, unburnt hydrocarbons, and particulate matter are lower than that of petroleum diesel [8].

Currently, the increasing rate of biodiesel is the key difficulty to commercialization. The increasing cost of biodiesel is mainly due to the cost of the feedstock used. One way of reducing the biodiesel costs is to use the less costly feedstock containing fatty acids such as inedible oils, waste cooking oil, and by-products of the refining vegetable oils [9]. However, using the waste avocado peels is one from this and its use as alternative raw materials.

1.1 Production of biodiesel and raw materials

Biodiesel is a substitute liquid fuel that can significantly replace conventional diesel and reduce exhaust pollution and engine maintenance costs. There are different types of feedstocks that are used for the production of biodiesel. These include palm seed oil, waste cooking vegetable oil, sunflower seed oil, cottonseed oil, jatropha seed oil, castor beans oil, and animal fats [10], [11]. The extracted oil from avocado peel is used for the manufacture of biodiesel through the process called transesterification reaction that is a process by which methanol alcohol reacts with the extracted oil in the presence of catalysts sodium hydroxide.

Avocado peel is a waste where so many people are throwing away after using the fruit flesh. Avocado fruit is one of the most popular fruit in Ethiopia as a result there is a significant rise in avocado fruit consumption and consequently an increase in avocado peel waste generation. currently, there is a large yield gap of avocado productivity in Ethiopia (about 4.2 t ha⁻¹) as compared to the world (7 t ha⁻¹) of which lack of improved avocado varieties has been a bottleneck [12]. The seed and peel weigh about 16 % and 11 %, respectively. However, these proportions vary among cultivars [13]. Therefore, alternative routes are needed for this waste management. This waste cannot be used still for any consumption. The presence of nitrogen allows it to be directly used as fertilizer or as soil improver (or compost) [8]. Avocado peels are used to evaluate the possibility of using and transforming waste into something valuable product, namely biodiesel thereby contributing towards alternative energy supply as well as recycles what would be discarded and resolves energy scarcity.

2 Materials and Method

2.1 Materials used for the production of biodiesel

Materials that were used during the experiment work are as follows: avocado peel oil, filter paper, heater mantle, knife, pipette, measuring cylinder, hydrometer, conical flask, plastic bags, hot plate, condenser, pH meter, measuring cylinder, and Piece of cloth.

2.2 Equipment

The equipment used during this experimental work are; Soxhlet extractor, vacuum pump, chiller, water bath, the oven was used for drying avocado peel and used to evaporate the excess alcohol from the extracted oil, Vibro viscometer, conical flasks, three-neck flasks, sample bottles, weighing balance, magnetic stirrer, test tubes, milling machine, FT-IR, sieve, beaker, density bottle, measuring cylinder, extraction glass

column, heating device, refractometer, thermometer, and separation.

2.3 Chemicals (Reagent)

Methanol was the most commonly used alcohol. N-hexane (99%) was used as a solvent for oil extraction from avocado peel powdered. The most commonly used catalyst was alcoholic sodium hydroxide (NaOH) (97%), hydrochloric acid (HCl), distilled water, and phenolphthalein indicator.

3 Biodiesel Production Process

There are many different production methods that can be used to produce biodiesel. From this transesterification process is the most popular method. Transesterification is the most conventional (popular way) and promising method used for biodiesel production. This is because this method is relatively easy, small reaction times, a straight conversion process, easy to operation, it significantly reduces the viscosity of vegetable oils without affecting the heating value of the original fuel, environmentally friendly, more conversion efficiency and quality of the converted fuel [2].

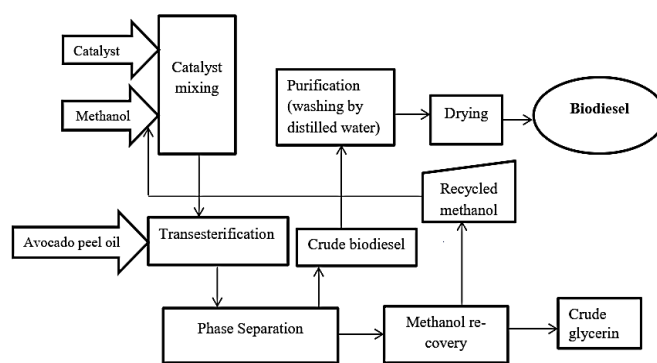


Fig. 1

Fig. 1 The production process of the biodiesel by transesterification reaction.

3.1 The Transesterification procedure

The transesterification process is the most common method to produce biodiesel, which is used for a catalyzed chemical reaction (Fig. 1). The production process requires a catalyst, usually a strong base, such as sodium hydroxide and potassium hydroxide [14], [15]. The biodiesel production process by transesterification reaction is made using three main components are; oil extracted from avocado peel and methanol alcohol, and a base catalyst sodium hydroxide is used in the experiments. A 500ml three-neck flask equipped with a magnetic stirrer, thermometer, and condenser are used during experimental work. The oil was stirred and heated in a water bath with the electric thermometer, within a temperature deviation of 1^oC. The procedures for the biodiesel production by transesterification reaction are:

1. Mixing of the methanol and the catalyst sodium hydroxide in a 200 ml beaker using the ratio of methanol and catalyst concentration respectively. A measured quantity of methanol was poured into a beaker and the sodium hydroxide pellet was measured in the weighing balance to get exactly the weight, and mix with methanol to 50 °C (in a water bath) and stirred manually until the catalyst is completely dissolved in methanol. During this reaction, the moisture level should be kept as low as possible. The

formation of soap decreases the biodiesel yield, consumes the catalyst and complicates the separation and purification process.

2. Methanol and sodium hydroxide solution was poured in the warm avocado peel oil in a 500 ml three-neck flask and stirred for (45-90) minutes using a magnetic stirrer at 500 rpm. After the reaction was completed, it was allowed to settle for 24 hours in a separating funnel.

3.2 Separation process

After the reaction was completed, the separation process is one of the most essential measures of biodiesel production. The production of biodiesel from the extracted oil by transesterification process is normally composed of biodiesel, glycerin, and other impurities. The properties of the fuel are strongly influenced by the impurity of the biodiesel product. Normally, the biodiesel is separated from byproduct glycerin using a simple gravitational settling (density difference) method (Fig. 2) and left for 24 hours. The separation process using the separation funnel was considered cost-effective. After 24 hours, two different layers were seen in the separating funnel. The above biodiesel layer was separated for further purified and the lower glycerol layer was decanted off.

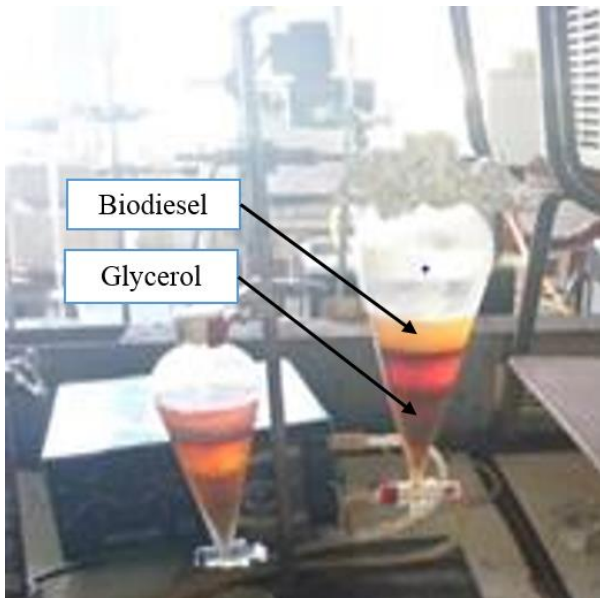


Fig. 2 Separation processes.

3.3 Washing and Drying

3.3.1 Washing of crude biodiesel

Once, separation has been done, the purification of the ester phase is necessary to ensure that the biodiesel meets the standard specifications of ASTM and EN. After the phase separation of glycerol and biodiesel, still has an excessive amount of soaps, catalyst, FFAs, water, methanol, glycerides, and other impurities. If these impurities are not reduced to their bounds value, this will have effects on the biodiesel as given in Table 1 and it may not meet the ASTM. The biodiesel is washed with warm distilled water to remove any impurities left in biodiesel after the reaction, and the initial settling is complete. The impurities include (primarily) excess alcohol, excess catalyst, soap formation glycerine, and a small amount of leftover lye. The ratio of water to biodiesel, 50% (related to the volume) (v/v) used is warmed to 50 °C for the washing of the biodiesel to extract impurities passed through the esters and other impurities.

The washing process of produced biodiesel was repeated until the pH of the biodiesel becomes relatively neutral. When biodiesel is first made, it is quiet with a pH of between 8 and 9. Washing with distilled water is sufficient to improve impurities bringing the pH down biodiesel becomes relatively neutral.

Table 1 Effects of Impurities on biodiesel performance [15].

Impurity of produced BD	Effects of impurities on biodiesel
FFAs	Corrosion and low oxidation stability.
Water	Hydrolysis (free fatty acid and alcohol formation), corrosion, bacteriological growth (filter blockage).
Methanol	Low values of density, viscosity, and low flashpoint.
soap, catalyst	Deposit in the injectors, filter blockage (sulfate ashes), and engine weakening.
Glycerol	Settling problems.

Table 2 Physico-chemical Properties of the obtained biodiesel and avocado peel oil and the standards of biodiesel in the United States (ASTM D-67510 and Europe (EN 14214).

Property	Avocado peel oil	Biodiesel Yields	EN 14214	ASTM D-6751
PH	6.2	7.8	5- 6.7	7-9
Density at 15 °C, kg/m ³	910	880	860-90	
Specific gravity	0.91	0.88	0.86-0.9	
Kinematic viscosity at 40 °C, cSt	5.1	4.22	3.5-5.0	1.9-6.0
Flashpoint, (°C)		161	>120	>130
API		31.14		30-45
Esters content %	38	95.2		
HHV (MJ/kg)	40	41.25	36-40	40-42
Fire point (0C)	250	190		--
Iodine value , g I ₂ /100 g	82	114.21	< 120	
Cetane number		49	> 51	> 47
Acid value , g NaOH/g	8	0.4		< 0.5
Free fatty acids	4.4	0.2		< 0.24
Refractive index @40 °C		1.54		1.4-1.7
Saponification value (gKOH/g)	200			

3.3.2 Drying (Evaporation) process

The last step was the drying process. Drying biodiesel requires a little more than heating the final biodiesel at 65 °C, for 15 - 20 minutes until any remaining moisture (water) evaporates and is removed from the sample. After the biodiesel is washed and dried, the yield of biodiesel production must be analyzed to confirm the standard specifications, and the product was then characterized using an empirical formula to confirm the biodiesel production yield and consider biodiesel yield with its standard.

4 Results and Discussions

4.1 Physicochemical Properties of Biodiesel

The production of biodiesels from avocado peel oil was characterized by empirical formula and FT-IR analysis. The extracted oil and the biodiesels of physicochemical properties are given in Table 2 comparing with the limit value below in Table 2 [17].

4.2 Statistical Analysis of the Experimental Results

Statistical software analysis of the model was performed to evaluate the analysis of variance (ANOVA). The regression

analysis and analysis of variance will be used as one of the primary tools for statistical data analysis, to generate surface plots, using the fitted equation, and by holding one of the independent constant variables using the Design Expert 6.8 program. The design summary is given in Table 3.

The predicted percentage conversion of the oil to biodiesel values using the conducted experimental design expert is 26 runs are shown in Table 3

The percentage actual yield of biodiesel produced at different process parameters was calculated using the formula as:

$$\text{Yield of FAME (biodiesel \%)} = \frac{\text{weight of BD produced}}{\text{weight of oil used}} \times 100$$

Table 3 Design Summary of factorial designs.

Design Summary of Design expert® 6.8 software	
Study type	Response surface
Initial design	CCD
Design model	Quadratic, polynomial
Run	26

Table 4 Actual versus Predicted model of biodiesel yield.

Standard Order	Residual	Leverage	Student Residual	Cook's Distance	Outlier T	Run Order	Actual Value	Predicted Value
1	-0.22	0.687	-0.244	0.009	-0.233	3	67.60	67.82
2	1.36	0.687	1.484	0.323	1.582	10	72.90	71.54
3	-0.70	0.687	-0.767	0.086	-0.752	18	69.50	70.20
4	-0.37	0.687	-0.407	0.024	-0.391	7	73.70	74.07
5	-0.71	0.687	-0.774	0.088	-0.758	21	69.50	70.21
6	-0.32	0.687	-0.354	0.018	-0.340	20	73.30	73.62
7	1.71	0.687	1.864	0.509	2.149	4	78.40	76.69
8	-0.66	0.687	-0.719	0.076	-0.702	25	79.60	80.26
9	-0.29	0.687	-0.319	0.015	-0.306	22	68.70	68.99
10	-0.76	0.687	-0.826	0.100	-0.814	2	70.90	71.66
11	1.28	0.687	1.392	0.284	1.462	9	72.90	71.62
12	-0.24	0.687	-0.265	0.010	-0.253	16	74.20	74.44
13	1.32	0.687	1.440	0.304	1.525	12	68.50	67.18
14	-0.24	0.687	-0.266	0.010	-0.254	26	69.30	69.54
15	-2.31	0.687	-2.517	0.928	-3.687*	13	71.60	73.91
16	1.17	0.687	1.277	0.239	1.319	1	77.60	76.43
17	-0.88	0.901	-1.696	1.740	-1.882	23	87.10	87.98
18	0.26	0.976	1.040	2.981	1.044	6	95.20	94.94
19	-2.24	0.145	-1.475	0.025	-1.571	11	90.70	92.94
20	-0.50	0.144	-0.330	0.001	-0.317	8	92.90	93.40
21	-0.36	0.400	-0.279	0.003	-0.267	17	92.70	93.06
22	0.53	0.400	0.414	0.008	0.398	15	93.80	93.27
23	-0.68	0.400	-0.536	0.013	-0.518	5	91.50	92.18
24	0.85	0.400	0.671	0.020	0.653	14	92.90	92.05
25	1.51	0.119	0.979	0.009	0.977	19	93.20	91.69
26	1.51	0.119	0.979	0.009	0.977	24	93.20	91.69

* exceeds limits

Table 5 Analysis of variance (ANOVA) for the quadratic model of esterification.

Source	Sum of Squares	DF	Mean Square	F Value	Prob > F	
Model	2661.13	14	190.08	70.65	< 0.0001	Significant
A	38.88	1	38.88	14.45	0.0029	
B	85.97	1	85.97	31.95	0.0001	
C	19.14	1	19.14	7.11	0.0219	
D	7.09	1	7.09	2.64	0.1327	
A ²	19.78	1	19.78	7.35	0.0202	
B ²	22.65	1	22.65	8.42	0.0144	
C ²	6.84	1	6.84	2.54	0.1391	
D ²	0.56	1	0.56	0.21	0.6570	
AB	0.024	1	0.024	8.857E-003	0.9267	
AC	0.090	1	0.090	0.033	0.8582	
AD	1.10	1	1.10	0.41	0.5352	
BC	16.81	1	16.81	6.25	0.0295	
BD	0.063	1	0.063	0.023	0.8816	
CD	17.64	1	17.64	6.56	0.0265	
Residual	29.59	11	2.69			
Lack of Fit	29.59	10	2.96			
Pure Error	0.000	1	0.000			
Cor Total	2690.72	25				

The model equation that relates the transesterification reaction process variables in terms of actual value after eliminating the insignificant terms was given below. The predicted model for the percentage of biodiesel equation in terms of Coded factors is shown in the equation below:

$$\begin{aligned} \text{Biodiesel yield} = & +91.69 + 1.56 * A + 2.32 * B + 1.09 * \\ & C - 0.67 * D - 356.10 * A^2 + 147.62 * B^2 + 147.09 * C^2 \\ & + 42.09 * D^2 + 0.039 * A * B - 0.075 * A * C - 0.26 * \\ & A * D + 1.03 * B * C + 0.063 * B * D - 1.05 * C * D \end{aligned} \quad 2$$

where A – a molar ratio of oil to methanol
B – Reaction temperature
C – Reaction time
D – Amount of catalyst

Equation (2) provided the coefficients of the model by using a quadratic model equation. From the ANOVA the response surface quadratic model by the transesterification reaction, the Model F-value of 70.65 implies the model is significant. There is only a 0.01% chance that a "Model F-value" this large could occur due to noise. Values of "Prob > F" less than 0.0500 indicate model terms are significant. In this case, A, B, C, A², B² in addition, the interaction BC and CD are significant models. From this Prob > F Values greater than 0.1000 indicate the model terms are not significant. ANOVA for the quadratic model for esterification is evaluated in Table 5.

From the Table 5, F-values of the model coefficients, the reaction temperature in both linear and quadratic is less than 0.0001. This indicated that reaction temperature is the most significant in determining the model than the other and the value

of the methanol to oil molar ratio is the second. However, to minimize error, all of the coefficients were measured in the design. The Lack of Fit F-value of 2.96 indicates its insignificance relative to the pure error. Non-significant lack of fit is good since we want the model to fit.

Table 6 Model adequacy measures from the model.

Std. Dev.	1.64	R-Squared	0.9890
Mean	80.05	Adj R-Squared	0.9750
C.V. %	2.05	Pred R-Squared	0.8528
Press	396.15	Adeq Precision	22.281

Table 6 shows the model adequacy measures from the model. The "Pred R-Squared" of 0.8528 is in reasonable agreement with the "Adj R-Squared" of 0.9750 in less than 0.15 difference as one might expect. "Adeq Precision" measures the signal-to-noise ratio due to random error. A ratio of 22.281 indicates an adequate signal. Therefore, this model can be used to navigate the design space.

The regression coefficients and the corresponding 95% CI (Confidence Interval) Low and High were presented in Table 7. If zero was in the range high and low 95% Confidence interval, the factors do not affect. From the 95% CI High and Low values of each model term, it could be concluded that the regression coefficients of catalyst concentration and the interaction terms of the molar ratio of oil to methanol and reaction time have a highly significant effect on biodiesel production.

Table 7 Regression coefficients and significance of response surface quadratic model for transesterification.

Factor	Coefficient Estimate	DF	Standard Error	95% CI		VIF
				Low	High	
Intercept	91.69	1	0.57	90.45	92.94	
A	1.56	1	0.41	0.66	2.46	1.00
B	2.32	1	0.41	1.41	3.22	1.01
C	1.09	1	0.41	0.19	1.99	1.00
D	-0.67	1	0.41	-1.57	0.24	1.00
AB	0.039	1	0.41	-0.86	0.94	1.00
AC	-0.075	1	0.41	-0.98	0.83	1.00
AD	-0.26	1	0.41	-1.17	0.64	1.00
BC	1.03	1	0.41	0.12	1.93	1.00
BD	0.063	1	0.41	-0.84	0.97	1.00
CD	-1.05	1	0.41	-1.95	-0.15	1.00

Table 8 Statistics model summary of the response quadratic model for transesterification reaction.

Source	Sum of Squares	DF	Mean Square	F - Value	P-value Prob > F	Std. Dev.	R ²	Adj. R ²	Pred. R ²	Press
Mean	1.666E+005	1	1.666E+005							
Linear	181.24	4	45.31	0.38	0.8209	10.93	0.0674	-0.1103	-0.3360	3594.85
2FI	35.85	6	5.98	0.036	0.9997	12.84	0.0807	-0.5322	-2.7127	9989.75
Quadratic	2444.04	4	611.01	227.11	< 0.0001	1.64	0.9890	0.9750	0.8528	396.15
Cubic	25.98	9	2.89	1.60	0.4431	1.34	0.9987	0.9832		+
Residual	3.61	2	1.81							
Total	1.693E+005	26	6512.11							

The quality of the model evaluated based on the correlation coefficient value, R², this R² value for equation 2 is 0.989 (Table 8). This showed that 98.9% of the total variation in the biodiesel yield was attributed to the experimental variables studied. The R² value close to unity, the better the model will be as it will give predicted values that are closer to the actual values for the response. From the ANOVA and regression analysis of Table 5 and Table 7 respectively it can be seen that the linear terms of A, B, and C, the quadratic term A² and B² are significant (because Prob > F less than 0.05), but the interactions BC and CD are insignificant.

In Fig. 3 the predicted vs. actual values were obtained using the experimental data run correspondence, since the plot contains a line of slope unit (i.e. the line of perfect fit) with points corresponding to zero error between predicted values and actual. This shows the performance of the correlation in an evident way. Hence, the regression model equation granted a very accurate description of the experimental data, in which all the points are very close to the perfect fit. This outcome indicates that it was successful in creating the correlation between the four process parameters to FAME.

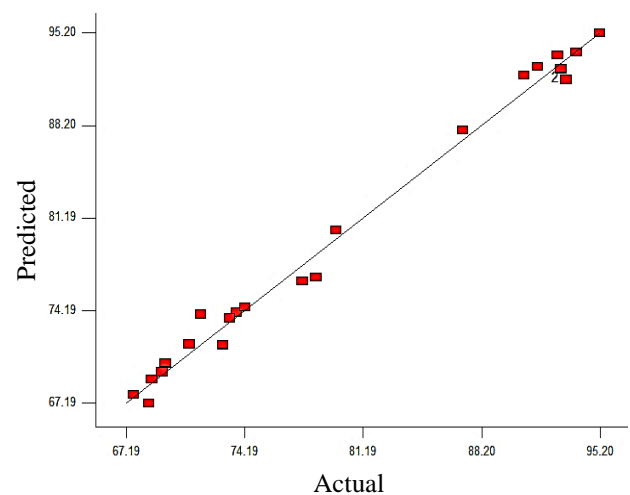


Fig. 3 Plot for the actual vs. predicted FAME yield.

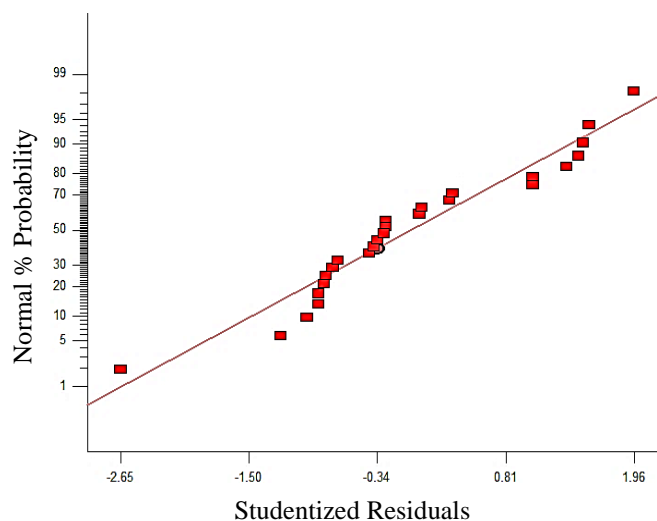


Fig. 4 Normal plots of residuals.

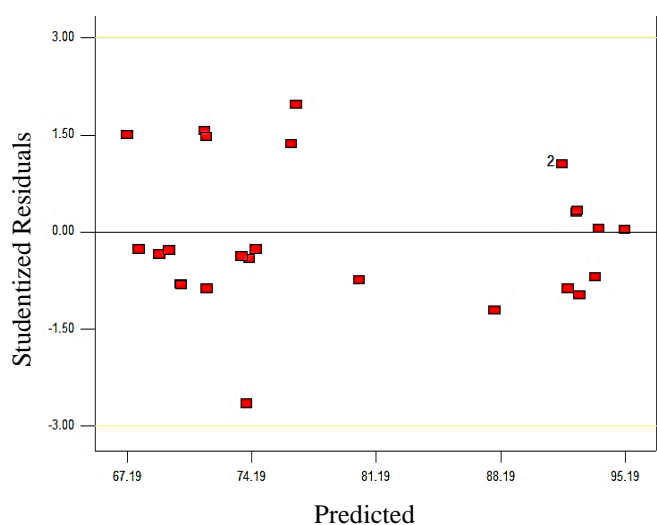


Fig. 5 Residual vs. predicted values.

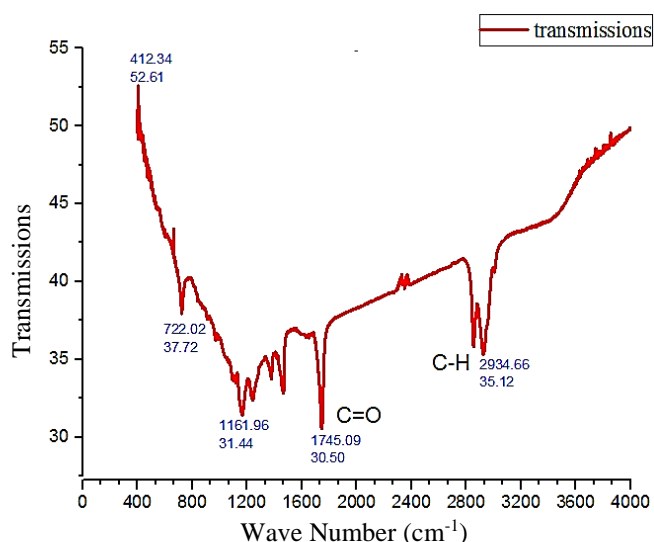


Fig. 6 The FT-IR produced biodiesel process.

In Fig. 4, as shown above, the standard probability plot shows the residuals following a normal distribution, in the case of this experiment the points in the plots shows fit to a straight line in the figure, this shows that the quadratic model satisfies the

analysis of the assumptions of variance (ANOVA) i.e. the error distribution is approximately normal.

From the model, the residuals should be structure less; in particular, they should be unrelated to any other variable including the predicted response. The plot of these response value tests the assumption of constant variance and this shows random distribution which justifying no need for any alteration to minimize personal error (Fig. 5).

4.3 Analysis of Fourier transforms infrared (FT-IR)

Fourier transforms infrared spectroscopy; FT-IR was to analyze the function group presence in the produced biodiesel and its raw materials avocado peel oil. FT-IR analysis was performed using an instrument as shown in Fig. 6. One of the detections of transesterification efficiency of oil by determination of the active groups produced from these processes. The FT-IR spectra will be recorded at a surrounding temperature in the wavenumber between 4000-400 cm^{-1} .

The biodiesel produced from the extracted avocado peel oil was analyzed by FT- IR spectrum. The main change that takes place during the conversion from triglyceride oil to biodiesel was the gain of a CH_3 carbon in the biodiesel product found in the range of 1438- 1459 cm^{-1} which is not present in the spectra of the oil. Biodiesel results in the formation of carbon-hydrogen bonds at 2855-3008 cm^{-1} , ester functionality at 1738-1759 cm^{-1} , the carbons at 1438-1459 cm^{-1} , and carbon-oxygen bonds at 1171-1197 cm^{-1} . C = O carbonyl compound (aldehydes, acids, etc) are the strong C = O stretching absorption bands in the region of 1870-1540 cm^{-1} . If ester this band appears in the 1705 cm^{-1} and 1658 cm^{-1} . C-O-C (Ethers), these stretching vibrations produce a strong band in the 1200-900 cm^{-1} region. Other identifying peaks found in the oil were at 2926 cm^{-1} and 2855 cm^{-1} that represent sp^3 hybridized carbon molecules that are found in the long carbon chain of the biodiesel [8].

5 Conclusion

In this study, biodiesel was produced by the transesterification method using the oil extracted from the avocado peel, methanol as alcohol, and sodium hydroxide as a catalyst to produced biodiesel. The process parameters that affect the yield of FAME conversion have been studied by design expert 6.8 Software and the statistical analysis. The outputs of the experimental run conducted have been analyzed by using physicochemical parameter determination. The whole results show that the avocado peel oil could be used to produce biodiesel as a feedstock. The characterized physicochemical properties of the produced biodiesel from APO could be used as an alternative energy resource in engines.

The obtained biodiesel produce by the transesterification process was, ranged from 67.8 to 95.2%. A 95.2% FAME conversion was obtained using a methanol/oil ratio of 6:1, 1.21g NaOH, reaction time 67.5min, and 60 $^{\circ}\text{C}$ reaction temperature. The physicochemical properties (characterization) of produced biodiesel are, (pH of 7.8, the specific gravity of 0.88, density at 15 $^{\circ}\text{C}$, kg/m^3 , the kinematic viscosity of biodiesel was found to be 4.22 $\text{m}^2 \cdot \text{s}^{-1}$ at 40 $^{\circ}\text{C}$, the flashpoint was 161 $^{\circ}\text{C}$ and Cetane number of 49 are well-matched the international standards and compared to ASTM and EN standards, which indicates it is possible to produce quality biodiesel.

Finally, this result shows that the oil extracted from avocado peel can be used for biodiesel production as an alternative feedstock.

References

- [1] Huang, D., Zhou, H. and Lin, L., 2012. Biodiesel: an alternative to conventional fuel. *Energy Procedia*, 16, pp.1874-1885.
- [2] Gashaw, A., Getachew, T. and Teshita, A., 2015. A review on biodiesel production as alternative fuel. *J. For. Prod. Ind.*, 4(2), pp.80-85.
- [3] Pinto, A.C., Guarieiro, L.L., Rezende, M.J., Ribeiro, N.M., Torres, E.A., Lopes, W.A., Pereira, P.A.D.P. and Andrade, J.B.D., 2005. Biodiesel: an overview. *Journal of the Brazilian Chemical Society*, 16(6B), pp.1313-1330.
- [4] Elkady, M.F., Zaatout, A. and Balbaa, O., 2015. Production of biodiesel from waste vegetable oil via KM micromixer. *Journal of Chemistry*, 2015.
- [5] Dash, S.K. and Lingfa, P., 2018, June. An overview of biodiesel production and its utilization in diesel engines. In *IOP Conference Series: Materials Science and Engineering* (Vol. 377, No. 1, p. 012006). IOP Publishing.
- [6] Van Gerpen, J., 2005. Biodiesel processing and production. *Fuel processing technology*, 86(10), pp.1097-1107.
- [7] Demirbaş, A. and Kara, H., 2006. New options for conversion of vegetable oils to alternative fuels. *Energy Sources, Part A*, 28(7), pp.619-626.
- [8] Hiwot, T., 2017. Determination of oil and biodiesel content, physicochemical properties of the oil extracted from avocado seed (*Persea Americana*) grown in Wonago and Dilla (gedeo zone), southern Ethiopia. *Chem. Int.*, 3(3), pp.311-319.
- [9] Ayoola, A.A., Hymore, F.K., Obande, M.A. and Udeh, I.N., 2012. Optimization of experimental conditions for biodiesel production. *International Journal of Engineering & Technology*, 12(6), pp.130-133.
- [10] Ogunwole, O.A. and Adedipe, O., 2012. Production of biodiesel from jatropha oil (curcas oil). *Research Journal of Chemical Sciences*, 2(11), pp. 30-33.
- [11] Gude, V.G., Patil, P.D., Grant, G.E. and Deng, S., 2012. Sustainable Biodiesel Production, Second world Sustainable forum, 1-14.
- [12] Jalata, Z., 2021. Current Status, Potentials and Opportunities of Avocado Production as an Alternative Crop: the Case of Ethiopia: A Review. *Agricultural Reviews*.
- [13] Mora-Sandí, A., Ramírez-González, A., Castillo-Henríquez, L., Lopretti-Correa, M. and Vega-Baudrit, J.R., 2021. Agro-Industrial Avocado (*Persea americana*) Waste Biorefinery.
- [14] Aydın, K., Sarıbiyık, O.Y., Özcanlı, M., Serin, H. and Serin, S., 2010. Biodiesel Production from Ricinus Communis Oil and Its Blends with Soybean Biodiesel. *Strojniski Vestnik/Journal of Mechanical Engineering*, 56(12).
- [15] Demirbas, A., 2008. Comparison of transesterification methods for production of biodiesel from vegetable oils and fats. *Energy Conversion and Management*, 49(1), pp.125-130.
- [16] Prah, E., 2010. *Biodiesel analytical development and characterisation* (Doctoral dissertation, Stellenbosch: University of Stellenbosch).
- [17] Indhumathi, P., Syed Shabudeen, P.S., Shoba, U.S, 2014. A Method for Production and Characterization of Biodiesel from. *International Journal of Bio-Science and Bio-Technology*, 6(5), pp.111-122.

Design and Analysis of A Vortex Induced Vibration Based Oscillating Free Stream Energy Converter

Ratan Kumar Das^{1*}, Muhammad Taharat Galib²

¹Department of Mechanical Engineering, Chittagong University of Engineering and Technology, Chittagong-4349, Bangladesh

²Department of Mechanical Engineering, City University, Dhaka-1215, Bangladesh

Received: April 14, 2021, Revised: June 25, 2021, Accepted: June 27, 2021, Available Online: June 29, 2021

ABSTRACT

The Kármán Vortex Shedding is one of the special types of vortex that is generated from asymmetric flow separation. For many years engineers tried to suppress the vortex shedding as it brings unnecessary motion to the static members inside the flow field. A converter model is designed and studied to harness the energy associated with this vortex shedding and convert it into usable form rather than suppressing it. It is a bluff body placed on the free stream incurring vortex-induced vibration and giving out a swinging pendulum motion. This motion is utilized to produce electricity. The model is analyzed on the free stream of water and conversion efficiency of 8.9% is achieved. A theoretical formula is derived regarding the force acting on the bluff body during the motion. Various parameters such as aspect ratio, flow velocity, lock-in delay, frequency of oscillation, etc. as well as their relations are studied by simulating the model in ANSYS FLUENT 18.1 for different configurations. From the simulated results it is obvious that as the lift force on the bluff body increases, more power generation is possible. Also, the experimental results paved the way for further study for practical large-scale implementation of the converter.

Keywords: Vortex-Induced Vibration, Oscillating Energy Converter, Free Stream Energy



This work is licensed under a [Creative Commons Attribution-Non Commercial 4.0 International License](https://creativecommons.org/licenses/by-nc/4.0/).

1 Introduction

Renewable energy is the most developing field in modern engineering. As the limited natural resources are being perished, the world is targeting energy transformations especially renewable energy. The concept of vortex in the field of renewable energy is pretty old. But no reliable base has been structured for continuous and large-scale power generation. Vortex is a regular phenomenon in various flow fields. Kármán Vortex Shedding is one of the special types that is generated from asymmetric flow separation. For many years, engineers tried to suppress the vortex shedding as it brings unnecessary motions to the static members inside the flow field. In fluid dynamics, a Kármán vortex street (or a von Kármán vortex street) is a repeating pattern of swirling vortices, caused by a process known as vortex shedding, which is responsible for the unsteady separation of flow of a fluid around bluff bodies [1]. In practice, this phenomenon appears after the destabilization of the flow due mainly to the surface roughness of a bluff body. As roughness is one of the inherited properties of a body, it can surely be used for reasonable purposes. Vortex can induce vibration in a body. To extract power from the vortex, this vibration has to be augmented by proper mechanism and transformed into suitable power generating motion. Again, many of the natural sources of water are the open channel. There is a vast free stream of water available from those. A huge amount of free energy can be harvested from these flows to cope with the upcoming demand for energy. Artificial vortex can be created on these open flow channels and the desired motion can be gained.

As mentioned by Von Karman [2], Ever since Leonardo da Vinci first observed Vortex-Induced Vibration (VIV) circa 1500AD, in the form of “Aeolian Tones,” engineers have been trying to spoil vortex shedding and suppress VIV to prevent

damage to equipment and structures. Further, Von Karman himself at Cal Tech proved that the Tacoma Narrows bridge collapse in 1940 was due to VIV.

Strouhal [3] first noticed and experimented on the vortex shedding in wires in 1878. He established a dimensionless number ‘Strouhal Number’ characterizing the oscillating flow mechanism. Dorman, et al. [4] invented a technique to improve turbine aerodynamic performances in 1968. Edwards [5] patented a wind energy converter utilizing vortex augmentation. He converted the linear momentum of wind energy into a pair of concentrated, counter-rotating, and side-by-side regions of high angular momentum to extract energy from the established regions for driving electric generators or generators therefrom. Patterson and Flechner [6] investigated an exploratory wind tunnel of a wingtip-mounted vortex turbine for vortex energy recovery in 1985. In 1990, Patterson [7] patented his experiment of extracting rotational energy from the vortex created at the aircraft wingtips which consists of a turbine with blades located in the crossflow of the vortex and attached downstream of the wingtip. From then on, operating the turbine at the vortex zone for increased efficiency was regularly researched. Jensen [8] made a concept on energy converter using imploding plasma vortex heating in late 1994. In 2008 Carney [9] patented his invention which includes a bluff body coupled to a gyroscopic electrical generator. In recent years from 2016 various projects named Vortex Bladeless by Cajas, et al. [10] are commercially started implementing large elastic columns or conical-shaped bladeless bars which vibrate due to vortex shedding that is generated by wind-column interaction. In 2008, Bernitsas, et al. [11] invented a new concept named VIVACE technology. This Vortex-Induced Vibration Aquatic Clean Energy refers to cylindrical-shaped horizontal bars that are submerged underwater undergo VIV and vibrates perpendicular to the

direction of flow producing electricity. According to him, from wind energy, power extraction using vortex has begun long ago. Various devices were designed to extract vortex power from the flow of liquid or water in 1957, 1994, and 2006. But none of them were able to go for large-scale implementation. Vortex generation from ocean energy emerged truly from 2007.

Throughout these studies, it is seen that no attempt is taken for harnessing energy from the free stream surface of open channel flow based on VIV. Thus, in this study, a swinging vortex energy converter is designed and implemented to convert the free stream flow energy of water into electrical energy. A bluff body (cylinder) is placed on the free stream of a flow. Karman Vortex Street will be formed and a transverse vibration will occur. Electricity generation is proportional to the frequency of the vibration. From the experiment, for maximum frequency, a suitable depth to diameter ratio, correlation length, the power output of the bluff body is obtained for different flow velocities. The model is simulated using ANSYS software to get relations among various parameters in different conditions.

The reason behind the selection of open flow channels of water is to minimize the effect on the environment as well as gaining maximum efficiency in energy conversion. Also, the aquatic life has a close similarity with vorticity and their movements which ensures an undisturbed environment. As there is almost no harm in vortex power generation from the free stream and with less continuous effort, this study deserves a go for the possibility of getting sustainable renewable energy.

2 Methodology

The study is carried out in three steps. A converter model is designed and fabricated, the experimental setup is run to check the feasibility along with data collection and 25 individual numerical simulations have been done to analyze the performance of the model. The experimental model has a fixed geometry and it is implemented on an open channel flow where the velocity is fixed. Hence, the setup yielded some results which are used to calculate power output and efficiency. This has proved the feasibility of the proposed model. A numerical model is also designed. First, it is simulated with the same configuration as the physical one. Then the numerical model is designed using five different aspect ratios (height to diameter ratio) and for each aspect ratio, the model is simulated for five different velocities. Hence, a total of 25 individual numerical simulations is carried out. From these simulations, the relationships amongst coefficient of lift (lift force generated on the cylinder surface to the dynamic force applied on the projected area of the body by the free stream), vibration frequency, delay time, velocity, and aspect ratios are analyzed.

2.1 Physical Model

The design and actual fabricated model is shown in Fig. 1. The model consists of a solid cylinder that is welded at the bottom of a steel bar. A metal sheet is attached at the lower mid-portion of the bar. At the top of the bar, a rectangular bar magnet is attached. The cylinder has a height of 5 cm and a diameter of 4.5 cm. The bar magnet has a magnetic flux density of 0.1 Tesla. The coil has 100 turns of copper wire with nickel insulation. Through the gap of the coil, the bar magnet attached with the upper portion of the converter can oscillate almost linearly. During operation, the cylindrical portion is submerged under the open channel flow up to its upper surface.

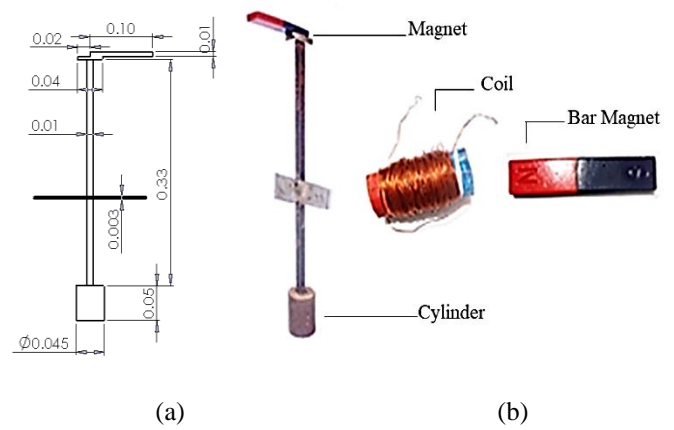


Fig. 1 (a) Design of the model and (b) Actual fabricated model with coil and magnet

Initially, the model rests on its metal sheet which hangs on two other external support rods. Due to continuous laminar flow, flow separation takes place around the cylindrical surface, and the vortex is formed accordingly. This vortex induces vibration to the cylinder, hence on the magnet. As a result, the cylinder undergoes pendulum swing being supported on the metal sheet. The magnet swings nearly with linear motion through the mid-space of the coil generating electricity according to the law of Electromagnetic Induction. This is depicted in Fig. 2. The velocity of the experimental flow channel was 0.3 m/s. A multimeter is used to estimate the power generation.

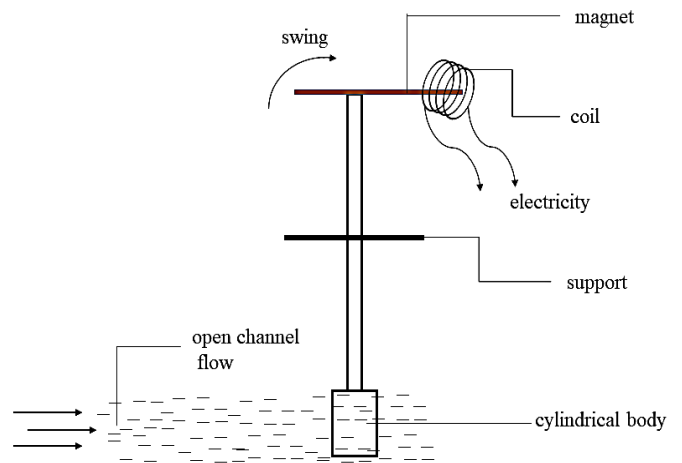


Fig. 2 Schematic diagram of the experiment

For a cylindrical body, the primary response mode is transverse to the flow. In-line oscillations of smaller magnitude are also observed in VIV and strengthen transverse oscillations [12]. As the flow velocity V_∞ increases, lock-in for a high mass ratio system is reached when the vortex formation frequency $f_{v, form}$ is close enough to the body's natural frequency f_n , water as seen, Lock-in or vortex synchronization occurs over a broad range. The data collected from the experiment is processed using the following equations:

The frequency of the body, in general, is given by [3]

$$f = 0.198 \frac{V_\infty}{D} \left(1 - \frac{19.7}{R_e} \right) \quad (1)$$

The power of the free stream can be calculated with [11],

$$P_{\infty} = \frac{1}{2} \rho V_{\infty}^3 DL \quad (2)$$

Power gained at output (electric power) is given by

$$P_{elc} = VI \quad (3)$$

Efficiency can be calculated by

$$\eta = \frac{P_{elc}}{P_{\infty}} \times 100 \% \quad (4)$$

2.2 Numerical Model

To study different parameters of the converter and flow region, a numerical model is developed. The model which has the same configuration and input parameters as the experimental one is shown in Fig. 3. The model is also modified for aspect ratios of 0.6, 0.8, 1.11, 1.2, and 1.5. For each of these aspect ratios, five different velocities are selected and simulated. The velocities are 0.3 m/s, 1 m/s, 2 m/s, 3 m/s and 4 m/s. The different aspect ratios are achieved by fixing the cylinder length at 0.05 m and changing the diameter accordingly to get the aforesaid aspect ratios. For these 5 different diameters of the cylinder, 5 different meshings are done keeping the meshing method, edge sizing, and inflation parameters the same.

The actual design is imported to ANSYS Design Modeler and various dimensional parameters are set. The rectangular portion is set as the fluid domain. The cut-out circular portion represents the outer surface of the cylinder. The cylinder is set to solid iron. The channel length is set to 0.6096 m and width is set to 0.3048 m maintaining similarity with the experimental setup. The diameter of the circle is changed as per the required aspect ratio. Meshing is carried out with ANSYS Meshing as depicted in Fig. 3. The meshing method is selected as all triangular method. Edge sizing is performed with uniform Size Function, Element Size of 0.001 m and Growth Rate of 1.20. The boundary of the cylinder is inflated for increased accuracy. The inflation option is set to First Layer Thickness, First Layer Height of 0.60.0005 m, and Maximum Layers of 30 and a Growth Rate of 1.10. The flow is set towards positive X-axis. Meshed model is opened in the FLUENT solver and various parameter is set. As for the solver type, a pressure-based solver is selected. Model is set to viscous-laminar. The boundary conditions are given as follows- inlet velocity is set as per the experiment, the two sides of the flow domain are set to the wall (applies no-slip condition), the cylinder is also set to a wall, the outlet is configured as pressure output. For the calculation of lift coefficients, corresponding reference values (area, density, and viscosity) are set according to proper aspect ratios and inlet conditions. Each calculation is allowed to run for sufficient time depending upon the lock-in time. Time step size is set to 0.01. For convergence with sufficient accuracy, a maximum of 200 iterations per time step is set.

The plot of the lift coefficients generated for each simulation is the key to understand the force acting on the cylinder for the given conditions and parameters. As the lock-in phase is achieved, a continuous similar vibration curve of maximum amplitude is found. The peak values of those sinusoidal curves are collected which corresponds to the coefficient of lift at maximum amplitude. Also, the frequency of vibration after the lock-in is counted. The lock-in delay (time) for each velocity and aspect ratios of the model are noted too.

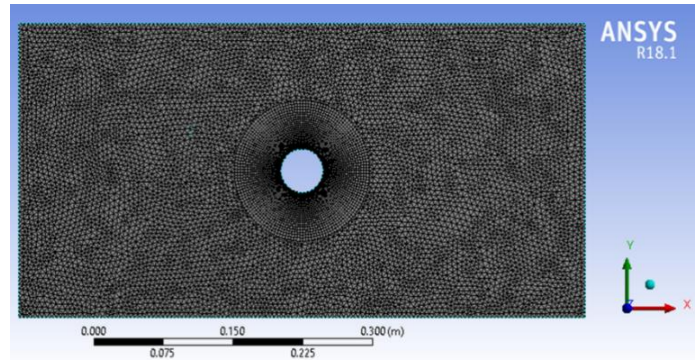


Fig. 3 Meshing of the model

3 Results and Discussion

3.1 Experimental Results

From the experimental setup, the free stream velocity of the channel is $V_{\infty} = 0.3 \text{ m/s}$, where the Cylinder Height, $L = 0.05 \text{ m}$; Diameter, $D = 0.045 \text{ m}$ and the Density of water is 100 kg/m^3 . From the multimeter, the voltage reading is $V_{rms} = 3.54 \text{ mV}$ and the Current, $I = 0.768 \text{ A}$. The number of full oscillations is 10 and it took a time of $t = 8.33 \text{ s}$. The Lock-in Delay is 7 s. The frequency of the converter is found to be 1.2 Hz. Power generated by the converter is calculated to be 2.715 mW whereas the power available from the source is calculated to be 30.375 mW. Hence, the conversion efficiency of the designed model is 8.9%. The conversion efficiency achieved by this model is satisfactory at this primary stage of development and very much affordable compared to the solar converter. This proves that the concept of harnessing free stream energy with a swinging VIV converter is feasible.

3.2 Numerical Results

From the numerical study, a total of 25 sets of Lift coefficient vs time charts, Streamline graphs, and pressure contours are found. Only the graphs of the numerical model which has a similar configuration with the experimental one are shown in Fig. 4. All other individual simulations for five different aspect ratios for lift coefficient, lock-in delay, and velocities yield similar sets of graphs. Values from those graphs are extracted and presented in Table 1.

The pressure contour in Fig. 4 (a) depicts that pressure is much higher at the inlet section of the cylinder surface due to stagnation. The immediate lowest pressure regions in circular forms just after the downstream portion of the cylinder represent vortex formation repetitively. The velocity streamlines in Fig. 4 (b) clearly show that the cylinder is experiencing lift force on one side and after a small time step it experiences lift force on the other side. This proves the vibration induced by the vortex. This repetitive change of direction of lift force causes the cylinder to swing along Y-axis. The value of the coefficient of lift with respect to flow time can be obtained from Fig. 4 (c). Here it is seen that the lift coefficient is inconsistent at first and it takes some time to become consistent and changes in a sinusoidal form. The time it takes to become stable is referred to as lock-in delay. Stable power conversion can be only obtained from the vibration after the lock-in. This graph also provides the number of vibrations against the time i.e. the frequency.

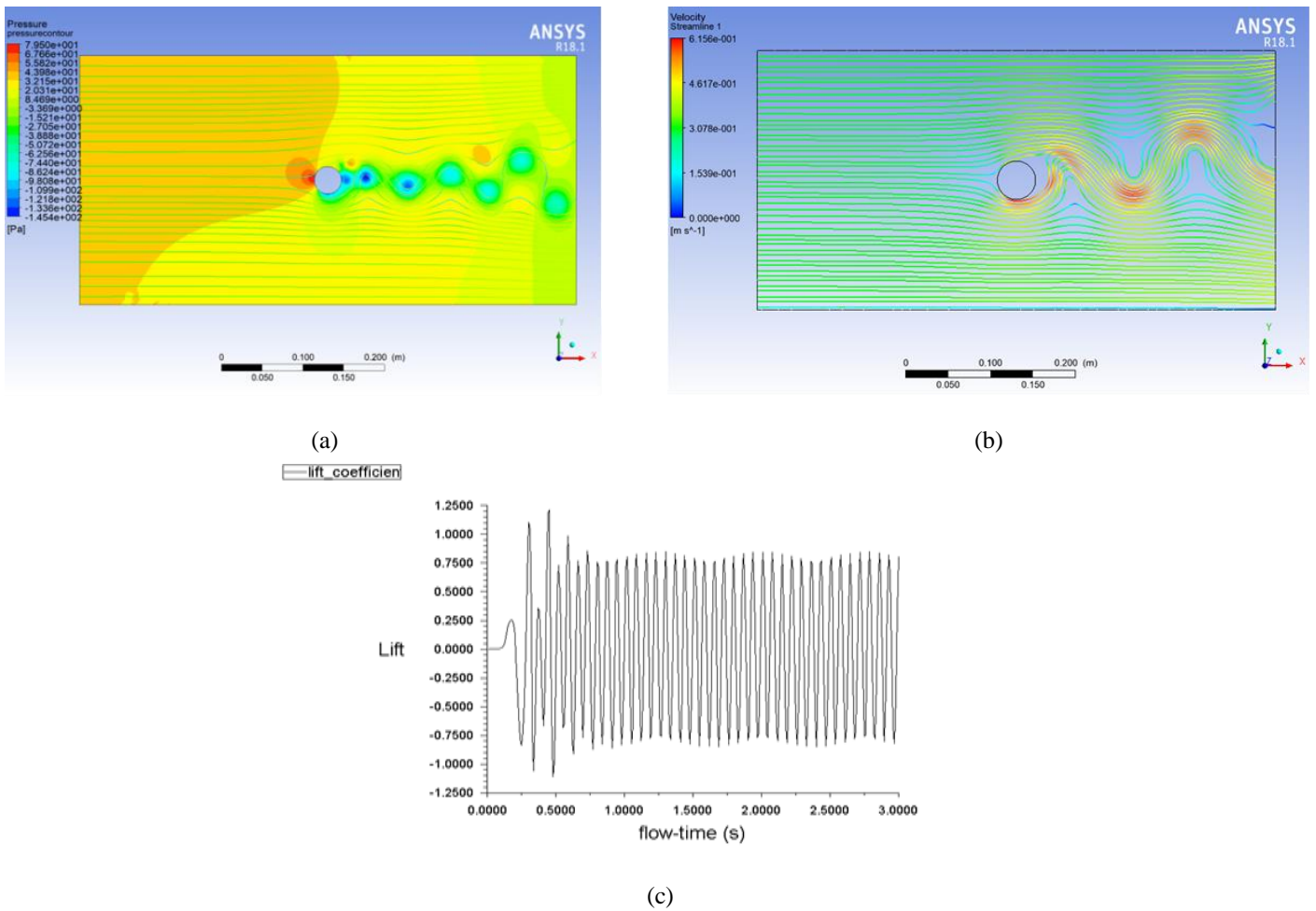
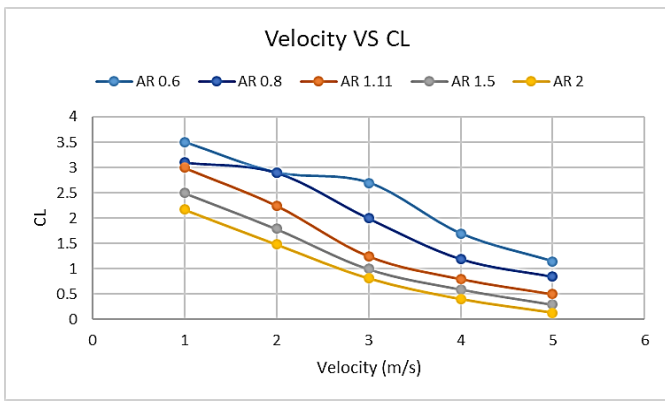


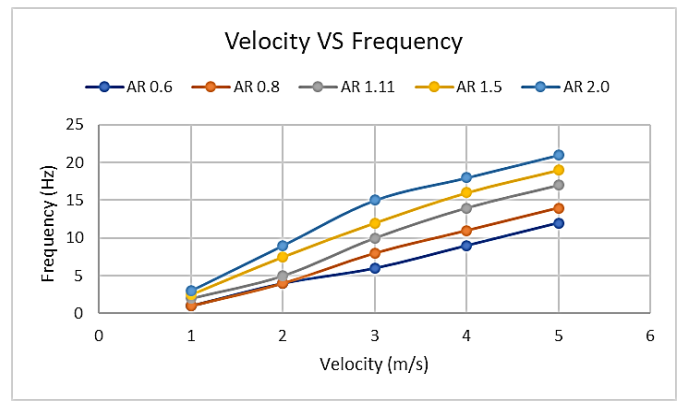
Fig. 4 Plots of (a) Pressure Distribution, (b) Velocity Streamlines, and (c) Coefficient of Lift

Table 1 Simulation results of Lock-in Delay, CL, and Frequency at different velocities

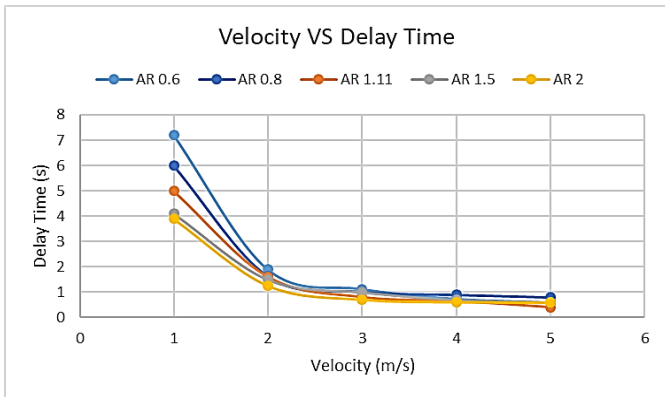
Diameter (m)	AR	Lock-in Delay (s) at different Velocities				
		0.3 m/s	1 m/s	2 m/s	3 m/s	4 m/s
0.083	0.6	7.2	1.9	1.13	0.75	0.6
0.0625	0.8	6	1.63	1.02	0.9	0.8
0.045	1.11	5	1.6	0.8	0.65	0.4
0.0334	1.5	4.1	1.5	1	0.7	0.6
0.025	2	3.9	1.25	0.7	0.6	0.59
Diameter (m)	AR	CL at different Velocities				
		0.3 m/s	1 m/s	2 m/s	3 m/s	4 m/s
0.083	0.6	3.5	2.9	2.7	1.7	1.15
0.0625	0.8	3.1	2.9	2	1.2	0.85
0.045	1.11	3	2.25	1.25	0.8	0.5
0.0334	1.5	2.5	1.79	1	0.6	0.3
0.025	2	2.17	1.48	0.81	0.4	0.13
Diameter (m)	AR	Frequency (Hz) at Different Velocities				
		0.3 m/s	1 m/s	2 m/s	3 m/s	4 m/s
0.083	0.6	1	4	6	9	12
0.0625	0.8	1	4	8	11	14
0.045	1.11	2	5	10	14	17
0.0334	1.5	2.5	7.5	12	16	19
0.025	2	3	9	15	18	21



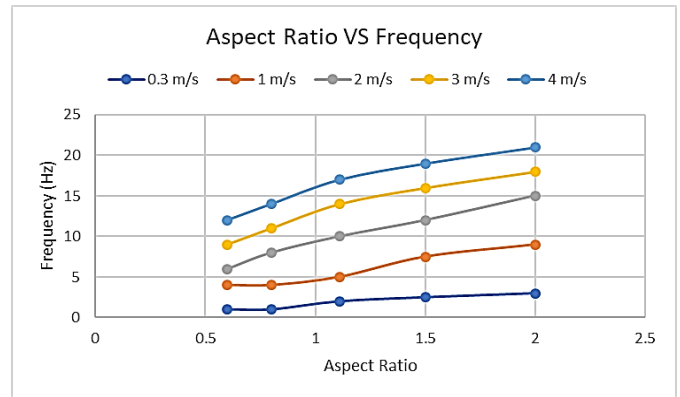
(a)



(a)



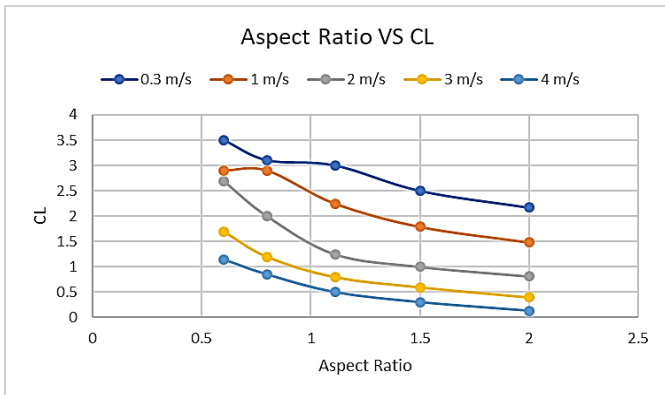
(b)



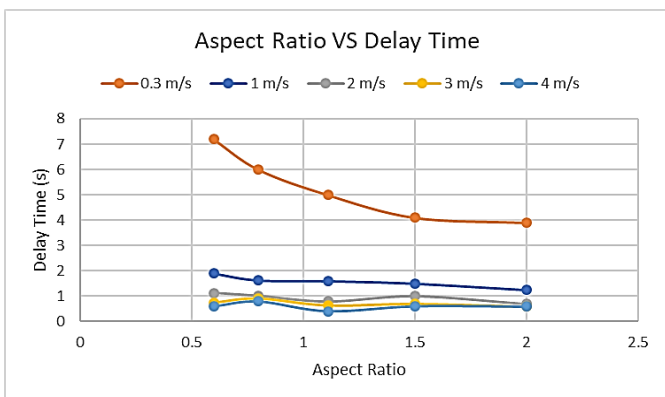
(b)

Fig. 5 Plots of (a) Velocity vs CL (b) Velocity vs Delay Time

Fig. 7 Plots of (a) Velocity vs Frequency (b) AR vs Frequency



(a)



(b)

Fig. 6 Plots of (a) AR vs CL (b) AR vs Delay Time

From Table 1 six different graphs can be obtained in Fig. 5 showing the relations among aspect ratio, lift force, frequency, velocity, and lock-in delay.

From Fig. 5 (a) and (b), it is seen that for a definite aspect ratio, lift force and delay time both decrease with the increase of velocity. Fig. 5 (b) also indicates that delay time is almost constant above 2 m/s.

From Fig. 6 (a) and (b), it is found that C_L and Delay time both decrease with the increasing aspect ratios. There is a drastic reduction in delay time as the velocity increases from 0.3 m/s to 1 m/s.

Again, it is visible from Fig. 7 (a) and (b) that, frequency of vibration most linearly increases with both aspect ratio and velocity. The higher aspect ratio may give higher frequency but it will result in less amplitude of vibration i.e. low power output.

4 Conclusion

The selection of the core method of power generation (electromagnetic induction) in the experimental setup is due to the fact that any other complex conversion incorporates more losses in the conversion process. The raw energy conversion rate proved that the concept of VIV based vertical oscillating converter has potential and could be studied further for practical large-scale implementation. The simulation result paved the way for understanding the behavioral pattern of the vibrating cylinder. It is observed that higher velocities produce greater lift force but at the same time the conversion rate i.e. CL decreases. As VIV occurs in laminar open-channel flows, this converter can be applied where the flow velocity is comparatively lower. Also, greater CL for lower velocities is observed. Again, in order to get sufficient power, the flow velocity should be in an optimally

greater range. This study also revealed that larger aspect ratios produce less CL and the delay time is almost independent of aspect ratios above the velocity of 2 m/s. Hence, in the case of the application of this converter above a velocity of 2 m/s, there is no need to consider converters with higher aspect ratios to gain effective conversion. Also for velocities above 2 m/s, the delay time is negligible. Thus, in practical cases of rivers and canals where the flow could be disturbed frequently, this converter could be applied as immediate lock-in would occur after every disturbance and the hamper in power generation would be negligible. As VIV is a natural occurrence in marine life, this will cause almost no harm to the aquatic environment. Energy can be harnessed from the free-stream which is clean, bio-life friendly, and noise-free.

Acknowledgments

The work presented in this paper is partially funded by the Department of Mechanical Engineering of Chittagong University of Engineering and Technology.

References

- [1] Pritchard, J.L., 1954. Aerodynamics. Selected topics in the light of their historical development. Theodore von Kármán. Cornell University Press, Ithaca, New York. Oxford University Press, Oxford, 1954. 194 pp. illustrated. 38s. *The Aeronautical Journal*, 58(528), pp.841-842.
- [2] Bernitsas, M.M., Raghavan, K., Ben-Simon, Y. and Garcia, E.M.H., 2008. VIVACE (Vortex Induced Vibration Aquatic Clean Energy): A new concept in generation of clean and renewable energy from fluid flow. *Journal of offshore mechanics and Arctic engineering*, 130(4).
- [3] Modi, P.N. and Seth, S.M., 2019. *Hydraulics and Fluid Mechanics Including Hydraulics Machines*. Rajsons Publications Pvt. Ltd..
- [4] Dorman, T.E., Welna, H. and Lindlauf, R.W., 1968. The application of controlled-vortex aerodynamics to advanced axial flow turbines. *Journal of Engineering for Gas Turbines and Power*, 90(3) pp.245-250.
- [5] Edwards, S.S., Edwards Samuel S, 1985. *Wind energy converter utilizing vortex augmentation*. U.S. Patent 4,516,907.
- [6] Patterson Jr, J.C. and Flechner, S.G., 1985. Exploratory wind-tunnel investigation of a wingtip-mounted vortex turbine for vortex energy recovery. NASA Technical Paper 2468.
- [7] Patterson Jr, J.C., National Aeronautics and Space Administration (NASA), 1990. *Wingtip vortex turbine*. U.S. Patent 4,917,332.
- [8] Jensen, D.C., Jensen Donald C, 1994. *Energy converter using imploding plasma vortex heating*. U.S. Patent 5,359,966.
- [9] Carney, M.E., 2008. *Energy capture in flowing fluids*. U.S. Patent Application 11/509,667.
- [10] Cajas, J.C., Houzeauxa, G., Yáñezb, D.J., Mier-Torrecillaa, M., 2016. SHAPE Project Vortex Bladeless: Parallel multi-code coupling for Fluid-Structure Interaction in Wind Energy Generation. Available online at www.prace-ri.eu.
- [11] Bernitsas, M.M. and Raghavan, K., 2004. Converter of current/tide/wave energy. *Provisional Patent Application. United States Patent and Trademark Office Serial*, (60/628,252).
- [12] Govardhan, R.N., 2000. Vortex-induced vibration of two and three-dimensional bodies. Cornell University.

This page is left intentionally blank

Journal of Engineering Advancements (JEA)

DOI: <https://doi.org/10.38032/jea>

Indexed by:



Volume 02 Issue 02

DOI: <https://doi.org/10.38032/jea.2021.02>

Published by: SciEn Publishing Group

Website: www.scienpg.com